Improved Modeling Tools Development for High Penetration Solar

Final Report

Prepared By:
Byron Washom, Jan Kleissl, Anders Nottrott, Ryan Hanna, Handa Yang, William Torre
University of California, San Diego
9500 Gilman Dr. #0057
La Jolla, CA 92093-0411
bwashom@ucsd.edu

Kevin Meagher, Yi Zhang, Rodger Koopman
Power Analytics Corporation
10805 Rancho Bernardo Rd. Suite 270
San Diego, CA 92127
Phone: (858) 675-9211
Fax: (858) 675-9724

Prepared for:

Department of Energy
Award Number EE-0004680

Table of Contents

Acknowledgments and Disclaimer

This material is based in part upon work supported by the Department of Energy under Award Number EE-0004680.

Executive Summary

This report covers Phases II and III of Department of Energy (DOE) award number EE-0004680. The final report for Phase I is available at the DOE High PV Penetration Portal and primarily covers PV power plant variability modeling tools and inverter models for power flow simulation.

One of the significant objectives of the High Penetration solar research is to help the DOE understand, anticipate, and minimize grid operation impacts as more solar resources are added to the electric power system. For Task 2.2, an effective, reliable approach to predicting solar energy availability for energy generation forecasts using the University of California, San Diego (UCSD) Sky Imager technology has been demonstrated. Granular cloud and ramp forecasts for the next 5 to 20 minutes over an area of 10 square miles were developed. Sky images taken every 30 seconds are processed to determine cloud locations and cloud motion vectors yielding future cloud shadow locations respective to distributed generation or utility solar power plants in the area. The performance of the method depends on cloud characteristics. On days with more advective cloud conditions, the developed method outperforms persistence forecasts by up to 30% (based on mean absolute error). On days with dynamic conditions, the method performs worse than persistence. Sky Imagers hold promise for ramp forecasting and ramp mitigation in conjunction with inverter controls and energy storage. The pre-commercial Sky Imager solar forecasting algorithm was documented with licensing information and was a Sunshot website highlight.

For the purpose of ramp mitigation, this report also presents detailed models developed to model, interconnect and ultimately operate a photovoltaic (PV) power plant as anticipated in the DOE SunShot initiative. Power models are used in power system analysis software packages to assess the impact of the integration of PV systems into existing distribution networks of power systems. The models presented herein are developed in Paladin DesignBase software but frequently begin in a different modeling application and are then converted to Paladin DesignBase. To make the models available to a wider engineering community, several conversion routines were developed (e.g. conversion to OpenDSS, Matlab®/Simulink®, etc.), discussed, and are reviewed in Chapter 6. The approach and capabilities developed through the combined research, including the power modeling, forecasting, ramp control and energy storage (battery charging/discharging), have already been proposed in several projects for island communities including Puerto Rico, which is widely considered the most stringent and difficult application for PV integration, control and operation. This work was also largely presented in the Webinar provided by Power Analytics and attended by over 120 individuals on March 27, 2013.

In Command, Control and Communications for Power Flow Management, the project team has focused on implementing an approach that recognizes the dynamic nature of the interoperability and capability communication requirements. The unique combination of proposed standards in the system controller maximizes capability within an open architecture that supports OpenADR, IEEE 2030, IEC 61850, and Legacy Protocols. The Inter-Control Center Communications Protocol (ICCP) was implemented and was certified by Electric

Reliability Council of Texas (ERCOT), the first Independent System Operator (ISO). It must be noted that the IEEE 2030 framework also anticipates the adoption of the Common Information Model (CIM) as a next level of open standard that conforms with the overall strategy of Power Analytics' approach. Through an Inter-Control Center Communications Protocol connection it was demonstrated that a virtual power plant (VPP) can participate in the power market as a true generation resource for bidirectional communications (virtual point of common coupling). Demonstrating this approach of generation-to-ISO communication reduces the barriers to high PV penetration. For example, the Power Analytics' proprietary communications interface and microgrid power management tool was applied and tested through a market simulation with the California Independent System Operator (CAISO). The use of ICCP as a method for aggregating distributed generation of any source as developed in this grant is currently implemented in the ERCOT ISO and has been proposed and reviewed for the Power Analytics' program in the San Diego Naval district.

An energy storage controller function for the master controller that acts upon the forecast has been completed and published on the High PV Penetration portal. The goal is to determine the optimal energy dispatch schedule for the battery to achieve load peak shaving (resulting in a reduction of demand charges), such that the net photovoltaic + storage (PVS) system power output meets or exceeds the customer load peak. The optimization algorithm leverages day-ahead PV power output and load forecasts to ensure that the customer load peak is eliminated or reduced as much as possible, subject to electrical performance constraints of the battery.

In an example considering San Diego Gas & Electric (SDG&E) tariffs, the controller optimizes battery dispatch based on load and PV forecasts to minimize demand charges. The optimal storage dispatch schedule for a typical commercial scale PVS system was simulated during one year, and compared to a simple off-peak/on-peak charge/discharge dispatch schedule that was generated without any knowledge of future PV power output or customer load. The analysis shows that the application of solar forecasting to the energy storage dispatch problem results in significant financial savings when compared with a simple off-peak/on-peak scenario. Financial savings are realized from a combination of demand charge reduction, time-of-use price arbitrage and especially reduced battery cycling which results in extended battery lifetime. A real-time dispatch method based on net-load outperformed the optimization for small demand charge reduction objectives and large battery sizes. The algorithm was implemented in a quasi-operational setting and proved to be robust.

1. Introduction

As photovoltaic systems continue to gain a more significant share of the U.S. electricity generation mix, it becomes increasingly important to better understand the effects of integrating higher penetrations of PV electricity on the reliability and stability of the electric power system. DOE's Funding Opportunity Announcement number DE-FOA-0000085 "High Penetration Solar Deployment" is the basis of the work centered around real time solar forecasting combined with highly accurate modeling and control to determine the effects of high-penetration levels of PV on the system. The previous generation of analysis tools for distribution system planning must be upgraded with appropriate PV performance models, and the fidelity of modeling results must be validated using simulations and field data. The goal of this project is to develop the needed modeling tools for high penetration scenarios of PV on distribution feeder systems. Adopting suitable reliability criteria for PV generation technologies on the power system is very important since many utilities in the US are receiving an increasing number of requests for interconnection of PV plants in their respective power systems.

The project's objectives are to

- Develop simulation tools for distribution feeder design by power system designers
- Characterize PV variability and develop a cloud tracking and forecast model
- Reduce integration costs and remove barriers to high PV penetration
- Provide means for the customer to manage power flows and battery storage according to economic conditions (e.g. dynamic price signals)

The research team consists of prime contractor UC San Diego (UCSD) and subcontractor Power Analytics. UCSD is responsible for the overall project management and the modeling and forecasting of the solar resource. Power Analytics is responsible for power systems analysis and utility command and control interfaces (Task 3).

2. Accomplishments

The Statement of Project Objectives (SOPO) task statements are provided below. Accomplishments are presented by subtask in *italics*.

PHASE II (DE-EE0004680)
Subtask 2.2. Three-dimensional Cloud Tracking and Insolation Forecast Model: The purpose of this task is to develop an energy storage controller function of the master controller that will respond to the cloud detection and forecast system using a three-tiered mechanism.

> *The energy storage controller function has been completed and applied in a case study of the Sanyo/Panasonic 30 kW/30 kWh PV Integrated Energy storage system (Chapter 5).*

A real-time observation network of insolation measurements that operates continuously at high temporal (1 second) and spatial (16 stations over 1200 acres) resolution will be utilized. It is collocated with a Sky Imager, a ceilometer, and 1 MWp distributed solar PV array.

> *The sensing infrastructure has been operated and maintained during 2010-2013. The data are used for validation of the solar forecast in Chapter 4.*

Using existing infrastructure at UCSD a generalized real-time cloud tracking and forecast model will be developed. The energy storage controller function of the master controller will respond to the cloud detection and forecast system using a three-tiered mechanism. Tier 1 is the real-time cloud detection, when on a clear day the detection of clouds by a Sky Imager or satellite will signal the controller to start diverting an appropriate amount of the PV output to charge the storage system. Conversely, the detection by the Sky Imager of a reduction in cloud cover will signal the controller to start discharging the storage system in anticipation of a rapid increase in solar power output. Tier 2 is the three-dimensional cloud position forecast that uses pattern recognition algorithms to derive cloud motion vector fields from sequential sky images and forecasts cloud positions for the hour ahead. Cloud height will be determined by a ceilometer. Given typical reductions in solar irradiance due to clouds, the controller will compute the amount of storage required to smooth out the PV power production curve. Tier 3 is the power output forecast, which is recomputed as cloud-related solar radiation reductions are observed at the micro climate stations, the optical depth of each cloud will be computed and used by the cloud position algorithm to determine expected solar power output at each PV array for the following hour. This will result in a full three-dimensional model that tracks and forecasts the movement, optical depth, and shadow locations of individual clouds with respect to solar PV arrays on the ground.

> *A three-dimensional cloud forecasting model has been developed and validated at the UCSD solar energy testbed (Chapter 4). From UCSD sky images, clouds are detected, cloud velocities and optical depths are estimated, and cloud shadows are projected onto maps of photovoltaic arrays. The cloud forecasting model has been implemented at UCSD's 2.0 MW distributed photovoltaic arrays on campus. The pre-commercial Sky*

Imager solar forecasting algorithm was documented with licensing information and was a Sunshot website highlight.

Task 3.0 Command, Control and Communications for Power Flow Management

Table 1 Definition of Terms

UCCI	Utility Command/Control Interface
System Controller	Communications master integrated into the micro grid master controller
OSI	Open Systems Interconnection Model established by the International Organization for Standardization
7 Layer Model	OSI Standard abstracted into (1) physical, (2) data link, (3) network, (4) transport, (5) session, (6) presentation, (7) application
SOA	Service Oriented Architecture is principles and methodologies for designing and developing software in the form of interoperable services
ERCOT	Electric Reliability Council of Texas

The Utility Command/Control Interface (UCCI) establishes a common interface for bi-directional communications between the system controller (SC) and the electrical power service provider or utility.

> *A UCCI that establishes a common interface for bi-directional communications between the system controller (SC) and the electrical power service provider or utility was developed by Power Analytics. Each service provider and utility typically requires their own certification process and agreement on the blocks supported. Power Analytics used the ERCOT validation process for the first Inter-Control Center Communications Protocol (ICCP) implementation, as the ERCOT definitions and performance parameters are the most stringent and performance oriented. The ICCP connection is primarily for the system controller to the utility or service provider. The device level protocols are translated to the device (system controller to the device). ICCP is the first level of system controller to utility or service provider in the IEEE 2030 framework. This ICCP implementation is IEC 60870-6 TASE.2 Blocks 1, 2, 3, 4 & 5 and can be either client or server.*

The UCCI's operation complies with the OSI seven layer model and utilizes non-proprietary methods whenever possible. The UCCI application layer defines a structure and method to process price signals from the utility or RTO/ISO, energy dispatch signals from the utility or RTO/ISO, acknowledgements with the utility or RTO/ISO, system performance and status from the PV system to the utility or RTO/ISO, metered performance to the utility or RTO/ISO and/or third party certification, operating software upgrades from the utility or RTO/ISO to the PV system, and the demand management gateway to the user premises. The UCCI also incorporates other modes of operation depending on local and external conditions, including:

- Net Metering (when the utility grid is viewed as an infinite source or sink for power);

> *Power Analytics has implemented the ICCP testing and support for a specific General Electric (GE) meter to validate the net-metering performance. The primary goal of the service-oriented architecture (SOA) is to translate secure requests and data from supported devices and protocols (including photovoltaic) through the ICCP connection. This interconnect includes OpenADR (DRACS) for OpenADR devices and as an emulation through to the service provider. In this manner, Power Analytics maps the existing protocol and interconnect to the device (PV inverter) through the ICCP connection. The Power Analytics SOA is intended to directly support other emerging standards as part of the IEEE 2030 framework.*

- Utility Dispatch Source (where the utility is always sourcing some energy to the local load) and Utility Dispatch Sink (where the PV system is always sourcing some energy to the utility grid, to the extent that local energy is available);

> *A primary capability of the system controller is to both optimize the energy resources and provide a communications link directly to inverters (PV) and other control devices. The following critical SOA elements reflect this capability: connection to the utility or service provider (ICCP) and connection to the inverter (IEC 61850, Modbus, OpenADR or proprietary device protocol). The targets and the controls are defined in the utility or service provider connection and then mapped to the device with control commands.*

- Price Signal (which allows the PV system to determine when favorable economic conditions warrant a particular energy flow action); and Override (when the customer takes total control of operation regardless of utility dispatch of price signals).

> *The existing ICCP (IEC 60870-6 TASE.2) includes definitions for real-time price signals, Locational Marginal Pricing and extended block support. The system controller can virtualize the PV resources as well as storage and other generation/load resources. The real-time optimization of these resources can be represented to the utility or other provider in the form of specific resources or virtualized resources depending on the level of control and interconnect to the devices. Inherent in the architecture is the ability to automatically or manually override automatic operation independent of the utility price signals. The simulation environment (blackboard) of the system controller allows the operators to simulate an override to see what the impact will be before executing the override.*

PHASE III (DE-EE0004680)
Task 4.0 Field Testing and Validation of the Suite of Models

The purpose of this task is to field-test and validate performance of the models and distributed energy storage and PV to electric vehicle charging as mitigating measures at its existing 1 MW (total at seven sites) and potentially at its 900 kW (total at five sites) of PV.

The BMW B2U installation at the UCSD campus is a 100kW, 160kWh battery energy storage system with existing photovoltaic- system and inverter integration (AC) a battery backed up Level II EV charger. The system was used to demonstrate integrated operation of energy storage with solar PV. If we are to enter into the new battery second use market segment it is imperative that we understand the opportunities and challenges from a technical and operational standpoint. Critical parameters within the value chain include the technical requirements for system integration and secondary use. This includes component requirements and control strategy of the system, and load profiles and market value of stationary applications.

To better understand these requirements UCSD installed the first commercialized Battery 2nd Life system together with the California Center for Sustainable Energy (CCSE), and National Renewable Energy Laboratory (NREL). The following objectives were addressed:

- Identify use cases in various market segments
- Development of control algorithm for balancing and State of Charge (SOC) calculation for second use systems.

After baseline health characteristics of the battery were established, energy storage application duty cycles were tested. A regulation energy management (REM) duty cycle and a demand charge management duty cycle were performed. For demand charge management, the system responded in real-time to campus resources, particularly building loads and solar generation resources. Further a solar PV firming application was demonstrated.

> *Energy storage controllers to firm demand charge savings of solar PV were tested in a quasi-operational setting for two months.*

The resource models developed under previous tasks will be used to predict solar electric output under high PV penetration levels, and will be verified against actual PV system performance based upon the micro climate stations’ forecast and resource models as well as newly developed high resolution datasets. A comprehensive evaluation of a solar forecasting method would require one year of data. However, compiling the Sky Imager forecasts is very complex and time intensive. Different cloud heights, aerosol content of the sky, and instrument limitations (especially the shadowband which blocks the sky view) require manual adjustments and quality control of the forecast. UCSD is currently working on improvements to the method that would allow more accurate ‘on-line’ forecasting. Under Phase 3, Task 4.0 Field Testing and Validation of Suite of Models UCSD will conduct a more thorough evaluation using forecasts at UCSD.

> *Sky Imager forecasts were evaluated during two months, November 2012 and June 2013.*

Task 5.0 Raise Situational Awareness of Virtual Power Plants and Microgrids by Distribution Utilities and RTO/ISOs

The purpose of this task is to perform real-world simulations, evaluating and verifying microgrid renewable integration operations in a controlled and well-instrumented environment and to raise the awareness and understanding of the RTO/ISO operators.

> *Power Analytics has successfully implemented the VPP interface with one ISO as a direct result of the goals of this program. The example of the ERCOT ISO represents a step function in integration of a Virtual Power Plant in the North American networks. This same capability has been proposed in other NERC/FERC related applications, including the opportunity for situational awareness that does not require market participation or control but represents secure communications via existing communications standards and is based on the overall architecture provided by Power Analytics and UCSD.*

The anticipated proliferation of Distributed Energy Resources (DERs), including, but not limited to, distributed energy storage and electric vehicles, has the potential to significantly complicate or enhance the operation of local electricity distribution networks and transmission grids. These DER resources are smaller than traditional central-station generating plants and are frequently connected to the local distribution network, rather than to the transmission grid. Some of them will be “behind the meter,” where they will not even appear as supply, but as load reductions. Several issues need to be addressed to enable the distribution grid and Regional Transmission Operators/Independent System Operators (RTO/ISO) to maintain the appropriate level of situational awareness. With greater penetration of DERs, observability, dispatchability, and permitted autonomous actions by DERs must be established. One approach to addressing these issues is to organize the DERs into structures that can be more easily characterized and understood. Three such structures are virtual power plants, microgrids and aggregations.

> *The first and most extensive of these is aggregation as a demonstration for an ISO. Power Analytics has successfully deployed an aggregated virtual power plant (VPP) with a municipality. A simple block diagram architecture is:*

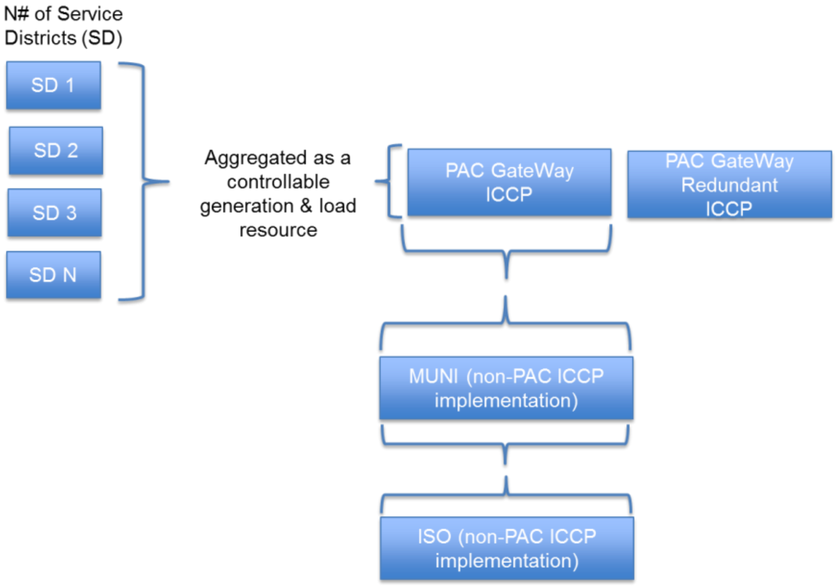

Figure 1. Block diagram architecture.

> *This configuration has been operational for 12 months and illustrates the integration of virtual resources into the mainstream of power generation and distribution at the retail level.*

This project will raise the distribution and RTO/ISO operators' understanding of Virtual Power Plants (VPP) and microgrids to a level that will permit these resources to become competitive operational assets for power generation, demand response and ancillary services responding to dynamic price signals. This will be accomplished by performing real-world simulations, evaluating and verifying microgrid renewable integration operations in the controlled and well-instrumented environment on UCSD's microgrid. The demonstration will incorporate renewable resources including solar PV coupled with advanced energy storage and demand response to test the ability of the microgrid to adjust its internal operations. Adjustments made will stabilize the variable renewable generation and allow the local utility to better balance their networks and the RTO/ISO to reliably schedule and dispatch the microgrid. A similar test will be performed for a VPP, including storage and load management capabilities with local thermal generation. This additional generation will simply appear to the system as supply and be modeled and dispatched within the RTO/ISO systems in exactly the same manner as any generation resource.

> *The primary accomplishments toward this goal have been in the simulation and planning for the UCSD microgrid. All advanced capability required for controllable resources is dependent on high quality, high availability of data streams at the Virtual Power Plant. There are extensive upgrades and enhancements that are required to the existing infrastructure of UCSD that are critical to increase the accuracy and reliability of real time sensor and meter data from the existing infrastructure. As the infrastructure is undergoing upgrade, focus has shifted to specific critical elements, including the*

control and testing of energy storage integrated with photovoltaic power. That testing and integration is also documented in the 2nd Life Battery program and integrated into the UCSD Microgrid as a controllable resource.

The software infrastructure is in place at UCSD to enable VPP level integration for ancillary services and dynamic price signals, but no contract is currently in place with SDG&E for actual market participation except in the existing Direct Access program and demand response.

The additional simulations and research have led directly to studies and capabilities included in this report and are integral to the advanced modeling and forecasting.

3. Command, Control and Communications for Power Flow Management: Utility Command/Control Interface and Situational Awareness (Tasks 3 and 5, PA leads)

3.1. Introduction

In order for advances to occur, or to develop in power systems modeling and hardware systems, a critical step is the communication or interconnects of these systems to the utility or bulk grid. There are focused efforts by organizations such as National Institute of Standards and Technology (NIST) (in particular the Smart Grid Interoperability Panel (SGIP)), IEEE, and IEC, all working to address the depth and breadth of existing and proposed standards for interoperability. A brief listing of the standards, options, agencies, and organizations that are engaged in this effort is included in Appendix A.

This effort has been specifically focused on achieving and delivering an interconnect strategy consistent with the requirements of Task 2, that includes implementation and verification in Phase 3 of research. While implementation is the goal, it is also important to support specific interoperability architectures that are consistent with the goals of the research and the goals of the larger standards being proposed.

On September 10th, 2011, the IEEE Standards Coordinating Committee 21 (Fuel Cells, Photovoltaics, Dispersed Generation, and Energy Storage) published IEEE 2030™-2011, representing what the authors believe is the most comprehensive architecture for interoperability. The IEEE 2030 standard does not recommend specific technologies, but rather it provides guidelines and use cases that are relevant and in sufficient detail to be used in architecting a solution.

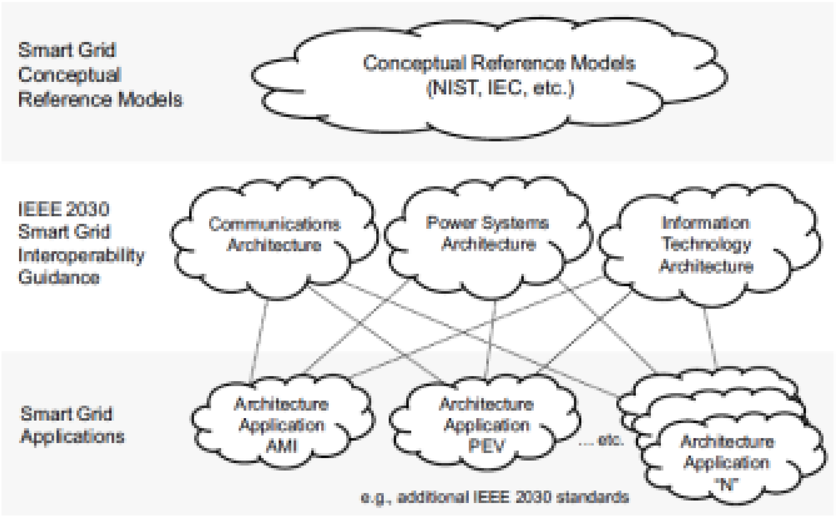

AMI = Advanced metering infrastructure

PEV = Plug-in electric vehicle
N = Other smart grid applications

Figure 2 - Evolution of smart grid interoperability[1]

The specific requirements of this report and the implementation are a subset of the IEEE 2030 report with the significant additional elements that the system must be installed, operational and capable in Phase 3 of the program. To accomplish this, the proposed implementation addresses the following:

- Physical infrastructure is an *existing* microgrid with legacy equipment and networks that cannot be removed or significantly modified as part of this research. Cost and time are always barriers to advanced technology.
- The electrical power service provider (utility) is SDG&E. However, the solution must have broad industry acceptance, leverage existing utility integration capabilities, and be consistent with accepted standards and protocols.
- The microgrid system (or System Controller) must also meet the operational standards of the UCSD cyber security, and performance of an existing mission-critical facility without interruption.

The overall architecture being deployed treats the infrastructure of UCSD as a “Virtual Power Plant” or VPP to aggregate the load and generation sources of UCSD, and present a single point of interconnect for the bidirectional communications.

3.2. Virtual Power Plant (VPP)

Service Oriented Architecture (SOA) – “The interoperability services in the System Controller (SC) is foundational to the VPP”.

Power Analytics software architecture is based on a Service-Oriented Architecture (SOA) that connects services to analytics, devices, and systems.

---

[1] 2030-2011 - IEEE Guide for Smart Grid Interoperability of Energy Technology and Information Technology Operation with the Electric Power System (EPS), End-Use Applications, and Loads, ISBN 978-0-7381-6728-2, STDPD97148

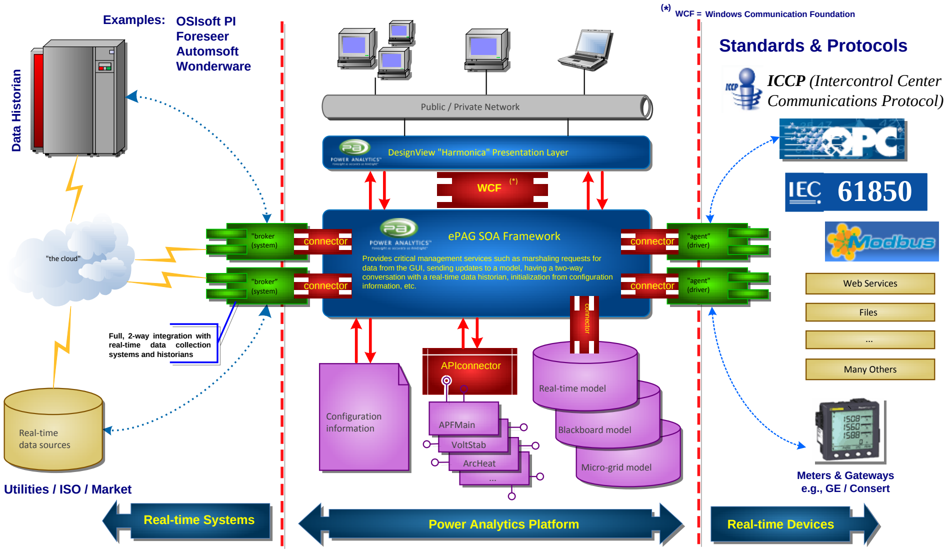

Figure 3 – Power Analytics Gateway Service Oriented Architecture

The elements of this architecture that are most relevant are the following:

- OpenADR – The OpenADR is an open standard for demand response in the California electric market. OpenADR implements specific connectivity for server-based connection to the ISO or utility (Demand Response Automation Server (DRAS)) and client connection. Both OpenADR server and client protocols are being implemented by Power Analytics as part of the Utility Command and Control Interface (UCCI) development.
- IEC 61850 – The 61850 standard and related standards provide a highly functional interoperable communications protocol. The original standard was intended for high-speed, reliable communications with substations, but has expanded to including mapping for other device level protocols. The IEC 61850 is also a focus of the UCA International User Group (UCA-UG) in the standards for the Common Information Model (CIM) for Smart Grid Interoperability. Power Analytics currently offers 61850 interface capabilities as a part of the SOA architecture
- OPC – OLE for Process Control or OPC is a standard for open interoperability, originally for manufacturing, but significantly expanded to include building management, process control, discrete manufacturing, and others. Power Analytics currently offers OPC connectivity directly to the SOA architecture.
- MODBUS – Modbus is a legacy communications standard still widely used in power metering and process control systems. Power Analytics currently offers Modbus interface as a part of the SOA architecture
- DNP3 – Distributed Network Protocol (DNP) is an advanced communications protocol also prevalent in Supervisory Control and Data Acquisition (SCADA) systems in particular, for utilities and process control. Distributed Network Protocol 3 is also

published as IEEE Std 1815-2010. Power Analytics currently offers DNP3 interface as a part of the SOA architecture

- ICCP – The Inter-Control Center Communications Protocol is used globally by utilities and generators as a primary method for generation, transmission, and distribution data exchange. What differentiates ICCP from other methods of communications is addressed in detail within Section III.

One of the primary benefits of the virtual power plant concept is the ability to aggregate a wide variety of generation *and* loads to provide a single representative stream of data from the premise to the utility. The aggregated VPP information is of significantly greater commercial value to the utility or power service provider when it can be treated like any other generation source to the operator.

This distinction creates value to both the VPP owner/operator and the utility or service provider. Since ICCP is an existing integration structure and is already well established, the barrier of entry for the VPP unit for market participation is low. The relevance for high-penetration solar is the operational and economic benefit derived from combining the VPP capability with the bi-directional communications through the ICCP standard.

Figure 4 - Virtual Power Plant Aggregation

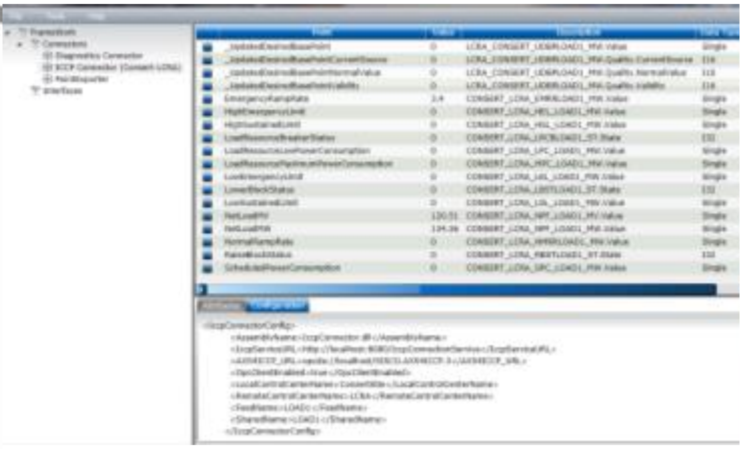

Figure 5 - ICCP Connection Controllable Load Resource (CLR)

The concept of a VPP is at the center of advanced planning and operational models for utilities, generators, and retailers for a very good reason. A VPP can be an aggregation of assets based on financial or physical resources, but the real benefit comes when both are possible.

In the physical model, the System Controller (SC) is the aggregation point for load and generation resources including solar. More than just aggregation though, the detail or granularity provided by the SC is exactly what is needed for the virtual power plant to operate, or appear as a true generation resouce. A well-behaved VPP is an invaluable asset to the utility or service provider because it can be more than a demand response. Since aggregation results in more accurate net load forecasting, and the response time is within the requirements of other physical generation plants, the VPP is also more highly compensated financially. In fact, the appropriate level of interoperability allows the utility to interface directly with the VPP SCADA (supervisory control and data acquistion) systems and DMS (distribution management systems).

The SC is also the branch-off location of the power network model which includes the specific inverter designs, and the aggregation point of the solar irradiance data. Again, it is this type of granularity that not only increases the value to the utility or service provider, but concurrently increases the financial value of the VPP to its owner, and by association, supports high penetration solar. Increased accuracy, forecastability, and interoperability all directly serve to increase the value of the VPP and renewable resources in particular, as a function of the overall utility or service provider portfolio of available assets.

The combination of the real-time power model, the real-time solar irradiance data, and the rest of the power infrastructure are all relevant to bi-directional communicatons. In effect, ICCP from the System Controller to the utility or service provider is the interoperability equivalent of point of common coupling to the same utility or service provider.

The SC also functions as the load/generation model balancing for photovoltaic on the virtual power plant.

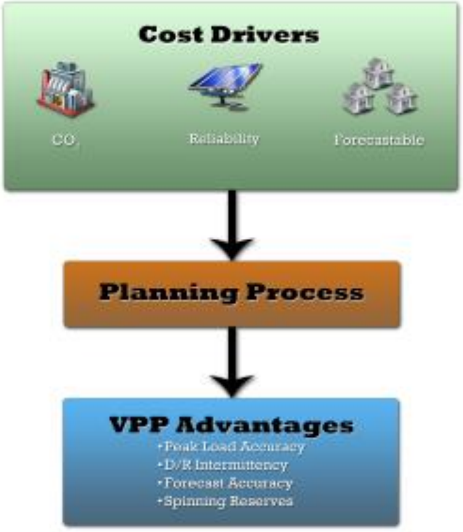

Figure 6 - System Controller as Virtual Power Plant

Figure 7 - Cost Advantages of a Virtual Power Plant

Accurate net load forecasting is a difficult process under normal circumstances. The impact to utilities and service providers is compounded with generation or loads that are not aggregated because the burden falls almost exclusively on the utility or service provider. The market structure and opportunities for generation and controllable loads reflect the risks for the utility or service provider; therefore, any and all structures that minimize risks for the utility or service provider are reflected in the market value of the resource. The promise of a virtual power plant, regardless of how the VPP is organized (as an operational VPP or a financial VPP) is to reduce the risks and increase the economic benefit for the VPP. Perhaps nothing demonstrates the economic benefit more than the significant price differential between the normal curtailment types of demand response, and the more lucrative generation programs.

Increasing the penetration of photovoltaic energy generation is impacted by many factors. This research is concerned specifically with the definition, development, and implementation of a secure, bidirectional, and open architecture communications capability for the command and control of generation and load resources generally, and photovoltaic resources specifically. The economic value of this has a quantifiable and direct economic impact on the level of solar penetration, and an indirect impact on the adoption rate of distributed generation resources. The intent is not to produce a pro forma financial model so much as to recognize that the ability to allow the virtual power plant/microgrid to operate as a generator provides a structure and economic incentive for increased photovoltaic penetration.

3.3. ICCP: Interoperability for Utilities and Service Providers

As important as the modeling for power impact, cost of deployment, and performance capability of photovoltaic is, the method or methods of interconnecting with utilities is as essential. The Inter-Control Center Communications Protocol (internationally IEC 60870-6 or Tase 2) is unique in its widespread adoption and use globally. The critical elements include:

- ICCP is capable of working across both LANS (local area networks) and WANS (wide area networks)
- ICCP uses TCP/IP (OSI 7 layer communications standard)
- ICCP has secure options and the operational redundancy that is required for communications and control of resources.
- ICCP “normalizes” the interconnect and interoperability of the controlling entity and the virtual power plant. In effect, ICCP defines the “how”, so that all activity is focused on the “what”.
- ICCP is supported in ALL tariff structures so that regulatory compliance is not a gating item to implementing high penetration solar as part of a virtual power plant.

Power Analytics has implemented an ICCP interconnect (TASE 2) and achieved qualification of this interface in 2012 as part of work with Consert and utilities in the Electric Reliability Council of Texas (ERCOT) market. Power Analytics is also working towards certification with additional utilities (SDG&E) or regulatory associations (PJM and CAISO). The capability created by Power Analytics is broad and unique, as the SOA framework is deployed at UCSD and in a network operations center in the Mid-Atlantic region.

A significant element of an ICCP connection is the creation of so called “Bi-Lateral Tables” (BLT). The BLT is in essence the agreement between the two subscribing entities about what information will be exposed by both parties. The Power Analytics ICCP supports multiple BLTs so that a single instance of the Power Analytics ICCP interface can connect to multiple service providers.

Figure 8 - Power Analytics ICCP Multiple Bi-Lateral Table (LCRA)

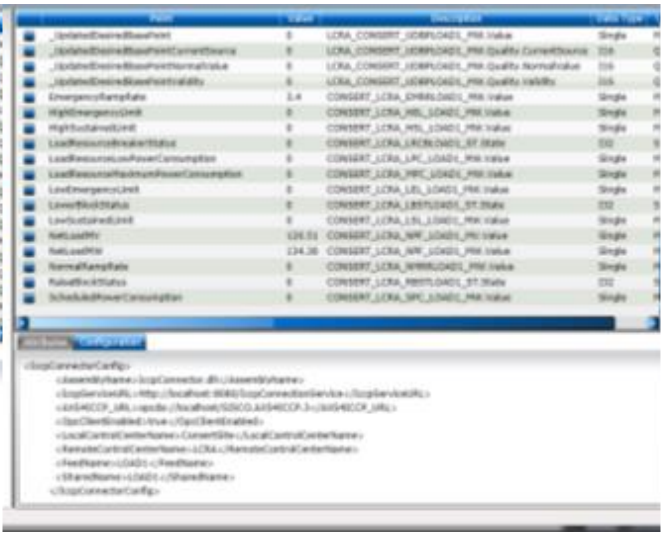

Figure 9 - CLR Control Block Successful Transmission

A requirement of Power Analytics ICCP is to support Controllable or Curtailable Load Resources (CLRs). The ERCOT definition of a CLR is a *Load Resource capable of controllably reducing or increasing consumption under dispatch control (similar to AGC) that immediately responds proportionally to frequency changes (similar to generator governor action).* This requirement is fundamental to a high speed and secure connection because the CLR requires a two-second response time.

Power Analytics has included management data to measure the network performance from command issued to command received in less than two seconds. The responsiveness of the system is a requirement for all ancillary services regardless of the location. For example, with Frequency Response with ERCOT, generator turbines are required to operate with governors in service that increase or reduce generation automatically (governor response) if and when the ERCOT frequency deviates from 60 Hz by more than 0.036 Hz.

This responsiveness includes droop response (defined as the percentage of frequency decay that will tend to cause a turbine generator to increase its output 100%). For example, if frequency drops from 60 Hz to 59.7 Hz, a 100 MW turbine generator with a 5% droop setting should increase its generation output by (0.3 Hz / 3 Hz) x 100% x 100MW = 10MW. Similarly, a VPP must be able to automatically, immediately, and proportionally respond to frequency deviations while providing Ancillary Services.

3.4. Implementation and Validation

While not a requirement of the ICCP connection, the validation begins with the creation of the target power network model including all the resources (generation and loads) that will be part of the overall solution. This includes the solar inverter models specific to the manufacturers, and the location of the PV on the power network. The overall capability of the virtual power plant is what determines the participation of the VPP as an aggregated resource, and not necessarily limited by any one resource (including all generation and load resources that will be part of the ICCP commitment).

Definition of the Bi-Lateral Tables and ICCP Blocks supported: Every ICCP controlling entity will have specific control blocks (Power Analytics supports IEC 608770-6 TASE 2, blocks 1,2,3,4 and 5) but the bi-lateral tables and the definitions must be created for each instance. Power Analytics is both client and server for ICCP.

The process steps for creation and integration of a Power Analytics VPP are as follows.

(i) Create a model of the electrical network with all electrical characteristics of each component as shown in Figure 10.

(ii) Integrate the real-time data from the microgrid or VPP to become part of the forecast for generation and load, the operator interface and contingency planning of the VPP. Connect to the controlling operator via ICCP, or become situational awareness via the same IEC 608770-6 TASE 2 interface.

(iii) Initiate the process with the target Utility or Service Provider that will be the ICCP connection. For illustrative purposes only, the initiating process for ERCOT is shown below:

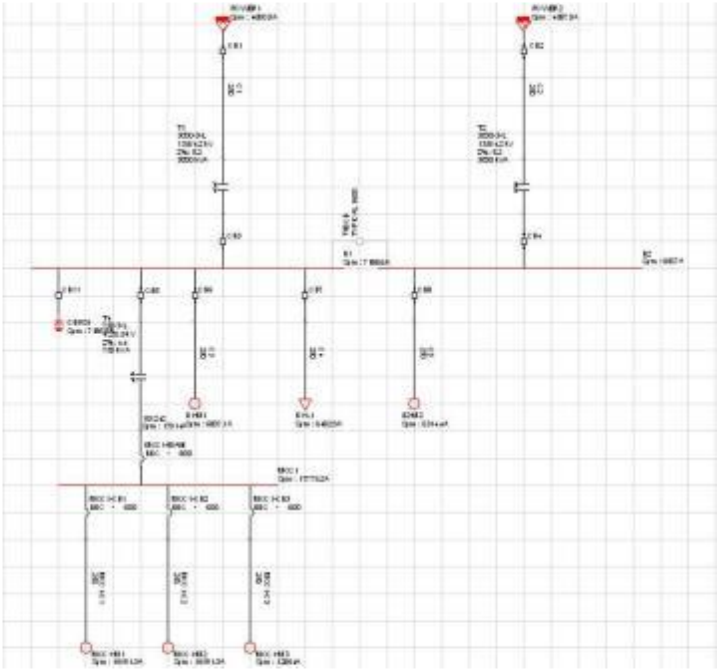

Figure 10 - Creating a model of the electrical network

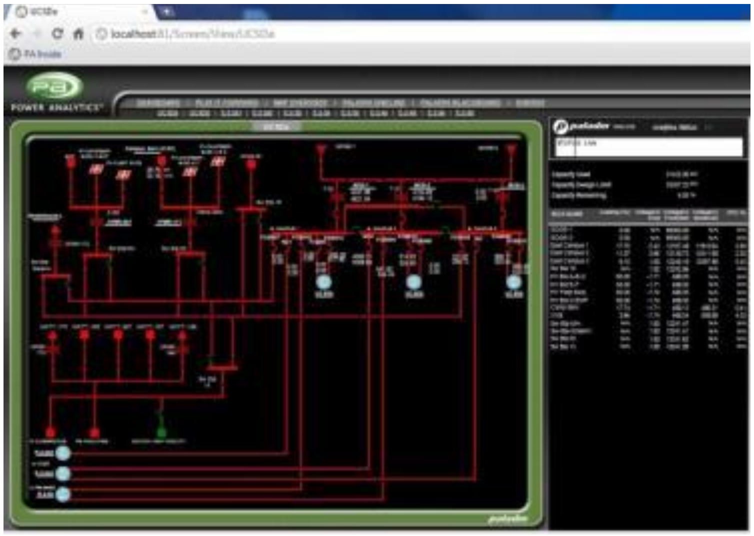

Figure 11 - Real-time data of the Power Network is translated through ICCP connection(s)

Market participants are required to use the ERCOT WAN for exchanging data with ERCOT via ICCP. The data to be exchanged is defined in the ERCOT ICCP Communications Handbook Version 3.02. In order to initiate the connection process, market participants must complete and submit a “WAN application.”

3.5. CAISO trial to raise situational awareness of Virtual Power Plants (VPP) and Microgrids

The purpose of task 5 was to raise the situational awareness and understanding of the RTO/ISO of solar distributed energy resources (SDER). SDERs are often "behind the meter," where they will not even appear as supply, but as load reductions. With greater penetration of SDERs observability, dispatchability, and permitted autonomous actions by DERs must be established. One approach to addressing these issues is to organize the DERs into structures that can be more easily characterized and understood.

As part of this project UCSD provided the CAISO access to its OSI server database to monitor microgrid operations. The purpose is to enable CAISO to achieve a Deep Situational Awareness of the performance of UCSD's distributed energy resources particularly during demand responses called by CAISO and Critical Peak Pricing called by SDG&E. The fact that both CAISO and UCSD utilize OSIsoft's PI software permits CAISO to be issued a UCSD user password which enables CAISO personnel to observe the UCSD microgrid at any metered level of granularity of distributed energy, resources including energy storage, that is typically not observable since it is behind the utility meter. This top down vantage point provided to CAISO also enables analysts to later request the data files of particular events or equipment through secure data delivery protocols.

As part of the effort to understand how virtual power plants and microgrids with high PV penetration would operate in within a RTO/ISO, UCSD completed a market simulation exercise with the CAISO.

The CAISO is developing new markets for wholesale products and other California opportunities for integrating their Microgrid as well as informing tasks identified in the DOE PV High Penetration projects. UCSD received training, participated in CAISO market simulation, and explored market integration opportunities.

UCSD's stated objectives were to:

- Observe various market participation options for Microgrid capabilities with both Proxy Demand Resource (PDR) and Non Generator Resource (NGR) including both NGR options, Regulation Energy Management (REM) and Non-REM.
- Obtain a "clean" AGC data set for NGR operating in REM option for Frequency Regulation participation.
- Obtain "Bid to Bill" data for various products on both resource types.

To fulfill these objectives, UCSD participated in CAISO market simulations. CAISO operates these simulations on a periodic basis to test the deployment of new market features. Market simulations utilize the Market and Performance Stage (MAP Stage) test environment and typically run bid to bill scenarios to demonstrate the full integration of the new feature prior to release to production. While the Fall 2013 market simulation was not specifically testing specific features associated with microgrids, demand response or energy storage it provided an opportunity to create pseudo-resources to best represent UCSD microgrid market capabilities and see those resources in a near production environment from bid to bill. Participation in the market simulation provided an opportunity to learn more about how UCSD microgrid and VPP market capabilities could interface in the market without the risk and the expense of participation in the production market.

The creation of the Non Generating Resources (NGRs) required inclusion in the full network model that is used in the market simulation environment. CAISO personnel outside of the modeling group assisted in development of NGR market models for UCSD for the market simulation. Similarly the CAISO assisted UCSD and its consultant to develop the Proxy Demand Resource Model (PDR) that was placed into the market simulation. The market simulation of the UCSD microgrid was conducted during the months of September through October of year 2013.

The results of the market simulation did provide a number of data points supporting basic market familiarity and that begin to inform the potential of market participation. In specific, the frequency regulation test of the UCSD NGR resource was completed successfully when it ran on a simulated AGC signal and showed similar patterns as other AGC scenarios observed in previous market simulations.

Results from the market simulation frequency regulation test provide insight into how an energy storage resource might operate in the market when providing frequency regulation. Figure 1 shows a representative example of regulation dispatch during the period when the CAISO operated the scenario. The AGC line shows dispatch within the discharge and charge range of the resource while the green field shows how the result of the 50% rule under the Regulation Energy Management (REM) option maintained the State of Charge near the midpoint of the registered storage capacity of 20 MW.

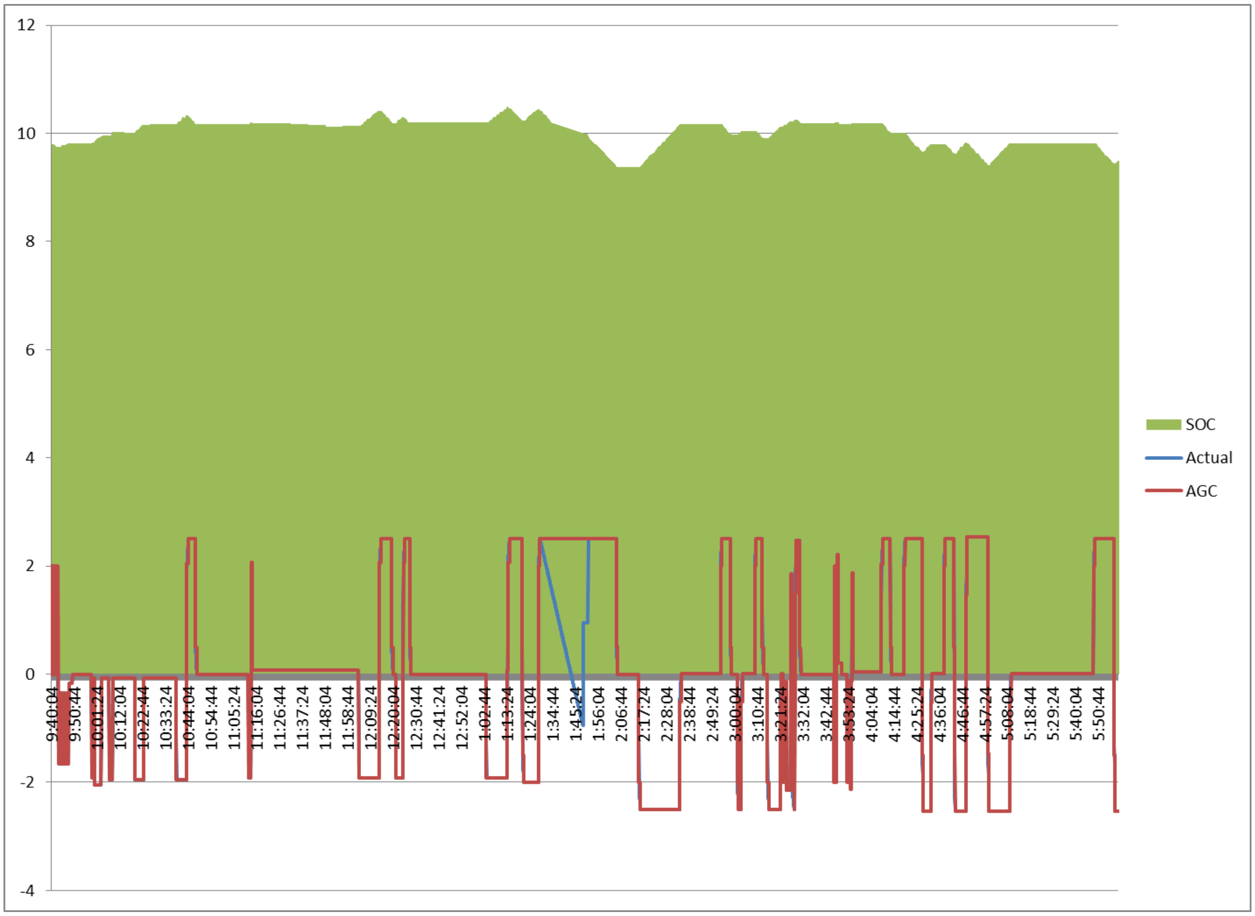

Figure 12: Energy storage state-of-charge (SOC) and CAISO AGC control signal and actual performance.

3.6. Conclusion

The ability to bring solar resources into a virtual power plant enables the VPP operator to participate in the most significant financial structure defined in North America and beyond, when the VPP can be operated as a true generation resource, and not a discounted connection due to variability or intermittancy. While all the connectivity options are important toward the goal of increasing solar penetration, none is more important than the ICCP connection for true bidirectional communications. The distinction of using this existing standard in a new way reduces the barriers of entry for solar energy, and facilitates the advancement of the science and goals of the high penetration solar initiative. Power Analytics has implemented IEC 608770-6 TASE 2 standard in the RTO/ISO application and has proposed providing similar capability for UCSD and the Department of Defense.

4. Three-Dimensional Cloud Tracking and Insolation Forecast Model (Task 2, UCSD leads)

In this section a three-dimensional cloud forecasting methodology based on Sky Imagery and its implementation at the UCSD campus is presented. Solar forecasts are used with a battery dispatch controller to optimize the net present value of a PV+battery storage system.

4.1. Introduction

Integration of large amounts of photovoltaic (PV) systems into the electricity grid poses technical challenges due to the variable nature of the solar resource. The ability to forecast solar irradiation will allow grid operators to better accommodate the variable electricity generation in their scheduling, dispatching, and regulation of power. Currently, physically based forecasting is primarily conducted using numerical weather prediction (NWP) and satellite cloud observations. NWP provides information up to several days ahead; however there are significant biases and random errors in the irradiance estimates (Remund, Perez, & Lorenz, 2008) (Lorenz, et al., 2009) (Perez, Kivalov, Schlemmer, Hemker Jr., Renné, & Hoff, 2010); (Mathiesen & Kleissl, 2011). The spatial resolution of NWP is coarse at about 100 km^2, but there is active research on high-resolution rapid refresh models with grid cell areas of less than 10 km^2 (Benjamin, et al., 2010) (Lara-Fanego, Ruiz-Arias, Pozo-Vazquez, Santos-Alamillos, & Tovar-Pescador, 2011). Either way, most clouds will remain unresolved in NWP. Frozen cloud advection based on GOES satellites images can provide accurate forecasts up to six hours ahead (Perez, Kivalov, Schlemmer, Hemker Jr., Renné, & Hoff, 2010) (Schroedter-Homscheidt, Hoyer-Klick, Rikos, Tselepsis, & Pulvermüller, 2009) at a resolution of 1 km^2.

To achieve high temporal and spatial resolution for intra-hour forecasts, NWP and satellite forecasts are currently inadequate. Ground observations using a Sky Imager present an opportunity to fill this forecasting gap and deliver a sub-kilometer view of cloud shadows over a central PV power plant or an urban distribution feeder. In this report, intra-hour cloud shadows and irradiance forecasting is demonstrated for the UCSD microgrid.

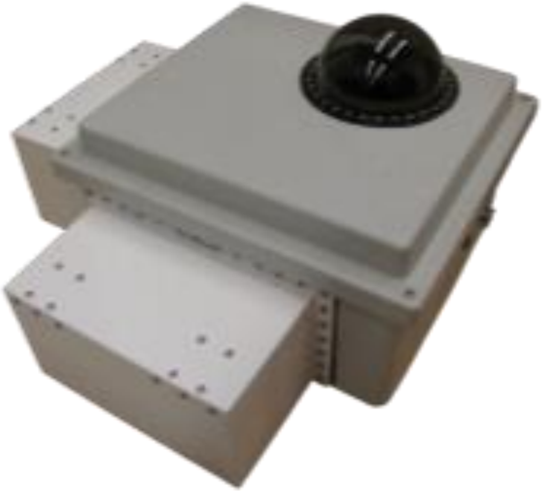

Figure 13 - Map of UCSD showing Sky Imager (USI) and weather stations. © Google Maps, 2013.

Figure 14 - UCSD Sky Imager (USI)

4.2. Three-dimensional Cloud Forecast Model

A rooftop mounted UCSD-designed and constructed sky imager (USI, setup at 32.8852°N, 117.2400°W, 124 m MSL) has taken images of the sky over UCSD since August 2009 (Figure 13). The instrument consists of a spherical mirror and a downward pointing camera. Images are taken every 30 seconds when the sun is above an elevation angle of three degrees.

To obtain cloud locations in the image, a clear sky library (CSL) (based on (Shields, et al., Research toward Multi-Site Characterization of Sky Obscuration by Clouds, 2009)) as a function of zenith and sun-pixel-angle was established from images on a clear day. A background image that would be expected for clear skies is then generated for each sky image based on the current solar zenith angle (Figure 15b). The CSL threshold is defined to be the red-blue-ratio (RBR) in the clear sky background image in addition to a threshold value. A pixel is classified as cloudy if its RBR (Figure 15c) is larger than this CSL threshold. In general, the method using the CSL is able to detect white opaque clouds accurately. However, within the circumsolar region, thick dark clouds cannot be identified since they have a lower RBR than the CSL threshold. Therefore, a sunshine parameter (Pfister, McKenzie, Liley, Thomas, Forgan, & Long, 2003) is used in addition to the CSL to improve cloud decision in the circumsolar region. The sunshine parameter is computed as the average RBR of the pixel area around the sun position (indicated in Figure 15a) and it is typically small when the sun is obscured. Pixels with RBR > sunshine parameter are classified as cloudy even if the CSL indicates otherwise. By adding the clouds detected using the CSL (Figure 15e) to the clouds detected using the sunshine parameter (Figure 15d), the overall cloud decision image is obtained (Figure 15f).

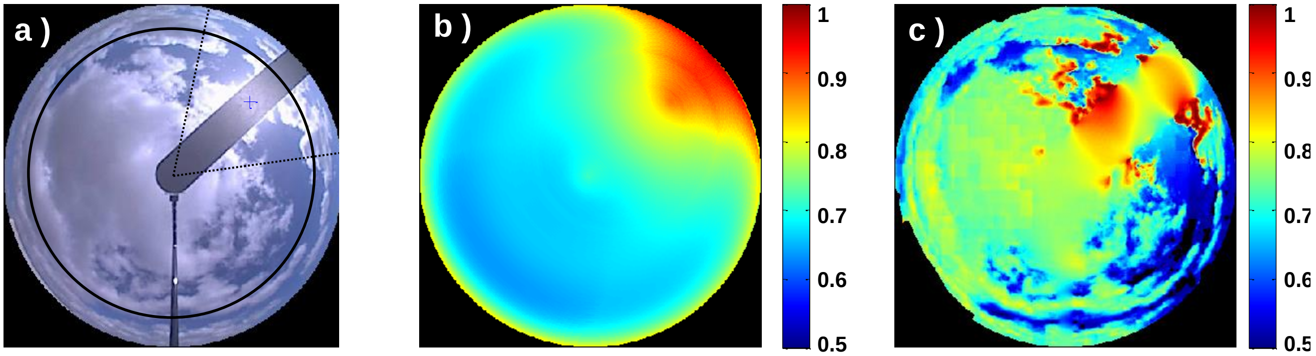

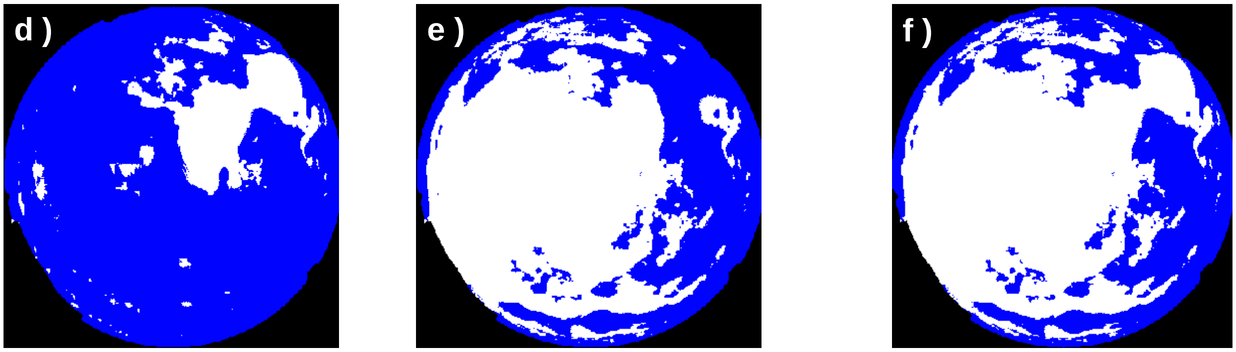

Figure 15 - Processing chain of a sky image on October 4, 2009 15:45:30 PST (a) to obtain the cloud decision image. The sunshine parameter is 0.85 and is evaluated around the sun position indicated by the blue cross. The dotted black lines show the borders of the circumsolar region defined as solar azimuth ±35° and the solid black line shows ZA at 65°. (b) Clear sky RBR (colorbar) background image plus the threshold. (c) RBR (colorbar) image. (d) Pixels in (c) with RBR > SP or (e) RBR > CSL threshold are assumed to be cloudy. (f) Shows the final cloud decision image. White areas are clouds and blue areas are clear skies.

The cloud decision image is transformed to sky coordinates (x,y) to geolocate clouds for cloud shadow mapping and forecasting using a geometric transformation that assumes constant cloud base height (CBH, $\Delta\mathrm{H}$) throughout the image. The sky coordinate cloud decision image (hereinafter cloud map) is restricted to ZA less than 65° since the coordinate transformation near the horizon is not valid (Beaubien & Freedman, 2001).

Cloud velocity and direction of motion is determined through the cross-correlation method (CCM) applied to two consecutive sky images (Hamill & Nehrkorn, 1993). Before applying the CCM, images are projected into sky coordinates to remove geometric distortion. The projected sky image is partitioned into subsets of pixels of equal size such that each subset is about 1% of the sky image area. The CCM finds the position that best matches each given subset of pixels in the previous sky image within the current image (Figure 16). The CCM yields a wind vector (direction and speed) with the largest cross-correlation coefficient that specifies the quality of the match. Assuming spatial homogeneity of cloud velocity, the vector field obtained through the CCM is further processed using several quality controls to yield an average cloud velocity across the image.

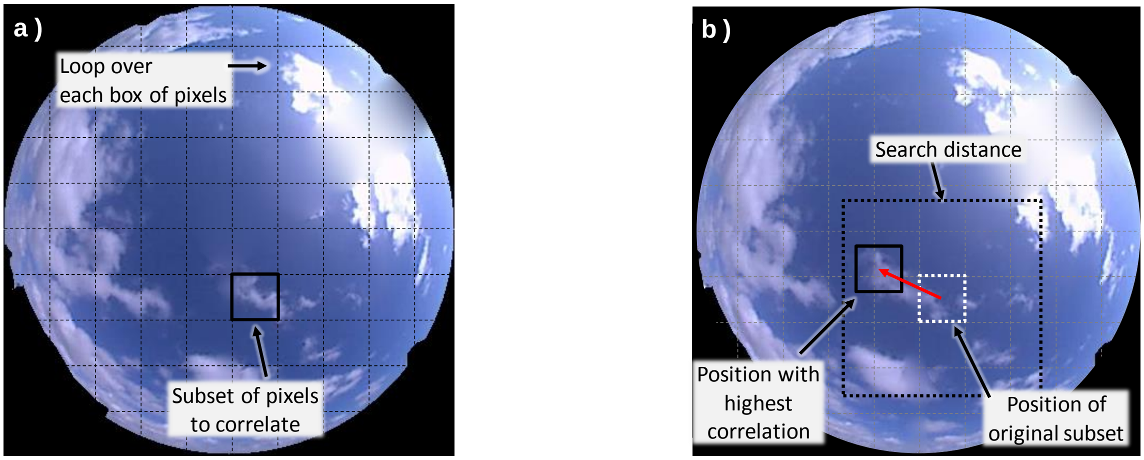

Figure 16 - Illustration of the cross-correlation method using two images on October 4, 2009 at 16:18:30 (a) and 16:19:00 PST (b). Each subset of pixels from (a) is correlated to (b) within a search distance. The location of the highest correlation is found and a motion vector is defined for each box. The cloud velocity determined from this pair of images was 5.2 m s^{-1}. While the method is illustrated here on a full color sky image, the method is actually applied to the coordinate transformed red channel image.

To forecast cloud cover, the cloud map at time t_o is advected at the speed and direction of the global vector determined from cross-correlating the images at time t_o and $t_o - dt$ ($dt = 30$ seconds). The quantity being forecast is the average GHI over one pixel of the Sky Imager. The size of the pixel (and its corresponding footprint on the ground) linearly increases with the cloud height and increases from the center of the image (straight overhead) to the horizon. For typical cloud heights the pixels near the center cover about 5 x 5 m and the pixels near the useable horizon (defined as 65^{o} zenith angle) are about 100 x 100 m.

4.3. Error Metrics

Since many inputs contribute to USI forecast accuracy, forecast validation was conducted in two parts in order to identify the main error sources and their effects on the final forecast. First, outputs from steps which are based solely on image analysis were analyzed to assess performance of the cloud decision and cloud motion algorithms. Second, time series constructed from 0-, 5-, 10-, and 15-minute forecasts were validated against measured data collected by the six ground stations. To avoid disproportional weighting of data near solar noon, validation was performed on clear sky index *kt* rather than GHI. Ground station *kt* time series were constructed by subsampling measured data at image capture times.

4.3.1. Validation using Actual Sky Image at Forecasted Time

As in (Chow, et al., 2011), two quantities were used to characterize the performance of image-based algorithms: matching error and cloud-advection-versus-persistence (cap) error. The *fh*-minute forecast cloud map generated at time t_0 was overlaid onto the actual cloud map at time t_0 + (*fh* min) in order to determine pixel-by-pixel forecast error, or ”matching error." No distinction between thin and thick clouds was made in determining matching error; a pixel is either cloudy or clear. Matching error was defined as:

$$e_{\mathrm{m}} = \frac{P_{false}}{P_{total}} \times 100\%, \qquad \text{Equation 1}$$

Cap error was computed in order to determine whether cloud advection improves forecast performance by comparing the number of falsely matched pixels of the *fh*-minute advection forecasts with those of an image persistence forecast, where the *fh*-minute persistence forecasts are obtained by assuming the cloud map at t_0 persists statically until *fh* minutes later. Cap error was therefore defined as:

$$e_{\mathrm{cap}} = \frac{e_{\mathrm{m}}}{e_{\mathrm{m,p}}} \times 100\%, \qquad \text{Equation 2}$$

which describes the forecast error obtained by cloud advection (Figure 17d) divided by the error obtained if the image at t_o was assumed to persist until $t_o + dt$ (no advection). An $e_{\mathrm{cap}} < 1$ implies that the cloud advection improves the forecast compared to persistence.

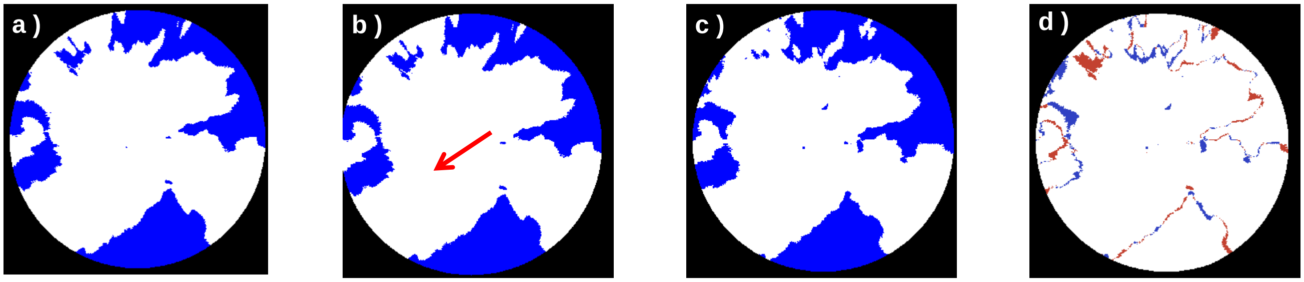

Figure 17 - The forecast cloud map (b) is produced by advecting the cloud map at time t_o (a) in the direction of the motion vector (indicated by the red arrow). To determine the forecast error (d), the future cloud map at time $t_o + 30$ seconds (c) is compared to the forecast (b). Blue and red colors in (d) show forecast errors (blue: pixel forecast cloudy and but actually clear; red: pixel forecast clear but actually cloudy) and white indicates accurate forecasts.

4.3.2. Validation using ground data

Four error metrics were used to assess the overall performance of the USI forecast system as a function of forecast horizon: relative root-mean-square error (rRMSE), relative mean absolute error (rMAE), relative mean bias error (rMBE), and forecast skill (FS). Relative metrics were obtained by normalizing by the temporal and spatial average of the observed *kt* for each day (kt^{obs}). Each metric was computed for every whole-minute forecast horizon (*fh* = 0, 1, …, 15 min) using instantaneous spatially averaged *kt* values averaged over the six stations. In the following equations, N denotes the total number of forecasts generated on a given day. The superscript "obs" denotes an observed value, and "fh" denotes forecast horizon in minutes. Therefore, kt_n^{fh} indicates the spatial average of the *fh*-minute-ahead clear sky index *kt* forecasts generated at each ground station at time t_n corresponding to the nth forecast of the day.

$$\mathrm{rRMSE}(fh) = \sqrt{\frac{1}{N}\sum_{n=1}^{N}\left(kt_n^{fh} - kt_n^{\mathrm{obs}}\right)^2} \times \frac{100\%}{\overline{kt}^{\mathrm{obs}}} \qquad \text{Equation 3}$$

Equation 4

Equation 5

In order to quantify the performance of USI forecasts, a forecast skill was calculated for each forecast horizon. (Marquez & Coimbra, Proposed metric for evaluation of solar forecasting models, 2013) found that the ratio of forecast model RMSE to persistence model RMSE is a measure of general forecast skill that is less affected by local solar meteorology and can therefore be used to intercompare forecast results. The persistence forecast was generated by assuming ground station measured kt at time t_n persisted for the entire forecast window (i.e. kt(persistence forecast) = $kt^{obs}(t_n)$). Here, rMAE was used to compute forecast skill instead of rRMSE due to the linear nature of rMAE. Thus, forecast skill FS was defined as:

$$\mathrm{FS}(fh) = 1 - \mathrm{rMAE}(fh) / \mathrm{rMAE}_p(fh)$$ Equation 6

Positive values of FS therefore indicate the USI forecast was superior to the ground station persistence forecast, with a maximum possible value of 1. As an indicator of sample size, the average number of ground stations covered by the shadow map for each forecast time series was computed. Error metrics were not computed for time series showing average number of stations covered less than 1, which indicates a lack of forecast data for the day and forecast horizon in consideration. A small number of stations covered can occur due to low cloud height or unfavorable cloud motion (fast speed or north-easterly direction).

4.4. Forecast Results

4.4.1. Image-based performance

Summaries of image-based forecast performance are presented in Table 2 for forecast horizons of 30 seconds and 5 minutes, and in Figure 18 for all forecast horizons. The image-weighted average 5-minute cap error is 91.9%, which implies 5-minute advection forecasts performed better than image persistence over the entire month. Inspection of daily 5 min cap errors reveals that 11 of 22 days exhibited cap errors higher than 100%. Ergo, pure advection of clouds is not appropriate for all sky conditions. The image-weighted average 30-second cap error of 67.0% is larger than cap errors in (Chow, et al., 2011), which ranged from 45.0% to 54.6%. The larger validation set analyzed in this paper (31 consecutive days versus 4 ideal days) presented a wider variety of cloud conditions, causing a greater range in cap errors and a larger (but more representative) average cap error. Additionally, new features of the USI such as thin cloud detection and an unobstructed circumsolar region (area immediately surrounding sun) result in more accurate kt assignment and greater visibility of the sky dome, but increase cap errors. Since thin cloud detection is very sensitive to the CSL threshold, and that threshold is not as distinct from typical clear sky RBRs as the thick cloud threshold, thin cloud detection fluctuates more from image to image for example, due to sun obstruction or stray light in the optics. Cloud decision errors in the circumsolar region, along with the sun obstruction CSL bypass, also cause fluctuations in the number of cloudy pixels between images. These effects increase the total number of false pixels in both advection and image persistence forecasts, causing their ratio to be closer to unity.

Table 2 Mean and standard deviation of matching errors, along with total daily cap errors (Equation 3 and Equation 4) for fh = 30 s and fh = 5 min. Reported average cloud speed is a scalar average.

Date	e_m(%)		Std. e_m(%)		e_{cap}(%)		Avg. cloud fraction (%)	Avg. cloud speed (m/s)	Avg. CBH (m)
	30 s	5 min	30 s	5 min	30 s	5 min			
Nov 01	4.6	15.5	1.6	7.5	90.8	102.9	45.0	3.5	1798
Nov 02	3.9	12.3	1.9	6.8	90.6	96.0	12.0	14.7	5796
Nov 03	6.1	28.1	2.8	17.2	62.3	379.6	8.7	23.3	1340
Nov 04	-	-	-	-	-	-	0.0	-	-
Nov 05	-	-	-	-	-	-	0.0	-	-
Nov 06	-	-	-	-	-	-	0.6	-	-
Nov 07	5.0	37.2	1.8	18.4	65.3	240.0	54.9	3.7	349
Nov 08	4.3	15.2	2.5	8.4	64.5	79.4	64.4	2.5	769
Nov 09	4.6	19.0	2.2	8.4	49.7	78.7	62.8	8.1	1522
Nov 10	4.1	19.1	1.7	6.1	37.3	67.3	20.2	9.6	1372
Nov 11	-	-	-	-	-	-	0.0	-	-
Nov 13	-	-	-	-	-	-	0.0	-	-
Nov 14	3.9	12.7	2.7	6.3	54.4	57.4	35.5	20.2	5486
Nov 15	-	-	-	-	-	-	99.1	-	-
Nov 16	2.4	10.9	1.7	5.2	43.0	63.0	22.0	12.1	2606
Nov 17	3.4	16.6	1.4	6.3	53.8	83.7	27.9	4.8	1269
Nov 18	6.7	23.1	2.9	11.3	69.4	99.2	54.8	6.9	1058
Nov 19	-	-	-	-	-	-	2.5	-	-
Nov 20	7.5	29.4	3.1	13.8	52.4	119.2	7.2	62.4	2980
Nov 21	7.8	17.8	6.1	10.1	82.9	90.5	37.0	37.5	6045
Nov 22	6.1	31.3	2.6	18.6	66.4	264.6	14.6	3.4	402
Nov 23	10.8	20.2	4.8	13.0	103.4	117.9	49.1	7.8	1695
Nov 24	7.7	21.0	6.7	21.5	101.0	101.0	6.8	0.1	274
Nov 25	6.3	20.4	4.2	17.6	78.6	106.1	44.7	2.4	429
Nov 26	4.7	15.6	3.2	8.2	83.5	100.4	42.9	14.7	4269
Nov 27	3.6	8.7	3.7	5.8	68.8	48.0	86.6	0.9	488
Nov 28	5.6	21.3	5.4	11.8	98.1	144.0	40.5	11.7	2563
Nov 29	-	-	-	-	-	-	97.7	-	-
Nov 30	-	-	-	-	-	-	99.0	-	-
Dec 01	6.3	17.0	4.4	14.5	95.3	103.2	52.2	26.6	2364
Dec 02	3.6	15.9	1.8	8.4	50.7	81.6	58.6	3.5	546
Mean*	5.0	18.9	2.8	12.4	67.0	91.9	36.6	11.2	1991

* Mean values are weighted by number of images.

Table 3 USI nowcast aggregate error metrics. Average number of stations covered by the nowcast shadow map is listed in the second column. This value is an indicator of the sample size used in the computation of error metrics. Average station cover of less than 1 is due to low clouds (small projected shadow map), large cloud speed (advection out of domain), or unfavorable solar azimuth/zenith or cloud direction that project the cloud field away from the area where ground stations are located. Days with average cloud fraction < 5% are indicated in italics.

	Avg # St.		rRMSE		rMBE		rMAE		$rMAE_p$	FS
Date	0	5	0	5	0	5	0	5	5	5
Nov 01	5.9	5.9	23.4	24.3	2.7	0.4	14.1	15.1	9.9	-0.5
Nov 02	6.0	6.0	14.5	13.3	-0.1	-1.0	6.3	6.4	4.9	-0.3
Nov 03	5.9	3.9	7.7	9.6	-0.7	0.3	3.8	4.5	3.3	-0.4
Nov 04	*6.0*	*4.3*	*2.2*	*0.4*	*0.0*	*0.1*	*0.3*	*0.3*	*0.3*	*-0.2*
Nov 05	*6.0*	*2.9*	*2.9*	*0.7*	*0.0*	*0.2*	*0.5*	*0.4*	*0.2*	*-1.4*
Nov 06	*5.8*	*5.8*	*4.2*	*4.7*	*0.7*	*0.6*	*1.4*	*1.7*	*0.6*	*-1.9*
Nov 07	4.1	2.6	18.1	18.0	10.9	4.6	12.3	11.4	7.3	-0.6
Nov 08	5.8	5.8	38.6	42.8	10.6	5.7	28.7	33.5	27.8	-0.2
Nov 09	6.0	5.8	26.6	29.4	-6.2	-6.6	17.5	21.6	24.7	**0.1**
Nov 10	6.0	5.8	15.4	17.5	-2.2	2.8	10.0	11.2	15.6	**0.3**
Nov 11	*6.0*	*6.0*	*0.6*	*0.8*	*-0.2*	*-0.2*	*0.4*	*0.6*	*0.2*	*-1.6*
Nov 13	*6.0*	*6.0*	*0.6*	*0.8*	*-0.2*	*-0.3*	*0.5*	*0.6*	*0.3*	*-1.2*
Nov 14	6.0	5.9	19.4	21.7	-6.3	-11.7	14.2	15.6	12.5	-0.3
Nov 15	6.0	6.0	21.2	27.6	-3.6	-3.2	6.8	16.4	13.7	-0.2
Nov 16	6.0	6.0	14.1	14.5	-3.5	-4.2	6.8	7.5	8.6	**0.1**
Nov 17	5.8	5.7	25.1	25.9	-1.9	-1.5	16.9	17.3	13.5	-0.3
Nov 18	5.9	5.4	23.0	24.5	-5.0	1.8	16.2	18.7	18.5	**0.0**
Nov 19	*5.9*	*4.2*	*7.8*	*6.9*	*-0.8*	*0.0*	*3.0*	*2.6*	*3.4*	*0.2*
Nov 20	5.6	0.2	10.6	-	0.1	-	4.5	-	-	-
Nov 21	6.0	5.9	20.0	21.6	3.4	4.0	6.3	8.2	4.0	-1.1
Nov 22	5.1	4.5	10.3	10.8	1.9	-2.2	4.9	5.5	4.5	-0.2
Nov 23	2.7	2.7	13.2	14.8	5.0	3.8	9.8	10.8	5.9	-0.8
Nov 24	5.5	5.6	5.1	5.0	0.3	0.4	2.8	2.7	1.9	-0.4
Nov 25	4.8	4.1	10.5	17.9	1.1	0.5	4.3	8.5	4.1	-1.1
Nov 26	6.0	5.8	18.4	22.6	1.0	-7.4	12.0	14.5	12.8	-0.1
Nov 27	5.7	4.8	27.1	34.2	2.6	3.5	17.3	24.4	18.2	-0.3
Nov 28	6.0	5.9	14.6	18.2	0.6	-0.4	6.1	9.8	6.7	-0.5
Nov 29	4.3	4.4	35.4	38.4	5.3	2.4	17.9	24.3	16.2	-0.5
Nov 30	4.2	4.1	52.6	67.9	23.4	27.6	27.8	43.2	17.2	-1.5
Dec 01	5.6	5.5	24.9	27.4	1.5	6.1	17.9	20.2	13.6	-0.5
Dec 02	5.8	5.6	11.4	12.7	2.0	0.7	5.6	7.7	6.5	-0.2
Mean*	5.5	4.9	17.7	20.0	1.7	1.4	9.1	11.1	8.6	-0.3

* Mean values are weighted by number of forecast data points.

These effects increase the total number of false pixels in both advection and image persistence forecasts, causing their ratio to be closer to unity. Cloud map matching metrics are shown in Figure 18 versus forecast horizon. Matching error can be seen to increase mostly monotonically with forecast horizon as static cloud advection is increasingly less valid; cap error also increases with forecast horizon, but exhibits a peak at a forecast horizon of 9 min. The number of images containing partial overlap by the advected cloud map from fh min prior is seen to decrease sharply from 8 min forecast horizon onwards. This decrease in image sample size is attributed to advection of the cloud map out of the initial field-of-view. At a forecast horizon of 15 minutes, approximately 30% of images have been advected out of scene, indicating forecast horizon limitations of the USI technique. To identify regions of high cap error, a map of monthly cap errors at 5 min on a projected cloud map is shown in Figure 19a. Plotting cap error vs. image zenith angle (IZA) (Figure 19b) shows cap errors mostly below 100% for all forecast horizons, with an approximately monotonic increase at IZAs > 70°. Separating the cloud map into top and bottom halves (Figure 19c & Figure 19d), it is clear that there is a cap error reduction between 10- and 15-min forecast horizons mostly in the bottom half of the cloud map. Additionally, the bottom half of the cloud map exhibits higher cap errors at high IZAs than the top half. This discrepancy can be attributed to difficulty in obtaining accurate cloud decision within the circumsolar region. During the month of November, the position of the sun is solely contained in the bottom half of the cloud map (extreme solar zenith and azimuth angles are 47.6° and 116.8° - 244.6°, respectively). Morning cloud cover is frequent in the San Diego region (e.g. marine layer clouds), so clouds frequently cover or pass over the sun following sunrise, leading to concentration of cap errors in the southeastern quadrant. Combined with prevailing westerly winds over San Diego, these high cap error regions are often advected out of scene between forecast horizons of 10 and 15 min. This corroborates the reduction in cap error after a forecast horizon of 9 min as previously observed in Figure 18.

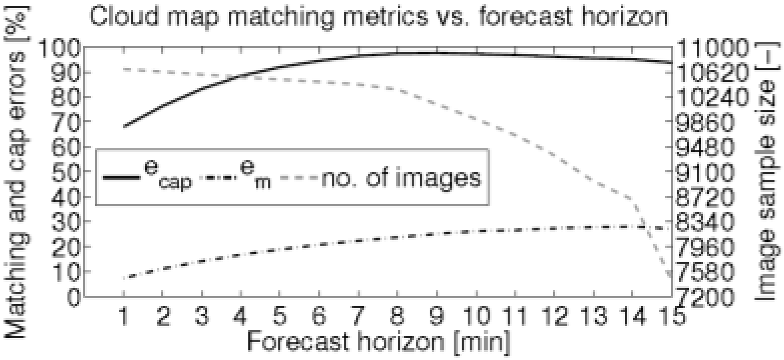

Figure 18 - Cloud map matching metrics versus forecast horizon. Metrics are averaged across all images over 31 days, i.e. not the mean of the daily means in Table 2.

Considering high cap errors are concentrated at high IZAs (particularly in the southeast quadrant), we arrive at an interesting conclusion: depending on the SZA, more accurate regions of the cloud map may cast shadows on the footprint following advection, instead of information from the higher-error cloud map perimeter. Furthermore, advection of high cap error regions out of scene (e.g. advection of southeast quadrant by prevailing westerly winds) leads to an inability to ray trace clouds from the high cap error region, resulting in no forecast for affected stations, rather than an erroneous forecast.

Despite the challenges presented by the situations outlined above, daily cap errors were below 100% for 20 out of 22 days for 30 second forecasts and 11 out of 22 days for 5-minute forecasts. This suggests the underlying principles and assumptions of the cloud decision and cloud velocity algorithms are consistently valid. Days with cap error exceeding 100% demonstrated unfavorable phenomena, such as stationary conditions (advection performs worse than persistence) and rapidly deforming clouds (cap error near 100%, as advection performs just as poorly as persistence). On the other hand, the cumulus clouds present on the day with the smallest cap error (Nov 10) presented heterogeneous cloud cover moving at uniform velocities, which is the ideal scenario for the cloud motion algorithm, as the sharp edges characteristic of cumulus clouds allow the cross-correlation method to obtain robust results. Statically advecting cumulus clouds conform to the forecast assumptions, and cumulus clouds are optically thick, so few thin pixels were present in each cloud decision image, thereby minimizing the fluctuations in cloudy pixels caused by thin cloud classification. Hence, Nov 10 was an ideal day for USI forecast performance, and its average 30 sec (5 min) cap error of 37.3% (67.4%) is superior to the smallest cap errors for similarly ideal days in (Chow, et al., 2011) of 45.0% (70.3%).

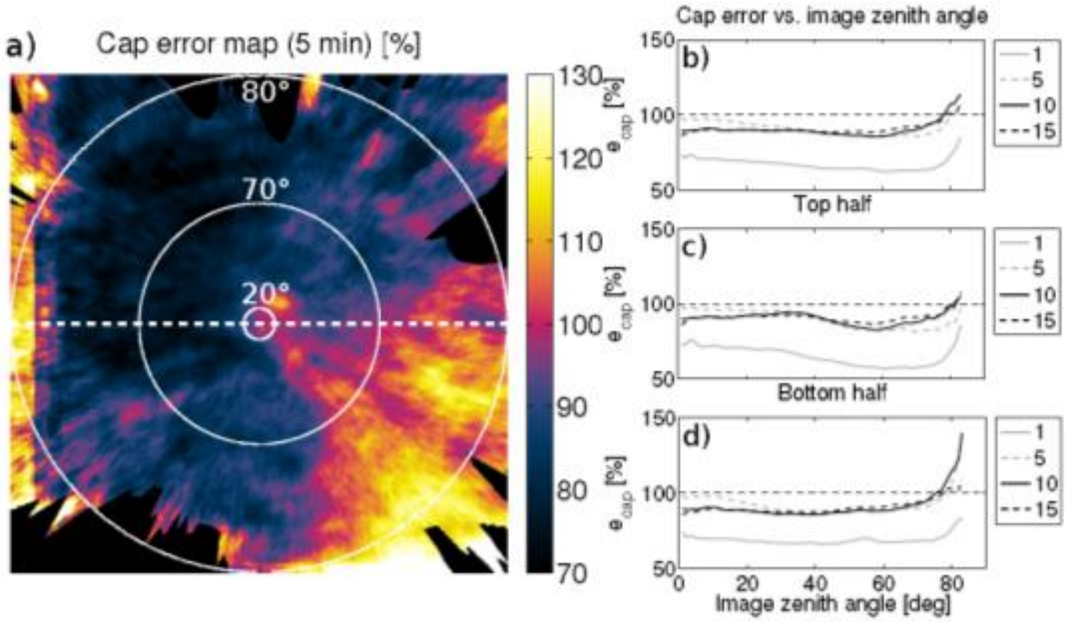

Figure 19 - a) Monthly cap error shown on projected cloud map for 5 min forecast horizon, with image zenith angle isolines at 20°, 70°, and 80°. b) Cap error vs. image zenith angle for forecast horizons of 1 min (solid gray), 5 min (dashed gray), 10 min (solid black), and 15 min (dashed black). c) Same, but for top region of cloud map. d) Bottom region of cloud map.

4.4.2. USI performance for irradiance forecasting

A graph of bulk error metrics as a function of forecast horizon for all 31 days is shown in Figure 20. The nowcast (0-minute forecast) shows an rMAE of 9% and forecast errors increase with forecast horizon. Detailed error metrics for each day are tabulated in Table 3. Although ground station persistence forecast outperforms the USI in terms of bulk error metrics, this is largely a result of inaccuracies in estimating cloud optical depth in clear or cloudy conditions. On the other hand, the USI offers the ability to predict ramp events. Graphical representations of USI forecasts versus measured data are therefore more indicative of forecast value, as the ability to forecast timing and magnitudes of ramp events can be shown. For this reason, daily overviews of USI forecast bias errors have been graphically compiled for nowcasts and 5-minute forecasts (Figure 25). Since we forecast the average GHI at all sites, large changes in forecast GHI are due to sudden shading of many or all sites by thick clouds, while small changes indicate shading of one site or that thin clouds are shading multiple sites. In the following sections, forecast periods of various forecast horizons will be shown to critically appraise Sky Imager forecasting.

Nowcast of sky conditions (0-minute forecast)

The 0-minute forecast, or nowcast is of particular interest in the validation process. Since nowcasts are not influenced by cloud velocity, the accuracy of cloud decision and projection algorithms can be verified. USI nowcast time series for two days demonstrating high irradiance variability are shown in Figure 21. November 10 (Figure 21a) illustrates an accurate nowcast which matches most of the day's variability in both timing and magnitude, indicating excellent performance of the cloud decision algorithm, as well as accurate cloud projection as a result of accurate METAR CBH and geometric calibration. November 17 (Figure 21b) also shows agreement between USI nowcast and measured *kt*, save for some periods in the early morning and late evening. Most of the errors from morning to afternoon can be attributed to cloud decision errors (most notably the underprediction of irradiance between 08:00 and 08:40 PST), when thin clouds were over-conservatively classified as thick clouds. The over- and underprediction of kt after about 14:00 PST resulted from a CBH error. METAR suggested 457 m at both KNKX and KMYF stations while visual examination of the images indicated altocumulus clouds that typically exist above 2 km. The result of an underestimated CBH was a projection error leading to shadow map contraction, as shadow map extent = CBH cos 80°. To illustrate this effect, a contracted shadow map generated at 14:07:30 PST at a CBH of 457 m (Figure 21d) is shown beside a correct morning shadow map (Figure 21c). In Figure 21c, irradiance measurements reflect ground station cloud shadow cover. Figure 21d, however, shows four stations in the north of the domain measuring lower irradiance than HUBB (southwest), despite the shadow map showing clear skies over all stations. In this case, cloud shadows were actually covering all four stations in the north, but cloud map projection at an incorrect CBH led to an underestimation of cloud shadow coverage.

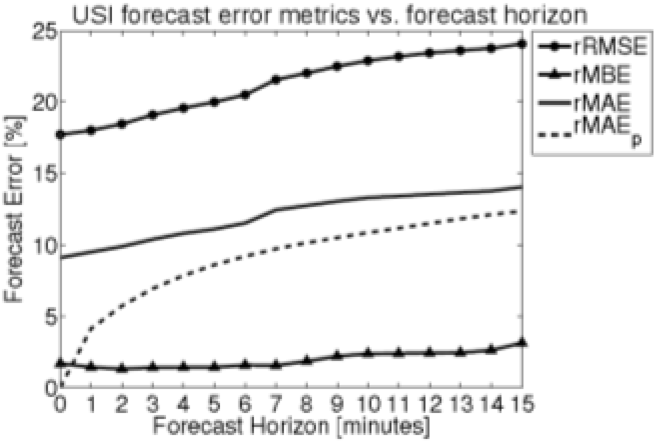

Figure 20 - USI error metrics for all 31 days vs. forecast horizon.

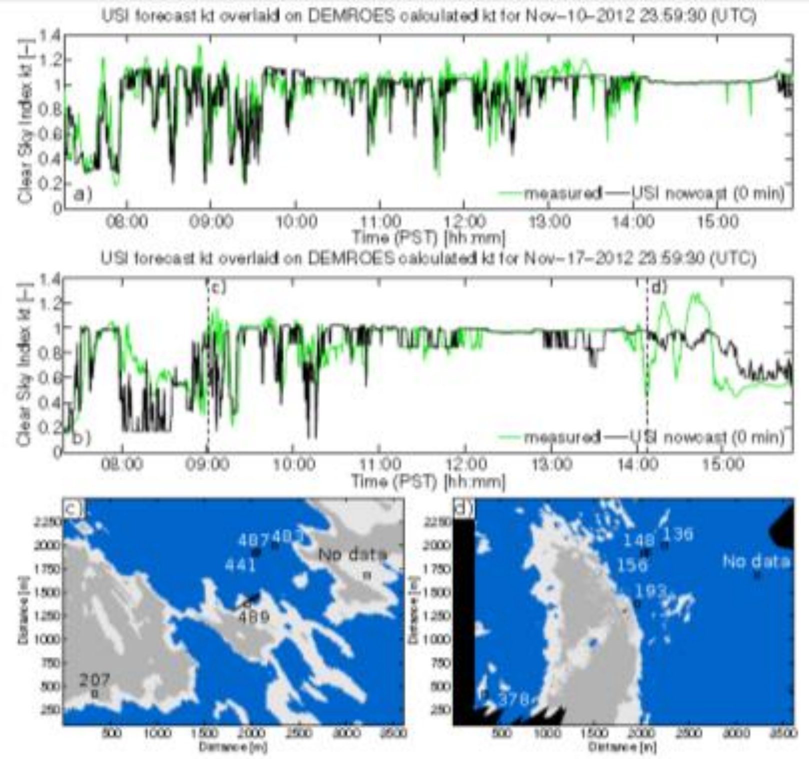

Figure 21 - USI nowcast and measured kt averaged across all ground stations covered by the shadow map for (a) November 10, 2012 with cumulus clouds and (b) November 17, 2012 with cumulus clouds (< 2 km) followed by altocumulus (2 km to 7 km). Dashed lines indicate times corresponding to c) and d). c) Shadow map (blue: clear sky, light gray: thin cloud, dark gray: thick cloud, black: no data) corresponding to 09:07:30 PST illustrating accurate shadow map. Ground station locations are marked by black boxes, with measured irradiance printed nearby in W m^{-2}. Cloud velocity is indicated by a black vector extending from the center of the shadow map. d) Shadow map corresponding to 14:07:30 PST illustrating compressed shadow map due to low cloud height of 457 m.

The primary factors affecting nowcast accuracy were found to be cloud decision within the circumsolar region and CBH measurements. Due to the geometry of ray tracing, sky conditions in the circumsolar region will always affect the region immediately surrounding the physical location of the USI for nowcasts and short-term forecasts. An erroneous reduction in assignment of "thin" to a thick cloud that occasionally occurs in the circumsolar region (detailed in 5.1) therefore introduces a positive bias into nowcasts for stations in close proximity to the USI. Nowcast errors may also result from an expansion or contraction of the cloud and shadow maps caused by a CBH error in the METAR data. As measured CBH increases, the size of the shadow cast by a cloud subtending a certain solid angle increases. A graphical overview of nowcast GHI bias errors with respect to measured GHI for November 10 and 17 is presented in Figure 22 to illustrate the relationship between *kt* and GHI. Similar plots for the entire data set are compiled in Figure 25. Periods exhibiting a CBH mismatch between METAR data (either due to multiple cloud layers or erroneous METAR data) and observed clouds are explicitly marked by ≠, and overforecasts (black areas) appear more common during these conditions. For Nov 17 in particular, the worst case occurs where the cloud projection error causes the cloud field to be (i) out of phase and (ii) smaller than in reality causing it to cover only one site at a time while the actual cloud field covered 4 sites during the episode around 14:20 PST. The error was further increased by significant cloud enhancement that is presently not modeled in our algorithm.

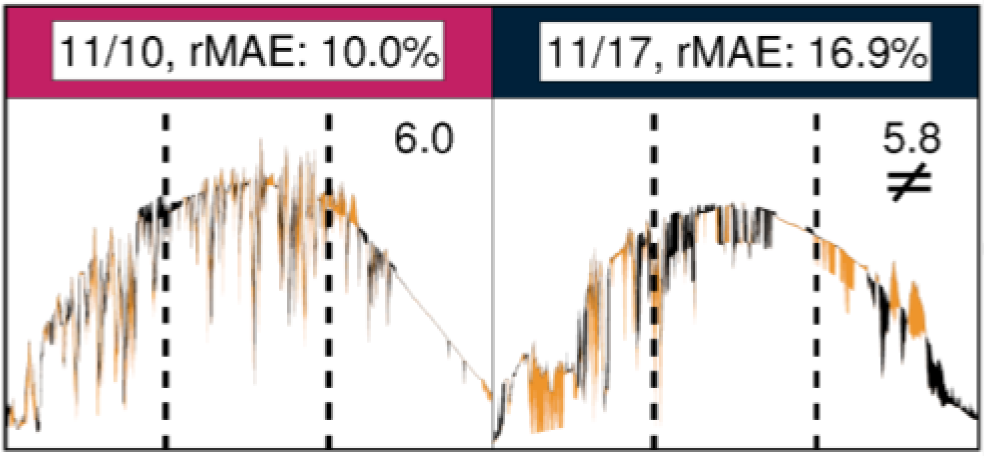

Figure 22 - Bias errors between USI nowcast GHI & Measured GHI

Figure 22 represents bias errors between USI nowcast GHI and measured GHI averaged across all 6 ground stations for Nov 10 and 17, 2012. Labels are color coded based on rMAE, ranging from 0% (white) to 20% (black). Note that while plots shown are of GHI, error metrics reported were computed using clear sky index *kt*. Black regions represent overprediction, while orange regions represent underprediction. The average number of stations covered by the shadow map throughout each day is reported in the top right corner of each plot. A ≠ marks periods with significant mismatch between observed clouds and METAR CBH. Vertical dashed lines divide days into morning, midday, and afternoon.

4.4.3. 5 to 15-minute forecast

Five-, ten-, and fifteen-minute forecasts for four partly cloudy days will now be examined in greater detail to examine the USI's ability to predict major ramp events and visualize error patterns. Sky conditions on Nov 16 (Figure 23a, e_{cap} of 63.0% at 5 min) consisted of a mix of clear skies and intermittent broken altocumulus clouds. Much of the variability in the morning was captured, but most notably, the large ramp events at 10:30 PST (down ramp) and 11:45 PST (up ramp) were captured both in timing and magnitude (11:45 event only). A smaller isolated ramp event around 15:30 PST was also correctly predicted. Nov 18 (Figure 23b, e_{cap} 99.2% at 5 min) exhibited an average cloud fraction of 55%, but consisting of a mix of low-level cumulus, mid-level altocumulus, and high-level cirrus clouds, as well as a brief overcast period in the morning. Although many high-frequency ramps were missed, the 5 minute USI forecast accurately predicted many of the larger ramp events well across such a large variety of sky conditions. In addition to accurate cloud decision and CBH, forecast performance increasingly depends upon accurate cloud motion as forecast horizon increases. Inaccurate cloud velocity or changes to cloud velocity during the forecast will cause errors to increase. On the other hand, a source of error reduction is that, depending on CBH and cloud velocity, circumsolar cloud decision errors may be advected out of the footprint and no longer affect irradiance estimates. Generally, we observed that provided a reasonably accurate nowcast was produced, the performance of 5 minute USI forecasts is promising. Four out of 24 days exhibited a forecast skill of 0 or greater (Table 3). A graphical overview of 5-minute forecast bias errors is shown in Figure 25. Compared to nowcast bias errors, periods suffering from a CBH mismatch showed a larger increase in bias errors than periods with more accurate CBH measurements, further highlighting the importance of accurate CBH data.

The 10-minute forecast time series for Nov 14 (Figure 24a, e_{cap} of 67.7% at 10 min) shows agreement between forecast and measured *kt* ramp shapes for most of the day. Many of the timings of larger ramp events were predicted correctly, but the magnitudes of the ramps showed occasional forecast underprediction caused by conservative CSL thresholds—most notably between 11:00 and 12:00 PST, and especially after 13:30 PST.

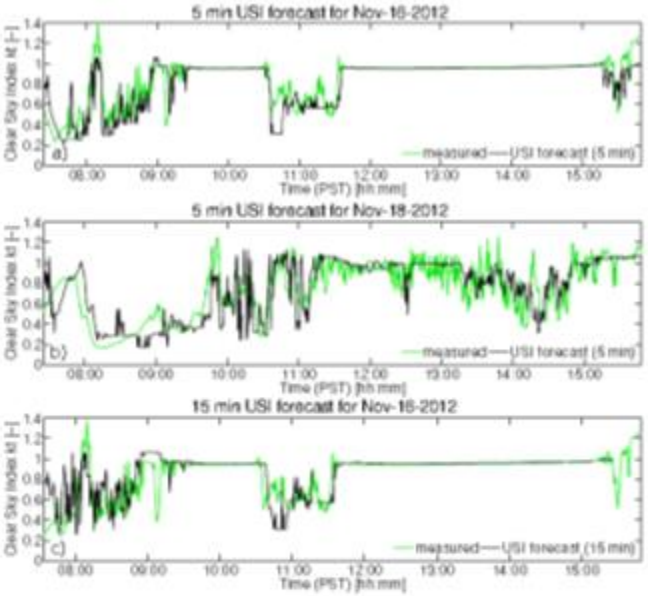

Figure 23- USI 5-minute forecast versus measured kt averaged across all ground stations for: a) November 16, 2012. Clear skies, with intermittent altocumulus clouds. rRMSE: 14.5%, FS: 0.1. b) November 18, 2012. Overcast, followed by varying partly cloudy conditions (cumulus, altocumulus, and cirrus). RMSE: 24.5%, FS: 0.0. c) USI 15-minute forecast versus measured kt averaged across all ground stations for November 16, 2012. Clear skies, with intermittent altocumulus clouds. rRMSE: 17.1%, FS: 0.3.

Despite small cap errors (e_{cap} of 47.0% at 10 min), the performance of the USI on November 27 was especially poor, and the 10-minute forecast time series (Figure 24b) illustrates the different types of errors that impact forecast accuracy. Although the high USI cloud fraction (> 95%) from morning until 10:00 PST indicated overcast conditions, the cloud field was visibly textured and appeared to be moving with an apparent velocity (averaging about 4.6 m s^{-1} at 457 m beginning around 09:00 PST as calculated by the cloud motion algorithm). The high velocity relative to CBH caused the shadow map to be advected out of the sensor array footprint at a forecast horizon of 10 min for most of the duration of overcast conditions. An overprediction of kt occurred between 08:30 and 09:05 PST, because an erroneous METAR CBH reading of 6096 m caused expanded shadow maps leading to thin clouds on the horizon to be projected into the forecast domain.

The overcast conditions then cleared, revealing a layer of thin cirrus clouds which are typically at a height greater than 7 km, but METAR CBH reports remained at 488 m for the rest of the day, which were inconsistent with the cloud types observed. The resulting CBH mismatch caused cloud cover to be inaccurately represented both in size and position, causing almost every ramp event of interest to be missed. Hemispherical cloud coverage during this period exceeded 95% (consisting of cirrocumulus and cumulus clouds), so the thick cloud class was assigned the median measured *kt* of the past minute. With 95% cloud cover, forecasts are almost entirely based on changes in cloud *kt*, so the resulting forecast is essentially a 10-minute time shift of the measured *kt* (similar to persistence forecast). The high measured *kt* values during this time indicate cloud enhancement with an increase in diffuse solar radiation caused by scattering of the solar beam on the base of the cloud field due to the sun's low position on the horizon (solar zenith angle was about 73°).

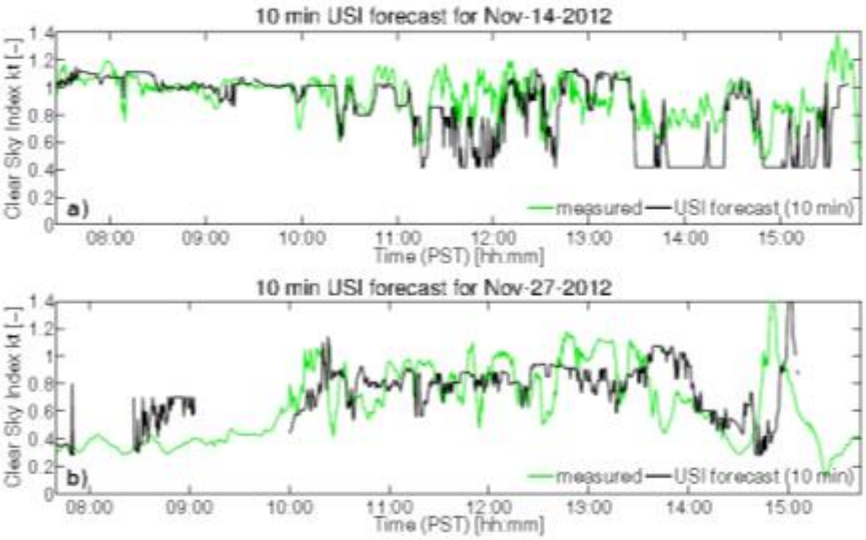

Figure 24 - USI 10-minute forecast versus measured kt averaged across all ground stations for: a) November 14, 2012. Cirrus transitioning into cirrocumulus around noon. rRMSE: 23.4%. FS: -0.1. b) November 27, 2012. Overcast in the morning, followed by partly cloudy conditions (cirrus, cirrocumulus, and cumulus), with occasional presence of multiple cloud layers for the rest of the day. rRMSE: 40.2%, FS: -0.3.

As discussed in Section 4.1, approximately 30% of images have been advected out of scene at a forecast horizon of 15 minutes, leading to less forecast data points available. The remaining images exhibited a monthly cap error of 93.7%, even showing slight improvement over the 10 minute monthly cap error of 97.2%. When forecast data is available, 15-minute GHI forecasts perform similarly to 10-minute forecasts. At a forecast horizon of 15 minutes, persistence forecasts do not provide much valuable information, whereas the USI may be able to forecast major ramp events 15 minutes in advance, as on Nov 16 (Figure 23, e_{cap} of 70.3% at 15 min), wherein the large ramp event at approximately 10:45 PST (cf. 5 min forecast in Figure 23) was predicted even at the 15 minute forecast horizon.

4.5. Summary of Sources of Forecast Error

Circumsolar region optical depth reduction: Cloud decision errors are more prevalent within the circumsolar region. Since forward scattering of sunlight by aerosols causes clear sky RBR to increase within the circumsolar region, the clear sky RBR stored in CSLs is elevated within the circumsolar region. Additionally, the intensity of the solar beam causes saturation in pixels immediately within the solar disk, resulting in a clear sky RBR of unity (which is much larger than the clear sky RBR in other regions). These factors tend to reduce the ΔRBR of clouds and therefore the detected optical thickness of clouds within the circumsolar region.

Errors due to this effect are difficult to quantify, as thick clouds falsely classified as thin clouds will not impact matching and cap errors (as defined here), though overprediction of forecast irradiance results if circumsolar thin clouds cast shadows on the site footprint.

Cloud evaporation and formation: Periods of cloud evaporation and/or formation on timescales of a few minutes are a common error source. Since the present advection algorithm of the USI does not possess any ability to model these physical processes, these periods will inevitably cause a larger matching error, as was the case on Nov 23, 26, and Dec 1.

Perspective errors: Occasionally, a cloud away from the image center may partially occlude a cloud immediately behind, obstructing a small gap of clear sky. This “merged cloud" effect is predominantly observed in low-level clouds of significant vertical extent, such as cumulus clouds. A related source of error introduced by these types of clouds involves a slight overestimation in cloud size of clouds farther away from the image center, due to the assignment of cloud sides as cloud bottoms. These perspective errors, through obstruction and distortion effects, slightly increase matching errors, and appear to be partly responsible for the concentration of high cap errors at high IZAs shown in Figure 19. One could statistically correct for these errors, i.e. shrink cloud sizes, if the vertical extent of clouds was known.

Heterogeneous cloud velocity: Errors are caused by the cloud motion algorithm when the assumption of uniform cloud motion across the USI's field-of-view does not hold. Heterogeneous cloud velocity is typically due to the presence of multiple cloud layers, but can also be caused by variations in topography that cause channeling of flow or cloud turbulence. The cloud vector quality control in the cloud motion method is designed to eliminate cloud velocity vectors from the cloud layer with smaller sky coverage and represent the predominant cloud velocity. More rarely, rotational motion (e.g. caused by horizontal shear, etc.), even over the relatively small scale of the USI view, will cause the linear cloud advection hypothesis to break down.

Stationary sky conditions: One albeit rare source of cap error was the presence of stationary clouds caused by, for example, rapid formation of clouds in a fixed position in the sky and subsequent evaporation occurring on timescales of a few minutes. Although clouds are traveling with the velocity of the underlying flow field, strong updrafts (especially in weak winds) can induce local forcing that balances the background flow, causing stationary clouds. Another example of a stationary condition is the occurrence of haze, which typically forms in calm conditions, when the lower atmosphere is poorly mixed. The relatively large aerosol particles contained in haze scatter light similarly to water droplets in clouds. As a result, the RBR signature of haze is similar to that of thin clouds, so haze is classified as such. Indeed, ground station data shows measurable irradiance attenuation during hazy conditions. However, due to the circumsolar cloud detection bias detailed in 5.1, a false clear region almost always results near the solar disk, causing a large matching error when advected, as well as a positive bias in irradiance forecasts. Because of the stationary nature of these cloud decision errors, cloud motion cannot improve over persistence forecast, leading to cap errors near or in excess of 100%, such as on Nov 24 and Nov 28.

Influence of cloud base height: Accurate cloud base height (CBH) measurements are critical to the accuracy of USI forecasts. Here, CBH was obtained from an off-site METAR station in a heterogeneous coastal environment, which introduces errors. Instead, more accurate CBH could be obtained from ceilometers or image stereography using two Sky Imagers. Erroneous CBH values lead to both incorrect projection of cloud cover within the forecast domain and incorrect physical cloud velocity. As the size of the shadow map scales linearly with CBH, and CBH typically ranges by an order of magnitude, CBH introduces errors in both the size of the cloud shadows within the forecast domain ("shadow map") and in the locations of clouds within the forecast domain. Because the shadow map is always centered about the physical location of the USI prior to advection, for nowcasts these cloud shadow errors more strongly affect stations located farther from the USI. Since physical cloud velocity is determined by converting cloud pixel velocity (approximately angular velocity with respect to physical location of USI) into an equivalent ground speed based on CBH, the resulting physical velocity will be overestimated if the METAR CBH is much higher than that of the clouds from which pixel velocity was computed (and vice versa). This cloud speed error scales linearly with the ratio of actual versus METAR CBH. Additionally, ground shadows obtained by ray tracing are affected when combined with an erroneous CBH, leading to errors in both cloud shadow position (dependent upon solar zenith angle) and size. An example was illustrated in (Figure 21c & Figure 21d). Furthermore, because the UCSD footprint consisted only of six point sensors (none of which were collocated with the USI) extremely low CBH measurements result in zero station coverage and therefore no forecast data (gray areas in Figure 25), as on Nov 23. However, the low CBH measurements on Nov 23 do not necessarily constitute a METAR mismatch, as fog-like conditions were intermittently present at the USI.

4.6. Conclusions and future work

This paper comprehensively demonstrates Sky Imager irradiance forecasting using state-of-the-art imaging technology for areas of ≈ 5 km^2 at resolutions of 10s of meters and seconds. Sources of error can be traced to image processing, cloud shadow projection, and *kt* assignment. The analysis of forecast cloud maps versus actual images demonstrated forecast skill. Excluding completely clear or overcast days, the USI's imagery-based forecast was superior to image persistence forecast on 20 out of 22 days for 30 second forecasts, and 11 out of 22 days for 5-minute forecasts. Based on imagery alone, the optical depth (thick or thin), percentage cloud cover, and mean velocity of clouds can be approximated at sub-kilometer resolution.

This information regarding the properties of the cloud field above a solar power plant should therefore serve as a valuable input for short-term irradiance forecasting. However, the introduction of other variables (i.e. CBH data and measured irradiance or power output) which are necessary to produce a site-specific irradiance forecast causes larger errors for deterministic forecasting. Excluding clear days or days with small forecast sample size, bulk error metrics showed USI forecast performance to be the same as or better than *kt* persistence forecasts on 4 out of 24 days for 5-minute forecasts, 8 out of 23 days for 10-minute forecasts, and 11 out of 23 days for 15-min forecasts. The typical low CBHs in coastal southern California restrict the size of the cloud map and typically only allow forecasts up to horizons of about 15 min. The upwind (westerly) location of the USI with respect to the ground stations contributed to increase the forecast horizon.

Forecast errors during several periods were traced to inaccurate cloud base height (CBH). A ceilometer will be installed to provide CBH measurements within the USI forecast area. Additionally, an algorithm is currently being developed to calculate CBH by leveraging different perspectives of the same cloud field provided by multiple Sky Imagers. The deployment of more than one USI will also improve spatial coverage and maximum forecast horizon.

Another focal research area is the cloud velocity algorithm. (Huang, Yoo, Yu, Huang, & Qin, 2012) developed a hybrid cross-correlation and local feature approach which was found to offer superior performance than phase-correlation, cross-correlation, and local feature approaches alone. To address the current weakness in dealing with inhomogeneous cloud velocities, a dense motion estimation method will be applied to detect differing velocities of individual patches of clouds and segment them for individual advection. Lastly, more pyranometers will be deployed throughout the UCSD campus to increase the coverage and spatial resolution of ground sites within the USI footprint. Greater coverage would better emulate the spatial averaging at a large power plant (Lave, Kleissl, & Arias-Castro, High-frequency irradiance fluctuations and geographic smoothing, 2012) and reduce the sharp, step-like jumps in irradiance often observed in current USI forecast time series. Alternatively, models such as a wavelet variability model (Lave & Kleissl, Cloud speed impact on solar variability scaling -- application to the wavelet variability model, 2013) (Lave, Kleissl, & Stein, A wavelet-based variability model (WVM) for solar PV power plants, 2012) or a Poisson model (Arias-Castro, Kleissl, & Lave, 2014) could be applied to pyranometer and USI forecast irradiance time series in order to simulate the behavior of power output by large solar arrays.

The error values presented in this paper represent the aggregation of different error sources. A comment on forecast error metrics is in order; RMSE, MAE, and MBE metrics alone (even if normalized by average *kt*) do not provide much insight into the forecast skill. Forecasts for 30 sec intervals over kilometer-scale domains will naturally result in larger errors than, for example, hourly average forecasts from numerical weather prediction. This is because the variability is larger for 30 second averages, and some of the variability is essentially random and difficult to forecast.

A forecast skill was therefore computed in order to compare the performance of the USI against the baseline *kt* persistence forecast on the same forecast horizon and temporal resolution, but *kt* persistence forecast is difficult to surpass on clear or overcast days, as an error-free USI forecast would only produce approximately the same result. However, the forecast skill metric also has limitations as the reference (persistence forecasts) cannot predict ramp events caused by approaching cloud cover, which would be the main application of a Sky Imager. Particularly, although a ramp event may be detected by the USI, errors in magnitude and especially timing will serve to increase MAE and RMSE error metrics. With typical cumulus cloud passages over the footprint lasting only 10s of seconds, phase-shifts in the forecast of half a wavelength will be common and would actually cause negative forecast skill. Future work will include designing an appropriate ramp forecast metric, but choices for ramp magnitude and duration are arbitrary. The forecast skill metric allows intercomparing Sky Imager forecast results. However, to the best of our knowledge—with the exception of (Chow, et al., 2011) which was already discussed in detail in Section 4.1—other investigators only forecasted for the location of the Sky Imager which largely eliminates cloud base height errors. (Marquez & Coimbra, Intra-hour DNI forecasting based on cloud tracking image analysis, 2013) found forecast skills of 0.2 to 0.4 for 3 to 15 min forecast horizons for 4 days of DNI forecasts employing a TSI at Merced, CA.

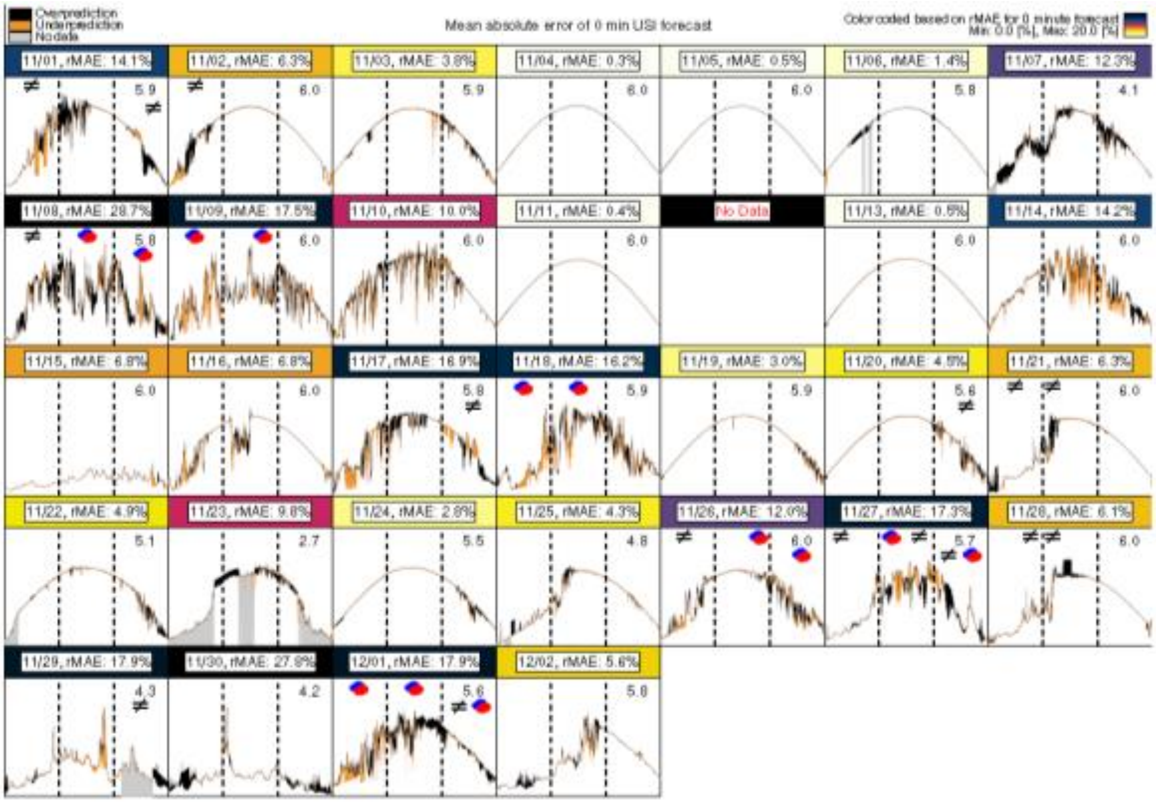

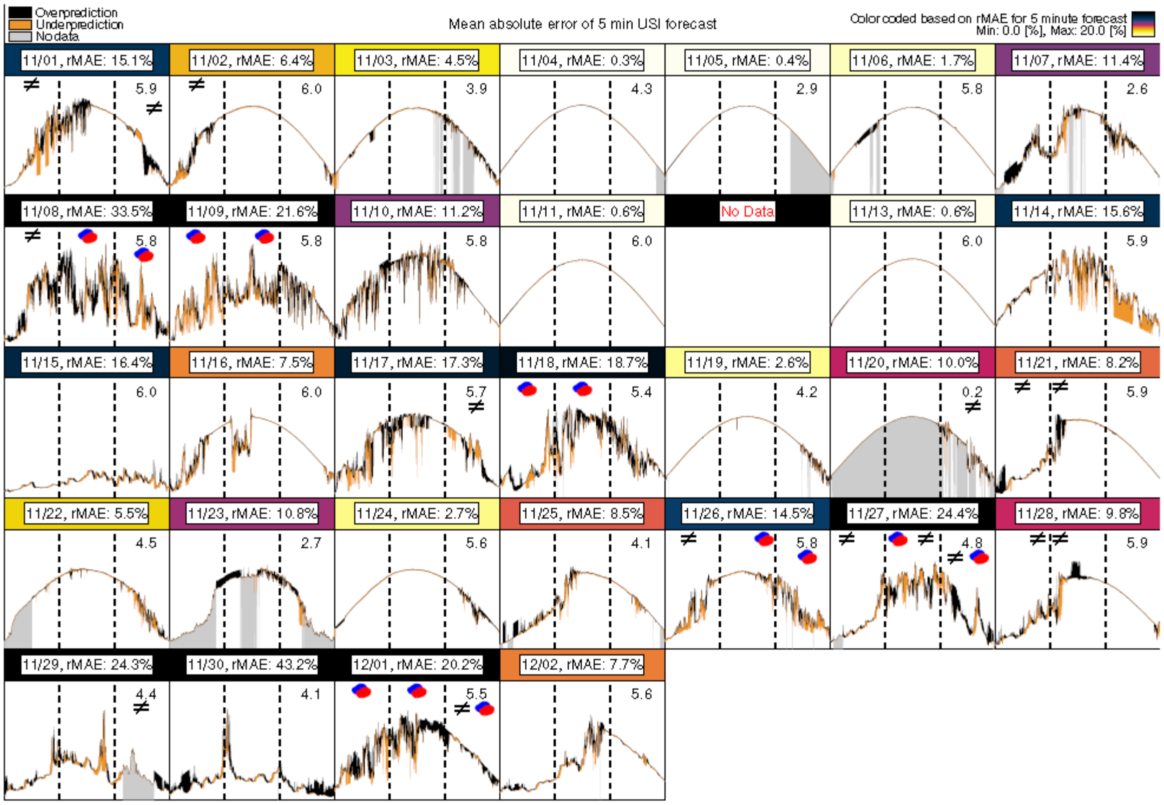

Figure 25 - Bias errors between USI nowcast GHI (top) or forecast GHI (bottom) and measured GHI averaged across all 6 ground stations. Labels are color coded based on rMAE, ranging from 0% (white) to 20% (black). Note that while plots show GHI, error metrics were computed using the clear sky index kt. Black regions represent overprediction, while orange regions represent underprediction. Times when no forecast data was available are shaded in gray. The average number of stations covered by the shadow map throughout each day is reported in the top right corner of each plot. A 6= marks periods with significant mismatch between observed clouds and METAR CBH, and a blue/red icon indicates the presence of multiple cloud layers.

5. Development and Application of a Controller for Energy Storage

In this section dispatch strategies for a battery energy storage system (Section 5.1.) coupled to a PV system are presented. The dispatch strategies range from simple off-peak/on-peak constant charging to optimization methods using load and PV output forecasts (Section 5.2). For illustration purposes results for one summer day are presented (Section 5.3). Simple economic and battery lifetime metrics are computed in Section 5.4 and a parametric analysis of net present value given battery storage size and demand charge reduction objective is presented in Section 5.5.

Table 4. Nomenclature

Nomenclature	
A	annual energy bill savings
E	energy
f	objective function
M	number of forecast update times
N	number of timesteps
NCC	number of charge cycles at 80% depth of discharge
NPV	net present value
OM	operation and maintenance costs
P	power (dE/dt)
R	power ramp rate (dP/dt)
r	discount rate
T	nominal battery lifetime
t	time.
Greek symbols	
Δ	discrete change
ε	forecast accuracy (safety) factor.
Superscript	
DC rating	DC nameplate rating of the PV array
m	forecast update index
max	maximum value
min	minimum value
n	time index
target	target value, objective
total	total energy capacity of the battery array.
Subscript	
0	initial condition ($n = 0$)
l	load
lf	load forecast
o	PV+ output
opt	computed with LP optimization routine, i.e. Eqs. 1-3
p	PV output
pf	PV output forecast
s	battery (storage)
update	time between forecast updates.
Symbols	
<>	denotes a time average.

5.1 PV-Storage (PVS) System Model

Ongoing advances in electrochemical battery technologies have dramatically increased the energy density, reliability and product lifetime of batteries. These improvements have translated to significant cost reductions in kW scale batteries, making battery energy storage an attractive option to regulate the variable power output of PV systems. If a battery is connected to the PV system behind the grid interconnect, the energy stored in the battery can be dispatched “on demand” to modulate the net output of the combined PV-storage system (hereafter PVS system) to the grid. A simplified PVS system was considered, in which a PV array and a battery are connected to the electricity grid via a lossless DC-AC inverter (see Figure 26).

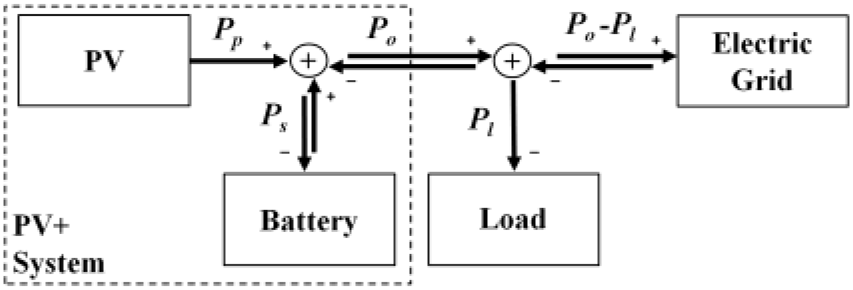

Figure 26 - A schematic of the system model illustrating the important components and power flows; the PV+ system is delineated by the dashed line. Positive and negative symbols indicate sign conventions for active power flows. Because the inverter is assumed to be lossless it is not shown in this diagram. The battery management system is included in the battery, which allows "black box" treatment of complex electrical dynamics and transients within the battery.

An idealized PV output forecast was obtained from one year of 15 min DC power output data from the EBU2 rooftop PV array on the UCSD campus. The PV array has a DC nameplate rating of 75 kW DC. A load forecast was generated from UCSD campus historical load data. Uncertainty in the load forecast was simulated by incorporating random, normally distributed fluctuations with a standard deviation of 5% of the magnitude of the peak load at any given time. To simplify the analysis weekend and holiday loads were not considered in this paper. The desired amount of customer peak load reduction (based on the load forecast) is a parameter in the model and was set to 150 kW for the results presented herein. The energy storage device was a Sanyo DCB-102 Lithium-ion type battery array consisting of 120 DCB-102 batteries. A single Sanyo DCB-102 is specified to have an energy storage capacity of 1.59 kW and a lifetime of 3000 cycles at 80% depth of discharge (DoD). The retail cost was assumed to be $1000/kWh. The battery array has a total energy storage capacity of E_s^{total} = 190 kWh and a maximum charging power P_s^{min} = 41.2 kW and discharging power P_s^{max} = 86.6 kW. Power requirements for active cooling of the battery array are not considered.

5.2 Energy Storage Controller Algorithm

5.2.1. Simple off-peak/on-peak schedule

The simplest way to operate the battery is to charge it off-peak and discharge it on-peak at a constant charging rate such that the battery undergoes one complete cycle every day. This strategy guarantees daily arbitrage revenue because of the price difference between peak and off-peak. The strategy also guarantees a demand charge reduction; however the reduction is relatively small since the battery is not discharged at the maximum rate during the demand peak. Operating the battery in the charge off-peak, discharge on-peak schedule will usually guarantee good correlation between the discharging profile and the load. Because of its simplicity, it is assumed that this simple strategy is used often in practice and therefore a useful reference case.

5.2.2. Dynamic Real-Time Dispatch

The simple off-peak / on-peak constant charging makes excessive use of the battery, often without a benefit. Unless the demand is actually larger than the demand charge target, the battery should not be discharged during peak hours. Another scenario that avoids forecasting and optimization yet is more sophisticated than simple off-peak / on-peak charging is to dynamically dispatch the battery in real-time as a function of the net load. So, if the net load is less than zero (PV is producing more power than the demand), the battery would sit idle. If net load is greater than zero, the battery would discharge at a rate equal to the net load. If over the peak-time the energy in the net load is less than the energy in the battery, this strategy will achieve its objective to eliminate the load. However, if the battery becomes completely discharged during the day, then no energy would be left to counteract any large net loads during the rest of the day. In the latter case the demand charge would be very large, even larger than for the simple charge off-peak, discharge on-peak scenario.

5.2.3. Optimization using Forecasted Demand and Solar Production

A nonlinear, mathematical programming routine with receding horizon optimization is applied to compute the optimum dispatch schedule for the energy stored in the battery. Equation 7, Equation 8 - Equation 10, and Equation 11 - Equation 13 are the objective function, system dynamics and battery performance constraints, respectively.

$$min\left\{f(P_{lf}^{n}, P_{o}^{n}) = \sum_{k=1}^{N} (P_{lf}^{k} - P_{o}^{k})\Delta t\,, while\ P_{lf}^{k} \geq 0\ and\ P_{lf}^{k} > P_{pf}^{k}\right.$$

$s.t.$

Equation 7

$$P_{pf}^{n} + P_{s}^{n} = P_{o}^{n}$$

Equation 8

$$\frac{E^{n+1} - E^{n}}{\Delta t} = P^{n}$$

Equation 9

$$\frac{P^{n+1} - P^{n}}{\Delta t} = R^{n}$$

Equation 10

$$E_{s}^{min} \leq \sum_{k=1}^{n} P_{s}^{k} + E_{0} \leq E_{s}^{max}$$

Equation 11

$$P_{s}^{min} \leq P_{s}^{n} \leq P_{s}^{max}$$

Equation 12

$$R_{s}^{min} \leq \frac{P_{s}^{n+1} - P_{s}^{n}}{\Delta t} \leq R_{s}^{max}$$

Equation 13

Variables E, P and R are energy, power and ramp rate. Variables with subscript s are related to the battery array, subscript pf refers to the PV power output forecast, subscript lf is the load forecast, subscript o denotes power flows to and from the grid and 0 indicates an initial condition. Superscript n is the current timestep and N denotes the maximum number of timesteps over the forecast horizon (i.e. N=96 for a 24 h forecast horizon at 15 min sampling rate). Superscripts min and max indicate performance limits of the battery.

5.3 Methods for Idealized Case Study and PV+ system cost-benefit analysis

There are three PV+ system parameters in our model: PV array DC nameplate rating ($P_p^{DC\ rating}$), energy storage capacity (E_s^{total}) and the peak load reduction target (P_l^{target}). P_l^{target} was chosen as a PV+ system parameter because the optimization algorithm targets demand charge management, and P_l^{target} is linearly proportional to the customer's demand charge (see Appendix A). A more common choice to quantify the load capacity being managed by the PV+ system is battery capacity ratio, which is the quotient of the total energy storage capacity and the average daily load energy capacity ($E_s^{total}/\langle E_l \rangle$; [11]). It will be shown later (Figure 32a) that P_l^{target} and $E_s^{total}/\langle E_l \rangle$ are consistent and both are valid PV+ system parameters. To evaluate feasible PV+ system designs a cost analysis was performed to determine the NPV of the battery storage system by calculating energy bill savings attained over the lifetime of the battery relative to capital costs of the storage system, annual operation and maintenance (O&M) costs and the discount rate. The net present value is estimated from

$$NPV = \sum_{t=0}^{T} \frac{A - OM}{(1 + r)^t}, \qquad \textbf{Equation 14}$$

where A is the value of annual energy bill savings extrapolated from 2009 data, OM is the annual O&M cost for operating the storage system (including energy costs for active cooling of the battery array), r is the discount rate, t is the current year and T is the total lifetime of the battery in years. For $t = 0$, OM is equal to the capital costs incurred on the purchase and installation of the storage array and $A = 0$. In this study we assumed that annual O&M costs were constant and equal to 3% of the capital cost of storage. Annual energy bill savings are attributed solely to the use of energy storage in the PV+ system, and energy bill savings are assessed in terms of the difference between the annual energy costs with and without the application of battery energy storage. Electric utilities assess time of use (TOU) energy pricing and demand charges for industrial customers. The energy bill was calculated using the San Diego Gas & Electric (SDGE) AL-TOU rate schedule for industrial customers. The AL-TOU tariff includes basic service fees, on-peak and non-coincident demand charges and TOU energy pricing (Table 5; [16]). Non-coincident demand charges are assessed monthly based on the utility customer's maximum load (15 min interval) during the current month, not considering the rate periods. If the maximum load during the previous 11 months was greater than the maximum load in the current month, the non-coincident demand charge is computed from 50% of the maximum load during the previous 11 months. This rate structure incentivizes customers to gradually reduce their monthly peak load in order minimize the non-coincident demand charge portion of their energy bill.

Table 5. San Diego Gas and Electric (SDGE) seasonal time-of-use rate periods for industrial customers (Schedule AL-TOU).

	Summer, May 1 - Sep 30	**Winter, Oct 1 - Apr 30**
On-peak	11:00 - 18:00, Weekdays	17:00 - 20:00, Weekdays
Semi-peak	6:00 - 11:00, Weekdays	6:00 - 17:00, Weekdays
	18:00 - 22:00, Weekdays	20:00 - 22:00, Weekdays
Off-peak	22:00 - 6:00, Weekdays Plus Weekends & Holidays	22:00 - 6:00, Weekdays Plus Weekends & Holidays

In order to quantify the financial advantages of our optimization strategy we compared the optimized dispatch schedule (OPT) with two storage dispatch schedules that did not use any PV output or load forecast information, a simple off-peak/on-peak, charge/discharge schedule (OFFON) and a real-time dispatch scenario (RT). For the OFFON schedule the battery undergoes one full charge cycle at 80% depth of discharge (DoD) per day. Charging and discharging rates are constant over the off-peak and on-peak periods defined in Table 5;. OFFON is often used in real applications because it is simple, guarantees reduction in net load during the on-peak rate period, and maximizes off-peak, on-peak energy arbitrage. For the RT schedule the battery is charged to full capacity during the off-peak rate period and discharged to meet the customer's actual net-load in real-time. RT is also simple and attractive because the battery is only used when it is needed for peak load reduction thus increasing battery lifetime.

5.3.1 Battery System

The energy storage device is a Sanyo DCB-102 Lithium-ion battery array (Sanyo was purchased by Panasonic during the course of this research). A single Sanyo DCB-102 has nominal energy storage capacity of 1.59 kWh and minimum lifetime rating of 3000 cycles at 80% DoD. The DCB-102 has a maximum charging power of P_s^{min} = -340 W and a maximum discharging power of P_s^{max} = 720 W. The capital cost of the battery array was assumed to be \$1000/kWh including installation costs. The number of charge cycles at 80% DoD over a period of N timesteps was calculated from Equation 15

$$NCC = \frac{1}{2}\sum_{n=1}^{N}\left|\frac{E_s^n - E_s^{n-1}}{0.8E_s^{total}}\right|, \qquad \textbf{Equation 15}$$

where NCC is the number of charge cycles and E_s^{total} is the total energy capacity of the battery array. To avoid overcharging or overdrawing of the battery array the model parameters E_s^{min} and E_s^{max} are set to $0.2E_s^{total}$ and $0.99E_s^{total}$, respectively.

5.3.2 Solar and Load Data and Forecasts

One year (2009) of 15 min DC power output data from one inverter of the EBU2 building rooftop PV array on the University of California, San Diego campus was used as the basis for P_p and P_{pf} (**Figure 27**a). The PV array has a DC nameplate rating of 7.5 kW DC and the data was scaled to approximate the output of a larger system with a rating of $P_p^{DC\ rating}$ = 500 kW DC; for 15 min averages the relative variability of the output for a 500 kW or 7.5 kW are essentially identical [17]. The load data were obtained from 2009 UCSD campus load profiles (Figure 27b).

Real forecasts (e.g. from numerical weather prediction) often produce large errors that are weather and location dependent [18].To make our results more generalizable and focus on the performance of battery dispatch strategies, a PV "forecast" was generated from the measured data. The 15 min PV output was filtered using a 45 min moving average window to generate the solar forecast P_{pf}. During clear and overcast conditions P_p (the actual PV power output) and P_{pf} (the forecast PV output) are very close since P_p is smooth, but in partly cloudy conditions P_p fluctuates randomly about $<P_{pf}>$. Uncertainty in the load forecast was simulated by incorporating random, normally distributed fluctuations with a standard deviation of 5% of the magnitude of the load in Figure 27b.

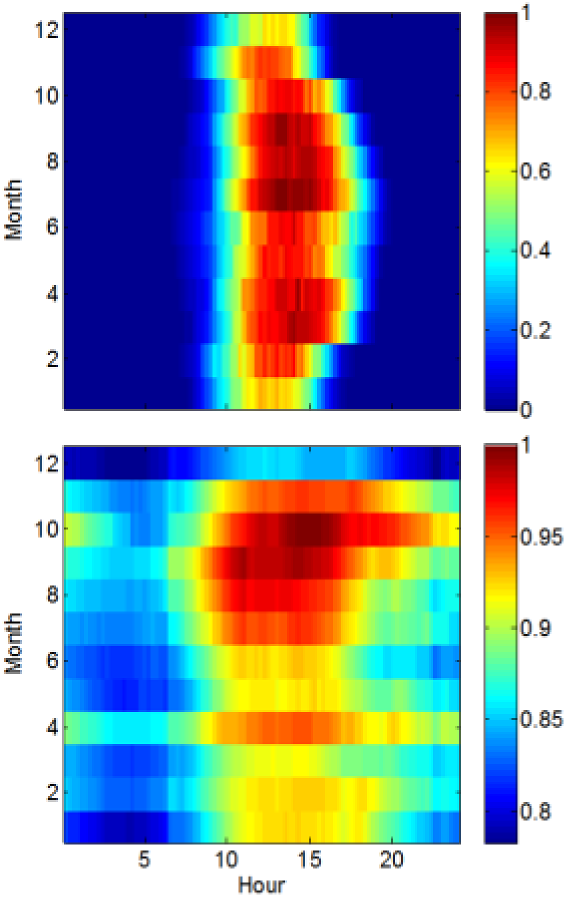

Figure 27– Monthly climatologies (15 min resolution) of a) the measured PV array DC output normalized by the DC nameplate rating; b) the total measured load normalized by maximum annual demand (33.8 MW in October). The peak load profile is obtained by requiring that the maximum monthly peak load is $\{P_l^{max}\}_{monthly} - P_l^{target}$ and the excess "peak load" is the input to the optimization routine. Note that the peak in the PV array output usually occurs several hours earlier than the peak in the customer load.

5.4. Results for Idealized Case Study

PV+ system performance was simulated for a wide range of peak load reduction targets (P_l^{target} = 240-1500 kW), battery storage capacities (E_s^{total} = 240-1270 kWh) and a PV array with a fixed nameplate rating of $P_p^{DC\ rating}$ = 500 kW DC in order to evaluate model performance and quantify the financial benefits that are realized when PV and load forecasts are applied to optimize the charge/discharge schedule of the battery. In total 602 cases were simulated for one year.

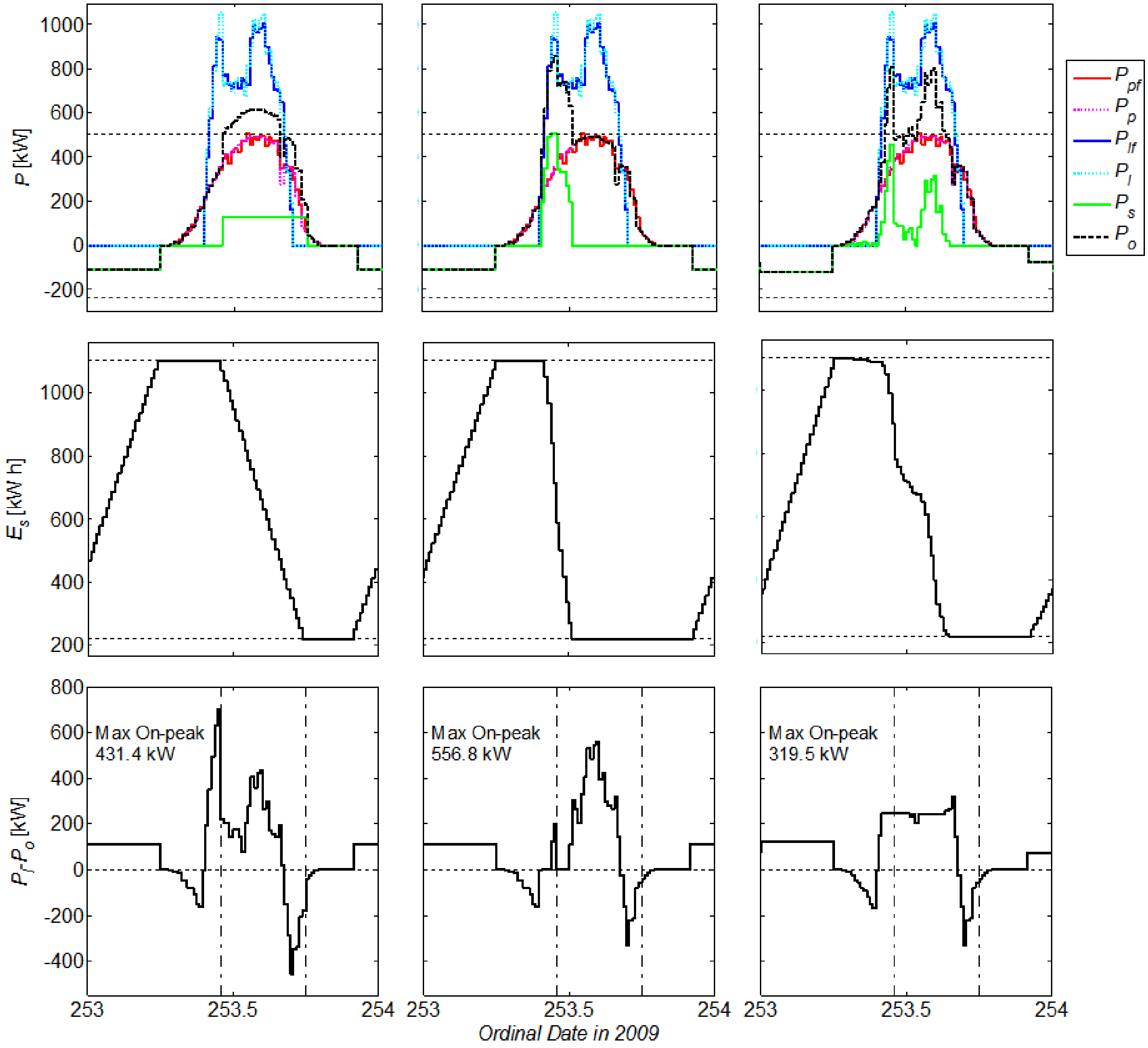

Figure 28– Sample timeseries of model output data on September 9th, 2009 illustrating PV+ system power flows (a,b,c), the battery charge state (d,e,f) and the net load on the electric grid (g,h,i). Figs. a,d,g show model output when energy storage is dispatched according to the OFFON strategy, Figs. b,e,h show model output for the RT strategy and Figs. c,f,i show model output for the OPT strategy. Power flows in Figs. a,b,c are relative to the PV+ system so that $P_o > 0$ indicates net generation by the PV+ system and $P_o < 0$ indicates reverse power flow (i.e. the battery is charging from the grid). The fine dashed horizontal lines in Figs. a,b,c, indicate the maximum charging and discharging power of the battery array. The net load plotted in Figs. g,h,i is relative to the electric grid so that $(P_l - P_o) > 0$ indicates power flow from the grid to the customer and vice versa. The dash-dotted vertical line in Figs. g,h,i indicate the range of the on-peak period as defined in Table 1. The PV+ system parameters for the data shown in this figure are $P_p^{DC\ rating}$ = 500 kW, E_s^{total} = 1111 kWh and P_l^{target} = 1020 kW.

Figure 28 shows exemplary time series of model output data from September 9th, 2009 for P_l^{target} = 1020 kW and E_s^{total} = 1111 kWh. The columns in Figure 28 show PV+ system power flows, battery charge state and net load on the electric grid for the OFFON, RT and OPT dispatch schedules. Figure 28c,f,i illustrate superior performance of the optimized schedule over the OFFON and RT dispatch schedules that do not use PV output and load forecasts. For the given PV+ system parameters the battery undergoes one complete charge cycle per day for all three dispatch schedules. Using the OFFON strategy, the energy stored in the battery is dispatched concurrently with the peak load, but the output power of the battery is too low during that time. Using the RT strategy the battery discharges too quickly leading to complete discharge by the beginning of the on-peak rate period. With the OPT strategy the shape of the battery discharge curve closely approximates the shape of the peak load, and the net load during the on-peak rate period is relatively constant when compared with the off-peak/on-peak and real-time strategies (Figure 28i).

Figure 28g,h,i show that the maximum net load on the electric grid during the on-peak rate period (i.e. when higher demand charges are assessed by the utility) is smallest under the optimized schedule. For the data shown in Figure 28 the optimization algorithm reduced the maximum on-peak, net load by 26% (112 kW) when compared with the OFFON schedule, and 43% (237 kW) when compared with the RT schedule. The small peak near the end of the on-peak rate period in Figure 28i is due to under-forecasting of the net load resulting from an overestimation of the actual PV power output by the PV forecast and/or an underestimation of the peak load by the load forecast. This leads to the battery becoming discharged just before the end of the high load period.

5.4.1. Performance evaluation of the optimized dispatch schedule

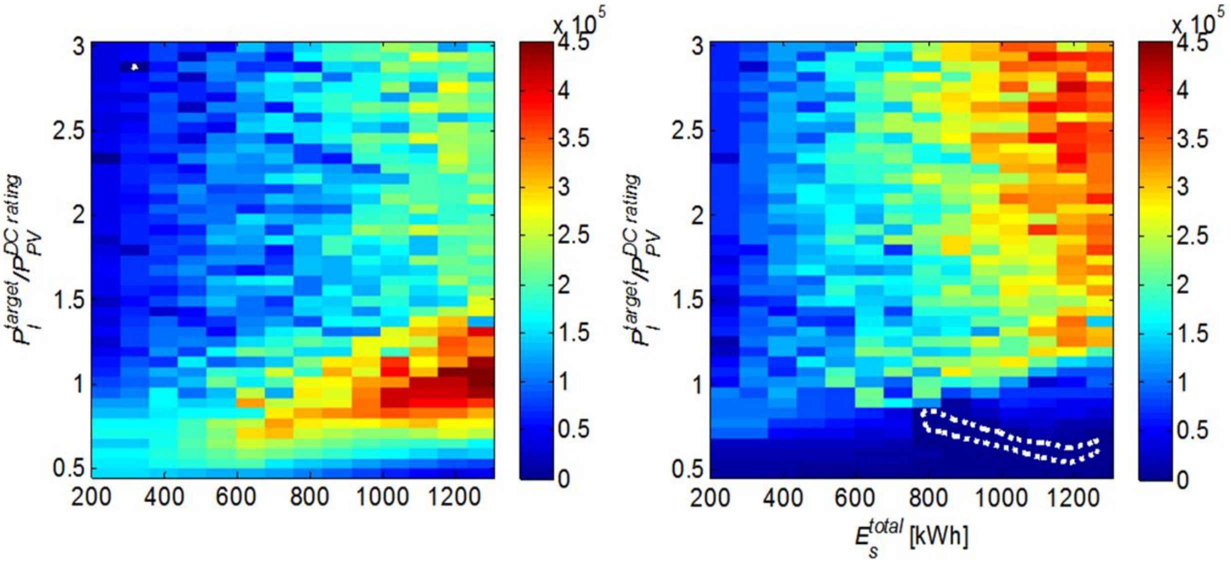

Figure 29 – Difference between the net present value (Δ*NPV*; Equation 14) of the OPT schedule and (a) the OFFON schedule; (b) the RT schedule. The NPV difference for a broad range of battery capacities (E_s^{total}) and peak load reduction targets (P_l^{target}) are shown. The PV array nameplate rating was set to $P_p^{DC\ rating}$ = 500 kW DC. The units of the color scale are $USD and the dashed white line delineates the $0 contour.

Results from 2009 model output were extrapolated over the lifetime of the battery (3000 charge cycles) to estimate the NPV of the battery array. Figure 29 shows the NPV gain of the OPT dispatch schedule over the OFFON (Figure 29a) and RT (Figure 29b) dispatch schedules for different battery capacities that were “tasked” with a broad range of peak load reduction targets (P_l^{target}). Total battery capacity (E_s^{total}) is plotted on the horizontal axis and the peak load reduction target ratio ($P_l^{target}/ P_p^{DC\ rating}$) is plotted on the vertical axis. Given that $P_p^{DC\ rating}$ is 500 kW, P_l^{target} ranges from 250 kW to 1500 kW). The color scale is the increase in NPV (ΔNPV) of the battery array in US dollars. Figure 29 shows that operating the battery on the OPT dispatch schedule is more profitable than operating on the OFFON or RT schedules for most battery sizes and peak load capacities modeled in this study. The OPT strategy provides significantly more value than the OFFON strategy, especially in the range $E_s^{total} > 500$ kWh and $P_l^{target}/ P_p^{DC\ rating} < 1.25$ where the NPV of the battery increases in the range \$150k-\$450k (or \$220/kWh of capacity) under the OPT scenario. When compared with the RT dispatch strategy, the OPT schedule increases the value of the battery array by about \$100k - \$400k (or \$270/kWh) for $E_s^{total} > 600$ kWh and $P_l^{target}/ P_p^{DC\ rating} > 1.5$ (Figure 29b). In Figure 29a the increase in NPV becomes independent of P_l^{target} for large values of $P_l^{target}/ P_p^{DC\ rating}$, because the demand charge savings are ultimately limited by the total battery capacity regardless of the dispatch schedule.

5.4.2. NPV of the battery array

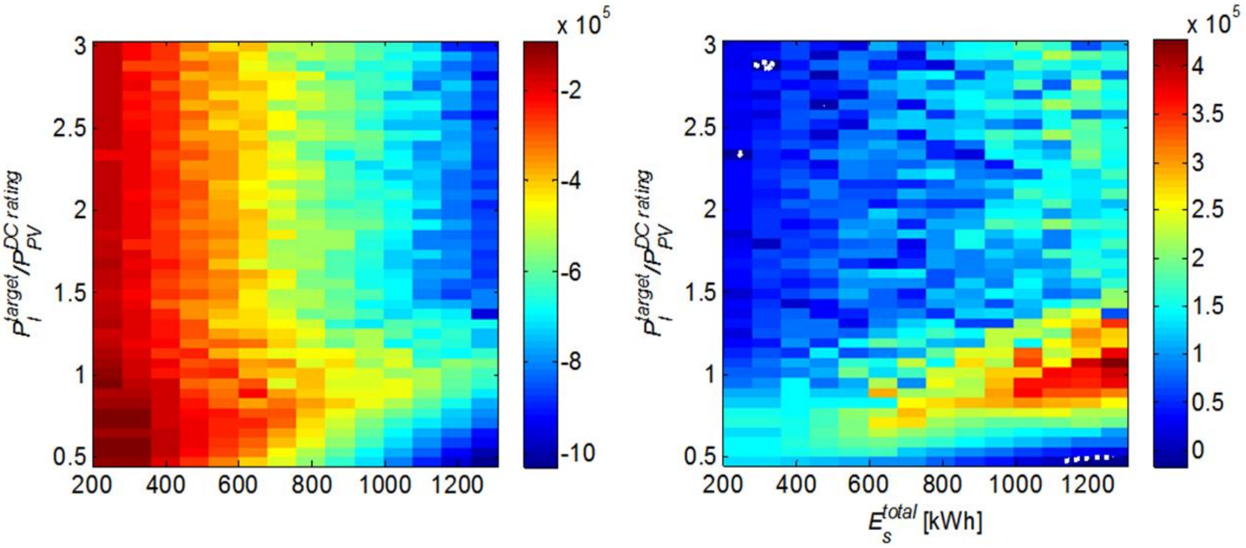

Figure 30– The NPV of the battery array operated on the optimized dispatch schedule assuming an installed cost for storage of (a) \$1000/kWh and (b) \$200/kWh. The units of the color scale are \$USD and the dashed white line delineates the \$0 contour.

Figure 30 illustrates the NPV of the battery array when operated under the optimized dispatch strategy assuming different costs for the storage. Figure 30a shows the battery NPV assuming a cost \$1000/kWh, which is representative of the 2011 market price for large scale, Lithium-ion battery arrays. At a price of \$1000/kW all battery sizes have a negative NPV indicating that

Lithium-ion type batteries are not a financially viable technology in demand side applications if energy bill savings for the utility customer are the only value proposition considered in the valuation of the storage array. The results of Figure 30a raise an interesting question: *What is the price at which Lithium-ion batteries become financially viable in demand side applications?* We estimated this price within our model framework by varying the capital costs in Equation 14. Figure 30b shows the NPV of the battery array at a cost of \$200/kWh, the maximum price at which the NPV > 0 for nearly all PV+ system designs modeled in this study. It is worth noting that the NPV of the battery array became greater than zero for a limited range of PV+ system parameters at a price as high as \$600/kWh.

Figure 31 shows the maximum NPV in USD as a function of battery energy storage capacity for three hypothetical storage costs \$600/kWh, \$400/kWh and \$200/kWh. At an installed cost of \$600/kWh only the battery capacities less than 400 kWh are profitable over the lifetime of the battery array and the marginal cost of storage is -123 \$/kWh. At installed costs of \$400/kWh and \$200/kWh all battery sizes are profitable and the marginal benefit of additional storage is 70 – 270 \$/kWh. In practice, when $E_s^{total} > E_l$ (or $P_l^{target} > sup\{P_l\}$) the slope of the lines in Figure 31 becomes zero, because no additional demand charge savings can be realized.

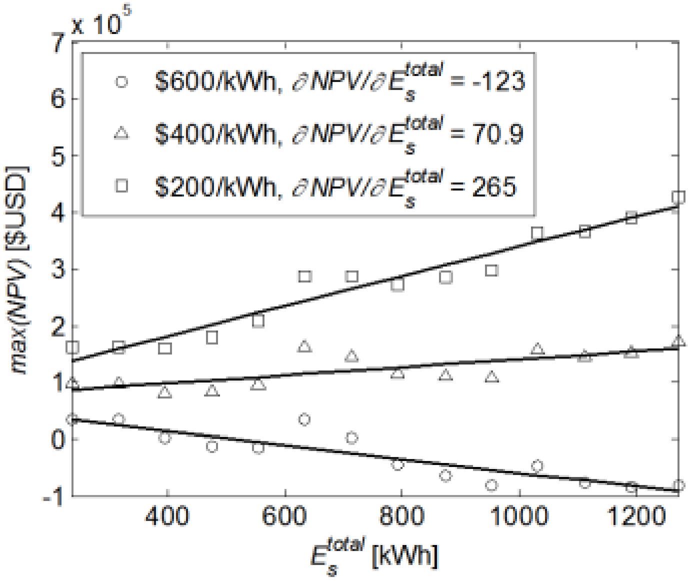

Figure 31– The maximum NPV [\$USD] as a function of battery energy storage capacity assuming an installed cost for Lithium-ion batteries of a) \$600/kWh, \$400/kWh and \$200/kWh. For example, the data plotted as squares in this figure follow the maximum of the surface in Figure 30b. The slope of the lines is the marginal cost of additional energy storage.

5.4.3. PV+ System Parameters at Maximum NPV

Figure 32a shows that the peak load reduction target ratio ($P_l^{target}/P_p^{DC\ rating}$) and battery capacity ratio ($E_s^{total}/\langle E_l \rangle$; [11]) are linearly increasing functions of battery energy storage capacity. P_l^{target} is a relevant PV+ system parameter in the context of demand charge management because it is linearly related to the reduction in demand charges, however, in practice E_s^{total}/<E_l> is a more useful quantity for system design. Figure 32b shows the financial value of the OPT dispatch schedule over the OFFON and RT dispatch schedules in terms of the difference in the NPV of the battery array (*ΔNPV*) as a function of the battery capacity ratio. *ΔNPV* in Figure 32b can also be interpreted as value of the PV power output and load forecasts. Figure 32b shows that the value of the forecasts increases linearly with E_s^{total}/<E_l> in the range \$150k - \$400k when compared to the ONOFF strategy. The trend in *ΔNPV* as a function of E_s^{total}/<E_l> is fairly weak for the OPT-RT data in Figure 32b, and is better represented by the mean value of the data (<*ΔNPV*> = \$51k) rather than a linear regression.

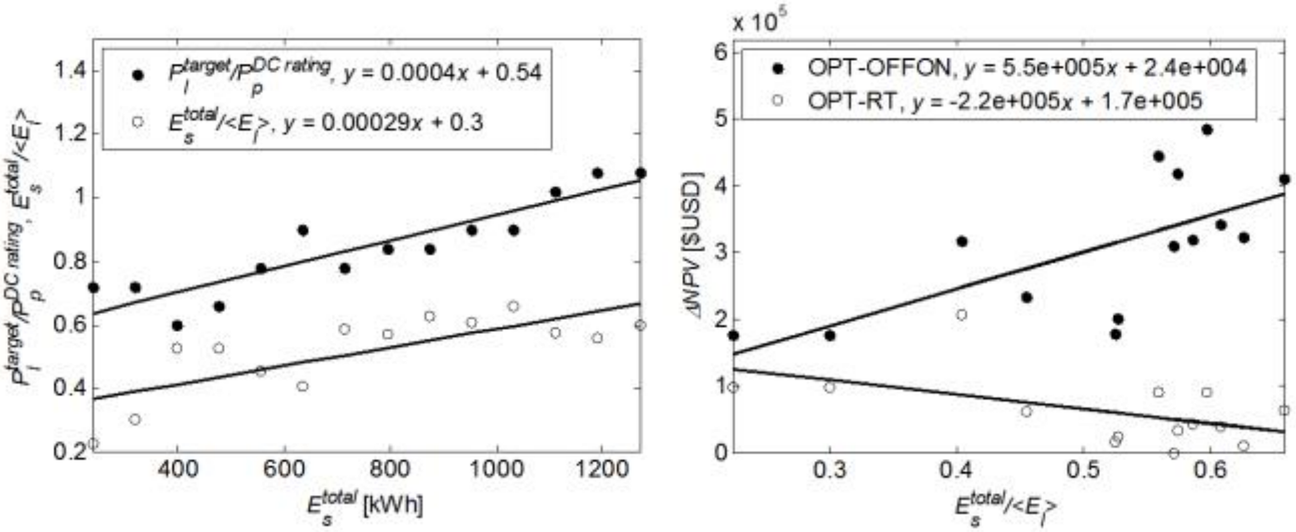

Figure 32– a) PV+ system parameters as a function of the battery energy storage capacity (E_s^{total}) and b) the value of the optimized dispatch schedule (*ΔNPV*) as a function of battery capacity ratio (E_s^{total}/<E_l>) along the maximum of the surface in Figures 30a and b. <E_l> is the average daily energy consumption during the peak period. The data in b correspond to the maximum of the surface plotted in Figure 29.

5.4.4. Discussion

An important goal of this modeling effort was to demonstrate and quantify the value of applying PV power output and load forecasts to inform energy dispatch optimization in PV+ systems. The OFFON schedule maximizes price arbitrage in the time-of-use energy market, but its success as a demand charge management strategy relies on a strong temporal correlation between customer's actual peak load and the peak load period defined by the utility (Table 5). If the customer's actual peak load occurs outside the peak load period defined in the utility rate schedule the customer may incur high non-coincident demand charges. Because the peak load is typically variable over the on-peak market period, constant output from the battery over during the on-peak period market period is a robust yet suboptimal approach for demand charge minimization (e.g. Figure 28a,d,g).

The effectiveness of the RT schedule primarily depends on whether the energy storage capacity of the battery exceeds the daily energy requirement of the customer's peak load (<E_l>). If the energy capacity of the battery is greater than the energy required to meet the customer's peak load, then energy stored in the battery can be dispatched in real-time and the entire peak load will be eliminated. If the battery capacity is less than the energy requirement of the load, the energy stored in the battery will be depleted before the peak load event (Figure 28b,e,h), and the customer incurs high demand charges. The optimization algorithm developed in this paper improves on both the OFFON and RT strategies by using PV power output and load forecasts to overcome the disadvantages of both approaches. The optimal scheduling strategy targets demand charge management, because demand charges typically account for the largest portion of a utility customer's energy bill.

Figure 29 quantifies the financial advantages of using PV power output and load forecasts to determine the optimal stored energy dispatch schedule in the PV+ system. We chose to present results as absolute USD values rather than percent values because, for an NPV that can be positive or negative, absolute USD values provide readers with a more tangible quantity to interpret the relative value of different dispatch strategies. Figure 29a shows that the largest financial gains from OPT strategy over the OFFON strategy occurred in the range in the range $E_s^{total} > 500$ kWh and $P_l^{target} / P_p^{DC\ rating} < 1.25$. Those gains were attributed to superior load following and reduced battery cycling characteristics of the optimized dispatch schedule. In the range $P_l^{target} / P_p^{DC\ rating} < 1.25$, the battery array lasts 8.2 year under the OFFON schedule compared to an approximately 10 – 16 year lifetime under the OPT schedule. The OPT dispatch schedule significantly increases the value of the battery array over the RT schedule for $E_s^{total} > 600$ kWh and $P_l^{target} / P_p^{DC\ rating} > 1.5$. These gains occur because the optimization strategy uses forecast information to distribute the energy stored in the battery over the duration of the peak load period, even when the energy capacity of the peak load exceeds the energy capacity of the battery array (Figure 28 h,i). In the range $P_l^{target} / P_p^{DC\ rating} < 1$ the performance of the OPT and RT dispatch strategies is similar because the energy capacity of the battery is greater than the energy capacity of the peak load so the amount of energy storage is sufficient to eliminate the peak load throughout the year, thus the dispatch schedules for both strategies are similar.

Noise in Figure 29Figure 30 is due to errors in the simulated PV power output and load forecasts relative to the actual PV output and load. Because forecasts are simulated using a Monte Carlo technique, and a real-time dispatch strategy is used to respond to forecast errors between forecast updates some random variability is expected across the range of simulations modeled in this study. The implication of the PV+ system real-time response to forecast errors is that, for erroneous forecasts that significantly and consistently under estimate the forecast net load (P_l-P_o), the OPT strategy reduces to the RT strategy as the forecast error becomes large. The small peak in Figure 28i was found to be a common feature of the daily storage dispatch schedules produced by the optimization routine that occurred when the actual net load was underestimated by the forecasts. This finding is interesting because it suggests that there is an incentive to overestimate the magnitude of the net load in the forecast to improve performance of the battery. An alternative interpretation is that the financially optimal battery capacity will change based on the nature of errors contained in the PV output and load forecasts.

Generally the OPT schedule provides as much or greater value than the both the OFFON and RT schedules (in terms of the NPV of the battery array), but the optimization algorithm is only superior if reliable, accurate solar and load forecasts are available. Due to the structure of the demand charge tariffs, poor forecasts on only one day of the month could render the demand charge reduction of the OPT strategy inferior to OFFON. When no forecasts (or unreliable forecasts) are available, the PV+ operator must choose between the OFFON or RT schedule. Our results are significant in that context because, a typical PV+ owner/operator needs to purchase forecasts from a third party provider. The decision to purchase forecasts will depend on the priority of the PV+ system owner/operator and trends observed in a plot similar to Figure 29 and Figure 32b. Figure 29 illustrates that the most financially attractive energy dispatch strategy for the PV+ system is a complex decision that depends on PV+ design parameters, electrical and performance characteristics of the battery array and utility energy prices.

Although the results of Figure 29 and Figure 32b are encouraging for the economics of solar and load forecasting in demand side energy storage applications, Figure 30a indicates that at current (2011) market prices, no dispatch strategy performs well enough to make large scale Lithium-ion battery energy storage a financially viable option if monthly energy bill savings are the only benefit associated with the operation of the energy storage. We employed our model to estimate the price at which Lithium-ion energy storage would become financially viable for the demand charge management application studied in this paper. Assuming a utility rate schedule similar to the SDGE AL-TOU battery array owners can expect to break even over the lifetime of the battery at an installed cost of $600/kWh for systems with batteries smaller than 400 kWh (Figure 31). Larger capacity batteries (up to 1.25 MW) generate profits in the range $100k-200k (or $100-400 per kWh) at an installed cost of approximately $500-$400 per kWh (Figure 31). This result is particularly relevant for the 2nd life battery industry, which holds promise for developing large scale Lithium-ion battery energy storage systems from used EV batteries at a lower cost than new batteries. Perhaps the most interesting trend in Figure 30 is that the PV+ system parameters which result in the most profitable design (in terms of the NPV of the battery array) change significantly depending on the market price of the battery. At the 2011 price of $1000/kWh all battery sizes return negative profits over the battery lifetime so it is logical that the most profitable battery size is the smallest size (Figure 30a). If the market price for Lithium-ion batteries decreases sufficiently (Figure 30b) nearly all battery capacities become profitable. In the price range of $200-$400 per kWh there is a marginal benefit associated with increasing storage capacity (until demand charges are eliminated) so that large capacity battery sizes have greater NPV than small capacity batteries, which is a desirable property in the sense of economies of scale (Figure 31).

The similarity of the trends observed between the two variables plotted in Figure 32a suggests that there is a strong correlation between the P_l^{target} and $\langle E_l \rangle$. This observation is an indication that both $P_l^{target}/P_p^{DC\ rating}$ and $E_s^{total}/\langle E_l \rangle$ are consistent and robust PV+ system parameters. The value of PV power output and load forecasts in demand side, energy bill management applications for large scale, Lithium-ion batteries is $51,000 ± $35,000 over the lifetime of the battery array, where the error is represented by one standard deviation of the OPT-RT data in Figure 32b.

It is important for readers to realize that the results presented in this paper were based on site specific PV power output data and load profiles, and the SDGE AL-TOU rate schedule (SDGE, 2011). Some variability in Figure 29 and Figure 30 is expected on site to site basis. It has been noted that demand charges are typically higher in the state of California when compared to other regions in the United States (T. Pietsch, Personal communication, 2011). It is highly probable that a different rate schedule would produce different trends than those illustrated in Figure 29 and Figure 30. However, all of these differences are not related to any of the fundamental aspects of our model.

5.5. Field Testing and Validation of Demand Charge Management Algorithm

We considered a PV+ system consisting of a virtual 64 kW-rated PV array and a real 40 kWh lithium-ion battery array with a 32 kWh maximum discharge capacity (i.e., 80% DoD) connected to the utility electric grid. The PV array power output was taken from the 28.7 kW_{DC}- and 24 kW_{AC}-rated solar array at UCSD's East Campus Utility Plant (EC, 32.8803 Lat, -117.2218 Lon). The array consists of Kyocera panels installed at 20° tilt and 180° azimuth connected to SMA SB5000 and SB7000 inverters. The battery array specifications were based on the second-life electric vehicle battery array installed at the Hopkins Parking Structure (HPS) at UCSD. The array has a 40 kWh capacity, a ±60 kW maximum discharge/charge rate, and an aggregate one-way efficiency of 93% (AC to stored energy). The maximum and minimum storage charges are set to 100 and 20% of total capacity (the latter to avoid damaging deep cycles), giving a maximum DoD of 80%.

Real load and PV data were considered. 1 sec PV data from the EC solar array were averaged to 1 min. Measured PV output was scaled to a nameplate rating of 64 kW to simulate the output of a system that is more appropriately sized to meet the daytime peak load. A meter of an office building adjacent to HPS was selected as the load which exhibits the expected diurnal behavior. The histogram of the metered load is bimodal, with one mode corresponding to the typical load during weekday working hours (typically 0700 to 1800 hours) and the second to the base load of the building during "off-peak" hours. The behavior of net load (i.e., load minus PV) is markedly different from that of the load. Once accounted for, PV reduces the magnitude of the elevated daytime load, giving the net load histogram negative skewness. The histogram of the net load is unimodal and the magnitude of the residual net load spikes to be plateaued by the battery lay to the right of the single mode.

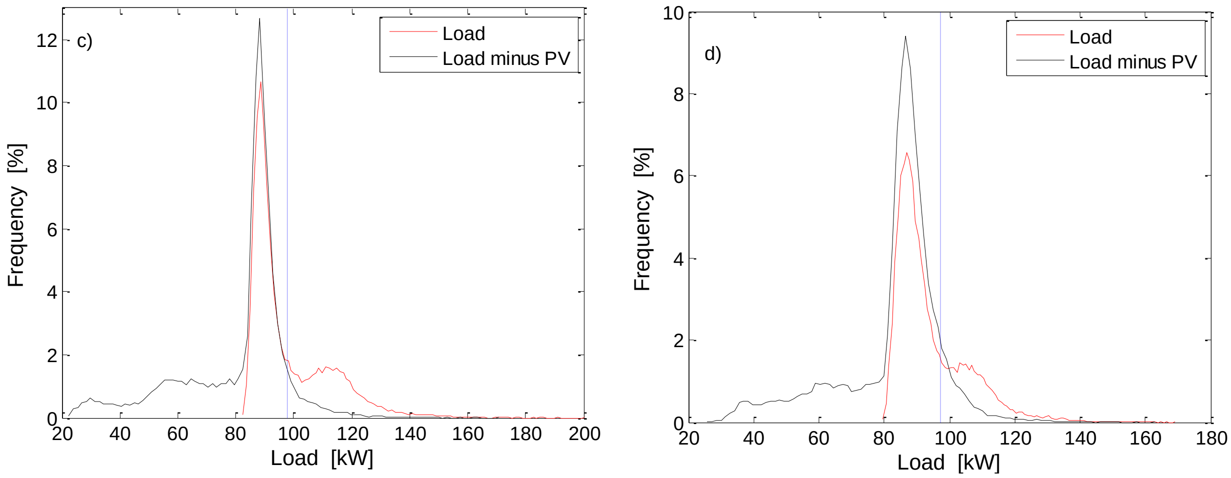

Figure 33c, d) Histogram of load (red) and load minus PV (black) for the month of July (c) and November (d). The daily mean post-DCM peak demand is denoted with a dotted vertical line.

Daily minimization of non-coincident peak demand was sought to evaluate the robustness and peak reduction capability of the dispatch algorithm. The goal of non-coincident DCM is to shave the peak load, and relatively little energy is necessary to eliminate the loads constituting the low frequency mode (greater than approximately 100 kW for both months (Fig. 4c,d). Indeed, the average post-DCM peak demand on weekdays was 97.6 kW in July and 97.4 kW in November (dotted vertical lines in Fig. 4c,d). On average, 184 kWh per weekday in July and 115 kWh per weekday in November were larger than the respective average post-DCM peak demand on weekdays, which is much less than the combined PV generation and battery capacity on most days.

The LP routine is run every hour beginning at midnight. The inputs to the midnight LP routine are the day-ahead load and PV forecasts, the charge state of the battery at midnight, and the physical constraints of the PV+ system. Subsequent LPs run each hour for the same midnight-to-midnight time span replace forecasted data with measured data. The output is a day-ahead, potentially multi-charge cycle dispatch schedule for the battery that minimizes non-coincident metered load. At midnight, the dispatch schedule is used to set the initial peak demand threshold, called the “target” or “load target”. The target is the minimum level to which the forecasted load can be reduced for the day, given the charge state of the battery and the load and PV forecasts. Given perfect load and PV forecasts, the algorithm guarantees this optimal level of reduction; however, load and PV forecasts are inherently erroneous due to variability in weather [8] and anthropogenic influence on the metered load.

Table 2 summarizes peak demand reduction against the baseline (i.e., against no DCM mechanism) for weekdays in the simulation period; weekends are ignored because they do not contain an elevated daytime load. Results are compared to a RT dispatch scheme, in which net load exceeding a load target is shaved. The load target, which is set each day and, if the battery does not fail, is constant during the day, is established using 14 day persistence, where weekdays and weekends/holidays are considered separately; that is, for a given weekday, the load target is set by: (i) generating a mean net load (load minus PV) profile using weekdays during the previous 14 days, and (ii) using the mean net load profile to calculate the maximum demand reduction (i.e., minimum load target) possible. If running RT independently, factors of safety would be used when setting the load target to prevent battery failure to a chosen probability level; to facilitate comparison with the OPT scheme, factors of safety are added such that the number of battery failures during each month are equal to that observed when running the OPT scheme. This method of comparison produces a "best case" RT scheme (i.e., the RT scheme with the best possible demand reduction statistics) for a permitted number of battery failures.

Table 3 summarizes peak demand reduction against the baseline (i.e., against no DCM mechanism) for weekdays in the simulation period for variations of the OPT scheme in which error in the PV forecast at each timestep t has been reduced as in $Pf_{\alpha}(t) = Pf(t) \pm \alpha^{*}[Pf(t) - P(t)]$, where Pf_{α} is the forecast improved by the factor α, $Pf(t)$ is the forecasted power, and $P(t)$ is the measured power; plus/minus is chosen depending on whether PV is over- or under-forecasted. Factors of 0.25, 0.50, and 0.75 were used for α. The NAM forecast chosen for this paper is freely and continuously available, but has been demonstrated to perform poorly; in particular, it consistently struggles to predict the formation and dissipation of the marine stratus layer present over Southern California during May to September, a primary cause of battery failures in the July simulation. Many superior forecast products already exist and forecast accuracy is expected to improve even more over the next few years due to market demand. Because inaccurate forecasts (over-forecasted PV in particular) repress peak demand reduction, it is prudent and justified to simulate DCM for PV forecasts with improved accuracy.

Table 4 summarizes battery discharge statistics for all variations of the OPT scheme.

Table 6 Summary of weekday peak demand reduction

	July 2012			November 2012		
Measure	PV only (%)	PV+ [a] (%)	RT [a] (%)	PV only (%)	PV+ [a] (%)	RT [a] (%)
Average	19.6	25.6	25.0	11.1	20.5	20.2
Standard deviation	4.6	5.9	5.5	4.2	3.9	3.4
Maximum	26.5	32.6	29.9	18.3	27.4	25.1
Minimum	9.6	10.7 [b]	7.9	5.7	13.6	13.2

[a] Percent reduction by both the PV array and battery array.

[b] The battery failed on the day for which the minimum reduction in peak demand by the PV+ system was observed. The minimum reduction in peak demand by the PV+ system for days during which the battery did not fail was 21.8%. Thus it is clear that battery failure causes a significant decrease in peak reduction potential.

Table 7 Summary of weekday peak demand reduction by PV+ with PV forecast improvement

	July 2012			November 2012		
Measure	25% [a] (%)	50% [a] (%)	75% [a] (%)	25% [a] (%)	50% [a] (%)	75% [a] (%)
Average	25.7	25.6	25.7	20.3	19.7	19.9
Standard deviation	4.6	5.9	5.1	4.1	4.6	4.7
Maximum	26.5	33.3	32.4	27.9	28.0	28.1
Minimum	9.6	10.7	11.7	12.5	11.3	9.7

Table 8: Battery discharge statistics for all simulations

		July 2012					November 2012				
Measure	Unit	0%	25%	50%	75%	RT	0%	25%	50%	75%	RT
DoD, mean	%	49.5	51.3	47.9	35.2	26.1	38.7	39.4	37.4	35.0	33.4
DoD, standard deviation	%	21.7	19.0	19.6	15.4	29.8	21.2	20.1	19.9	18.9	26.6
NCC, mean	--	1.27	1.28	1.27	1.13	0.84	1.07	1.08	1.04	0.99	1.00
NCC, standard deviation	--	0.32	0.30	0.32	0.32	0.45	0.35	0.34	0.35	0.30	0.67
Change in number of battery failures [a]	--	--	+1	0	-3	0	--	+1	+1	+1	0

[a] Comparison of the net change in the number of battery failures between the simulation and the real OPT scheme with no PV forecast improvement. The battery failed three times in July and zero times in November when running the real OPT scheme. For example, four failures were observed in the July simulation with 25% PV forecast improvement.

5.6. Field Testing of the BMW Mini-E Lithium Battery Pack

The BMW second life electric vehicle battery was installed and commissioned in December 2013. There are a total of four modes that the BMW system can operate in. They are DC current, DC power, AC power, and frequency response. Figure 34 is a diagram representing the system architecture and provides a communication map of the interaction between system components during testing operation. The test plan includes basic system functionality testing, such as discharging and charging at a variety of C-rates in both current and power modes. Reference performance tests (RPTs) measure initial battery state of health and degradation over time. The reference performance tests include pack-level and system-level C/6 constant

DC current performance tests and a system-level only pulse characterization test. Also included in the test plan are the EV charge control and solar PV firming algorithms. During the course of each algorithm, regular periodic RPTs are conducted to measure battery degradation under these grid applications. The RPTs are essential in evaluating battery performance and stationary battery energy storage usability to mitigate peak loads from EV charging and make PV generation more predictable.

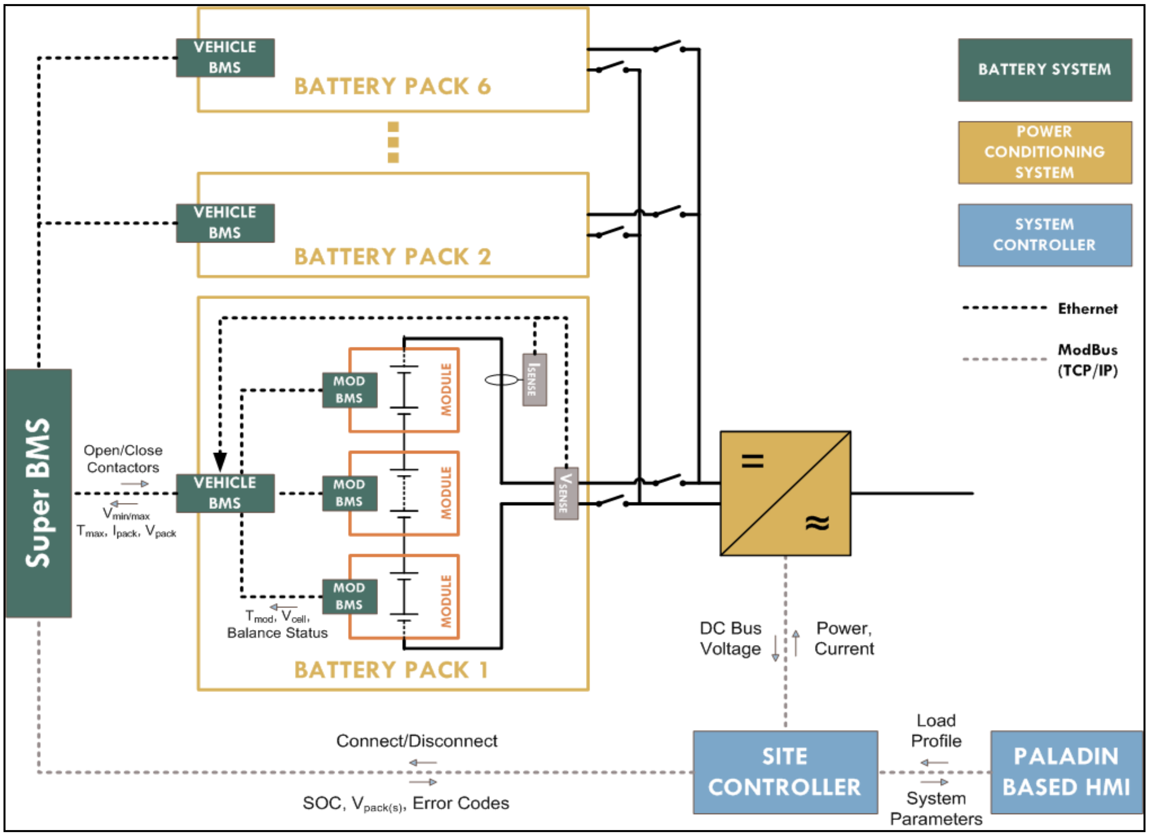

Figure 34: BMW System Architecture and Communications Map. Source: BMW and Electricore

5.6.1. Laboratory Testing of BMW Mini E Lithium Ion Battery Pack

Initial laboratory testing to evaluate the performance of a Mini E Lithium Ion battery pack was conducted by AeroVironment at their Battery Test Lab located in Monrovia, CA. The battery pack was sourced from BMW in Oxnard, CA, with engineering support from AC Propulsion and EV Grid, manufacturer and designers of the Mini E battery pack. The battery pack was directly removed from a BMW Mini E vehicle with approximately 25,000 road miles.

The purpose of the testing was to assess the battery pack’s performance and suitability for potential use in second-life applications and stationary energy storage.

Two tests were performed on the Mini E Lithium Ion battery pack to characterize its state of health and performance: a constant current performance test and a pulse power test were conducted to measure the battery pack's capacity and DC impedance, respectively.

The battery pack was also tested under a real-world stationary energy application test cycle, specifically, a real-time market (RTM) 2-day power profile to study the battery pack's potential capability in participating in CAISO markets. The real-time power profile was developed by consulting firm, KnGrid. The real-time market (RTM) power profiles for Day 1 and Day 2 are shown in Figure 35a,b.

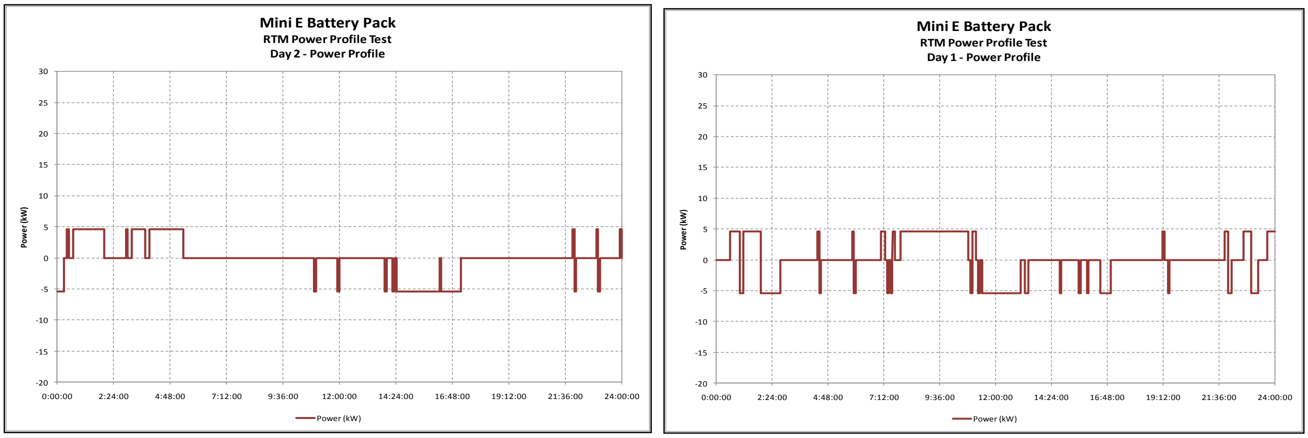

Figure 35a, b: RTM power profile for Days 1 and 2. Source: AeroVironment

Testing Results: Constant Current Performance Test

Results of the constant current performance test indicate that the Mini E Lithium Ion battery pack was at about 75% of its nominal nameplate capacity at the end of its automotive life (25,000 Southern California road miles). The nameplate capacity is measured between a max cell voltage of 4.2 V and a minimum cell voltage of 3.0 V. For this test, the capacity of the pack was measured from 4.0 to 3.3 V – per the OEM request. In this voltage range only about 80 percent of the pack energy is available. As a result, the estimated capacity loss due to the use of the pack in automotive applications was measured at just 5 percent.

Table 9a Constant current performance test summary. Source: Aerovironment

103.35 Ah Nameplate	**C/5**
C-rate used (A)	100
Discharge Rate (A)	20

Measured Capacity (Ah)	77.2
Energy (kWh)	26.7

Recharge Energy (kWh) Chg 1[2]	1.194
Recharge Energy (kWh) Chg 2[1]	26.606
Total Recharge Energy (kWh)	27.8
Energy Efficiency	96.0%

	Max	Min
BOD Temp °F (°C)	72.86 (22.7)	69.08 (20.6)
EOD Temp °F (°C)	87.62 (30.9)	81.68 (27.6)
BOC Temp °F (°C)[1]	71.6 (22.0)	68.36 (20.2)
EOC Temp °F (°C)	90.5 (32.5)	86.76 (28.2)

Data presented in Figure 36-39 show the pack voltage, current and temperature as a function of discharge (recharge) time. Also minimum and max cell voltages are presented. The spikes in the graph are due to noisy measurements reported by the battery management system.

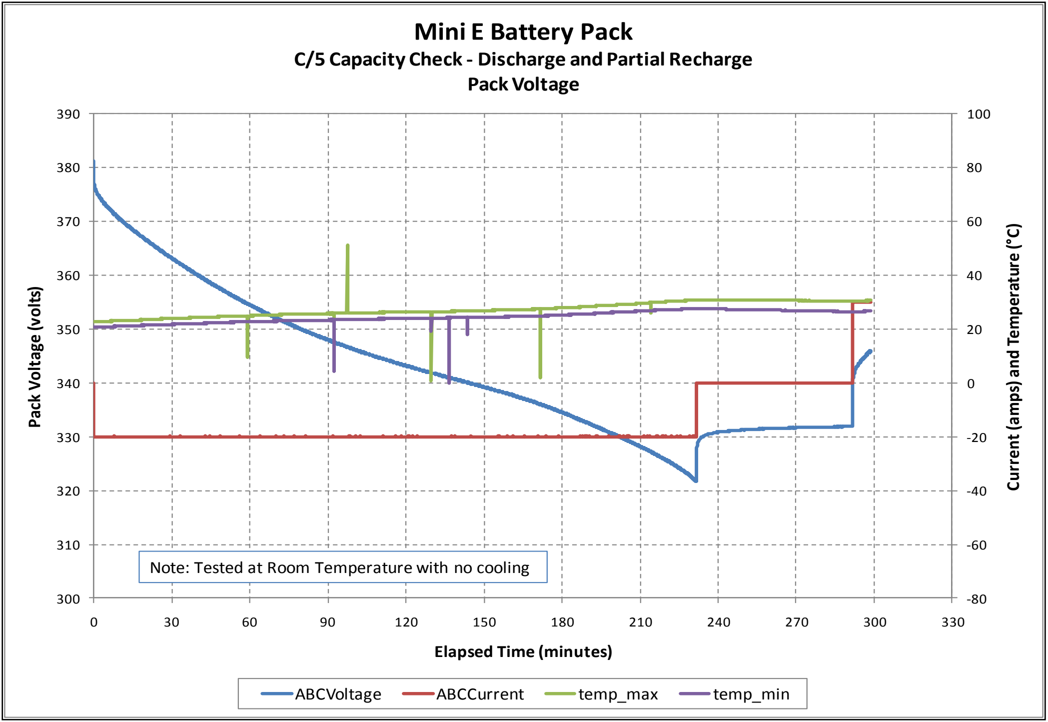

Figure 36: Pack voltage during the discharge and partial recharge portion of the C/5 capacity check

---

[2] Due to an AeroViroment requirement that this pack was not to be tested unattended, the recharge was stopped on a Friday afternoon and resumed after a weekend break. Therefore, there was a 2.5-day rest period (weekend) during the recharge step of the C/5 test. The BOC Temperature reading was taking after the 2.5 day rest period before the second recharge.

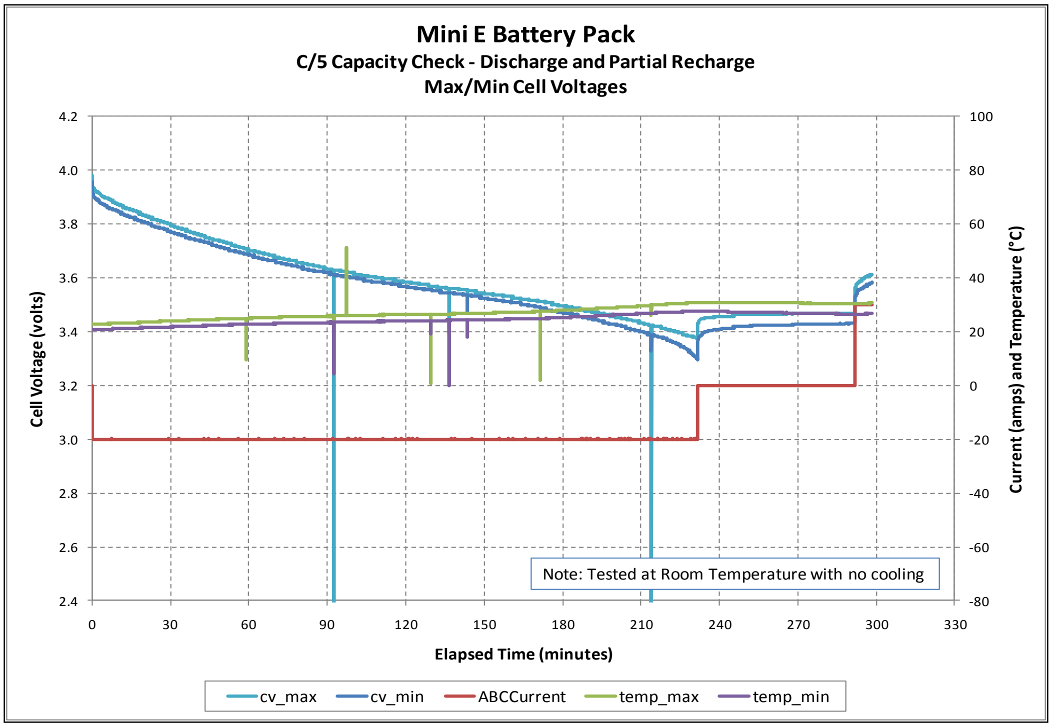

Figure 37: Max/min cell voltages during the discharge and partial recharge portion of C/5 capacity check

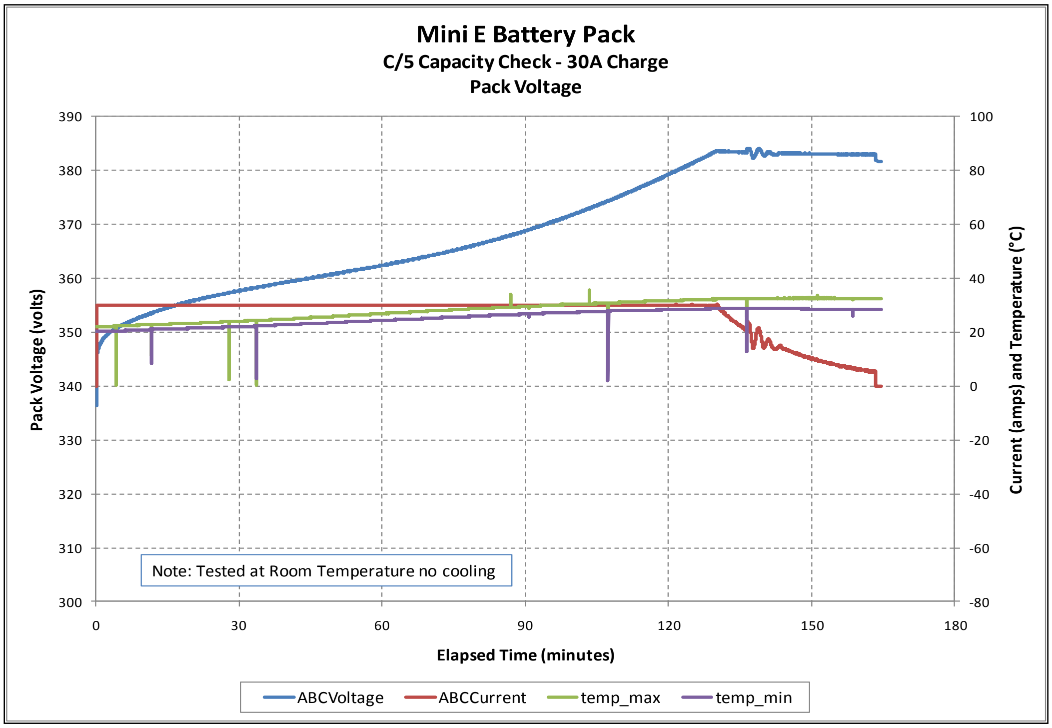

Figure 38: Pack voltage during the full recharge portion of the C/5 capacity check

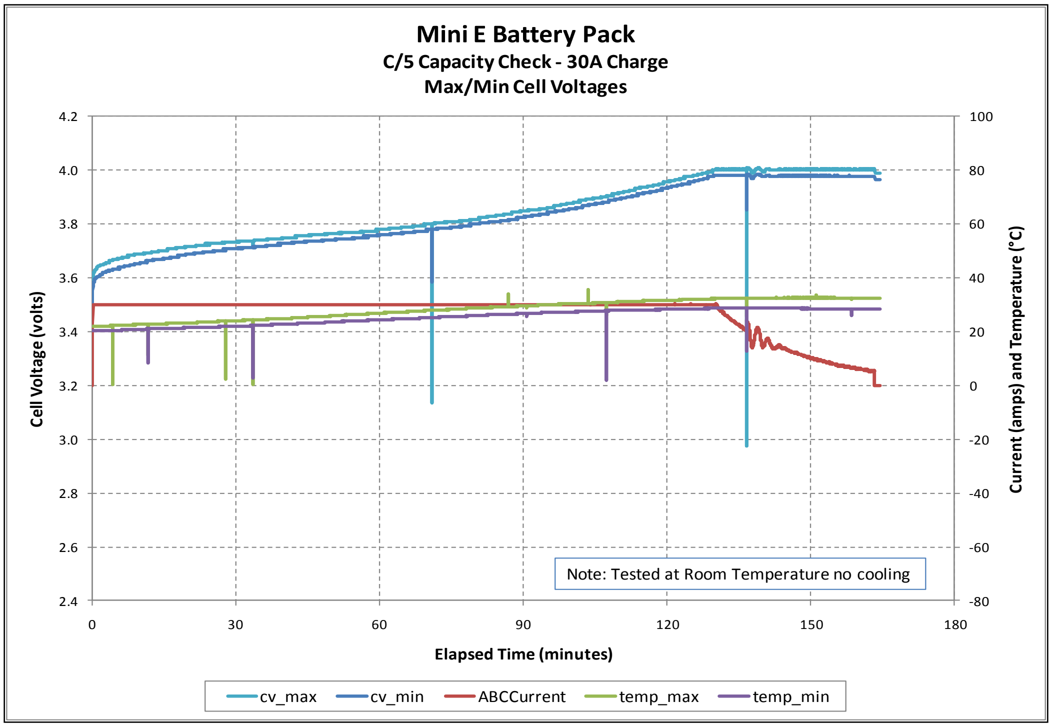

Figure 39: Max/min cell voltages during the full recharge portion of the C/5 capacity check

Testing Results: Pulse Power Test

Table 10: Pulse Power Test – Discharge Pulse Summary. Source: AeroVironment, Table 11, and Figure 40 show the test results for the pulse power test. The discharge and charge pulses were performed at different states of charge (SOC). Starting with a fully charged battery pack, a 10 second 4·C (413.4 A) discharge pulse was performed. For each SOC step following that, a 4·C (413.4 A) discharge pulse and a 3·C (310.1A) charge pulse were performed. When the pack became fully discharged a 10 second 3·C (310.1A) charge pulse was done.

The Mini E battery pack was not able to deliver the requested 4C (413.4 A) and 3C (310.1 A) current levels due to the current being limited by the pack voltage limits. Table 10: Pulse Power Test – Discharge Pulse Summary. Source: AeroVironment and Table 11: Pulse Power Test – Charge Pulse Summary. Source: AeroVironment. show the actual discharge and charge current/power levels attained at each SOC step. Figure 40 shows the open circuit voltage (OCV) and calculated DC discharge and charge impedance at each SOC step.

Table 10: Pulse Power Test – Discharge Pulse Summary. Source: AeroVironment

103.35Ah Nameplate	DISCHARGE PULSES				
AH Removed	Requested Current (4·C	Actual (A)[3]	Power (kW)	Pulse Length (seconds)	Pulse Stopped on

---

[3] Current was limited by the ABC-170 hitting the lower pack voltage limit.

	amps)				
0	-413.4	-338.5	-107.2	1s	Lower CV limit
10.3	-413.4	-243.0	-77.0	10s	Time
31	-413.4	-171.5	-54.3	10s	Time
51.7	-413.4	-144.4	-45.7	2s	Lower CV limit
72.3	-413.4	-79.3	-25.1	2s	Lower CV limit
76.2	Charge Pulse Only				

Table 11: Pulse Power Test – Charge Pulse Summary. Source: AeroVironment.

103.35Ah Nameplate	CHARGE PULSES				
AH Removed	Requested Current (3·C amps)	Actual (A)[4]	Power (kW)	Pulse Length (seconds)	Pulse Stopped on
0	Discharge Pulse Only				
10.3	310.1	81.2	31.2	3s	Upper CV limit
31	310.1	161.1	61.8	< 1s	Upper CV limit
51.7	310.1	180.6	69.4	1s	Upper CV limit
72.3	310.1	223.3	85.7	2s	Upper CV limit
76.2	310.1	226.1	86.8	2s	Upper CV limit

---

[4] Current was limited by the ABC-170 hitting the upper pack voltage limit.

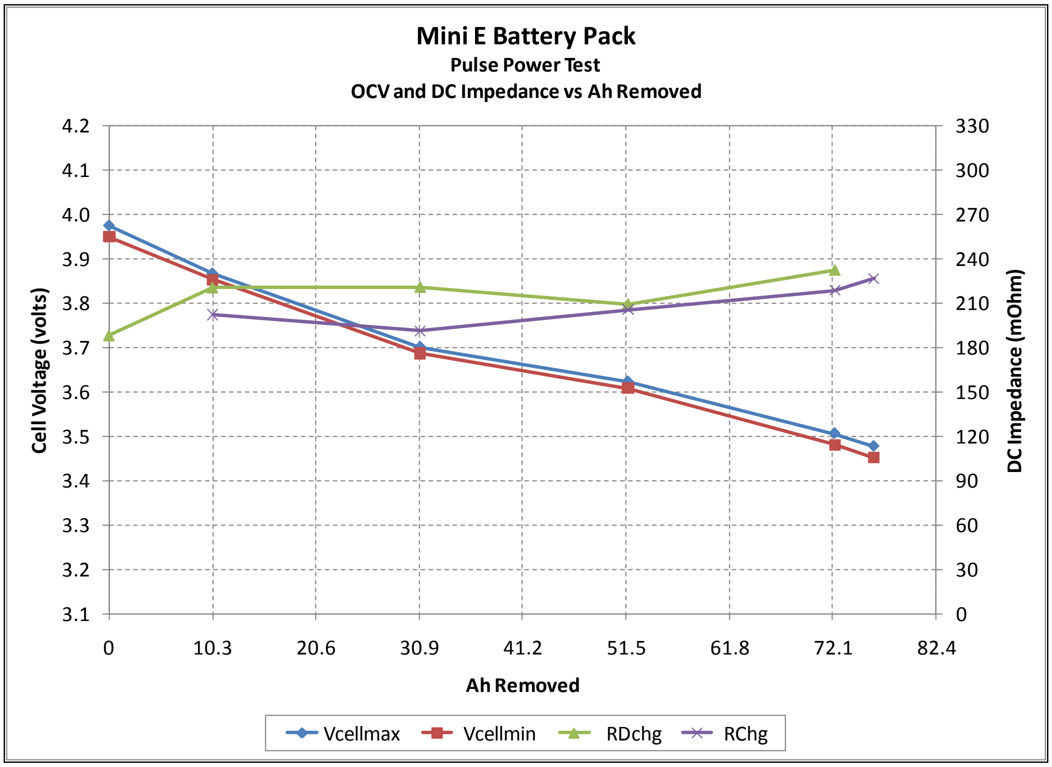

Figure 40: Open circuit voltage and DC Impedance versus Ah removed. Source: AeroVironment

Testing Results: Real Time Power Profile Test

The battery pack's 100 percent SOC rating was based on the C/5 Capacity Check test results. The 100 percent SOC capacity used for this test was 77.2 Ah. After fully charging the battery pack, it was discharged to 20 percent SOC by removing 61.8 Ah. Day 1 started at 20 percent SOC and Day 2 started at 24 percent SOC based on the power profile provide by KnGrid, so there was a slight SOC adjustment needed between Day 1 and Day 2.

An SOC calculation was made by integrating the Ah in and out and using 77.2 Ah as the full capacity divisor. The battery pack (VMS) also provided an estimated SOC based on the cell voltage values.

The power profile used was intended to cycle the battery pack between 20 percent and 80 percent SOC. Table 12 shows the energy throughput and Figure 41 and Figure 42 show the pack voltage, power, temperature and SOC (VMS estimated and integrated Ah), during the power profiles. Charts were split into Day 1 and Day 2 data. The VMS estimated SOC is labeled "batt_soc" and the software integrated SOC is labeled "ABCSOC" in the charts.

Table 12: RTM Power Profile – Energy Throughput and Efficiency. Source: AeroVironment

	Discharge (kWh Out)	Charge (kWh In)

Initial Discharge	21.6	
SOC Adjustment Charge (Between Days)		0.2
Cycling Discharge (Cumulative)	43.2	
Cycling Charge (Cumulative)		43.7
Re-Charge (Post-cycling to 100% SOC)		22.1

Total	64.8	66.0

Energy Efficiency	98.2%

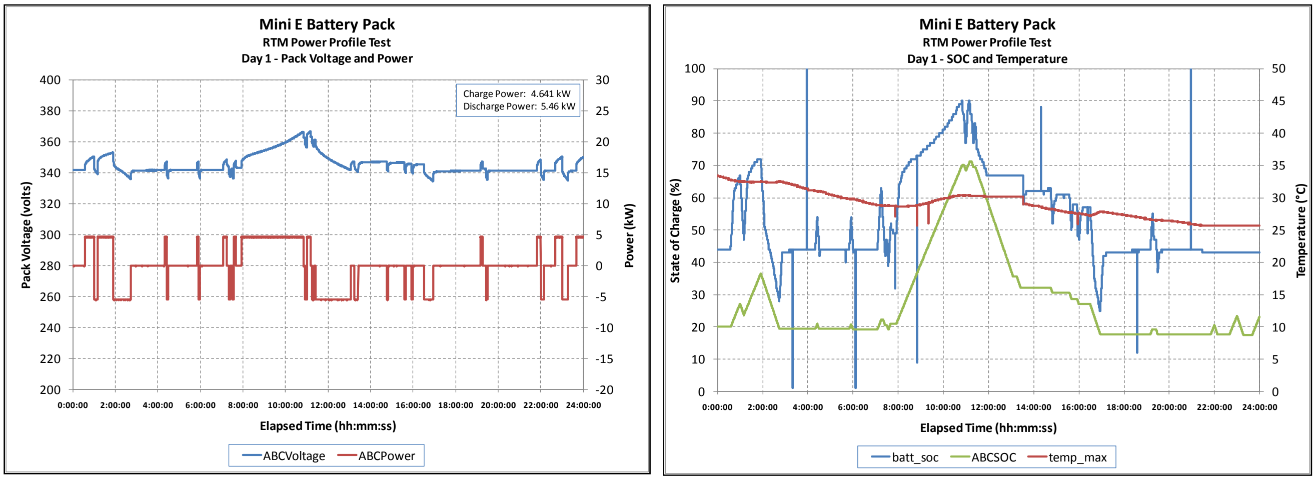

Figure 41 Left: Pack Voltage and Power. Right: SOC and Temperature during RTM Day 1. Source: AeroVironment

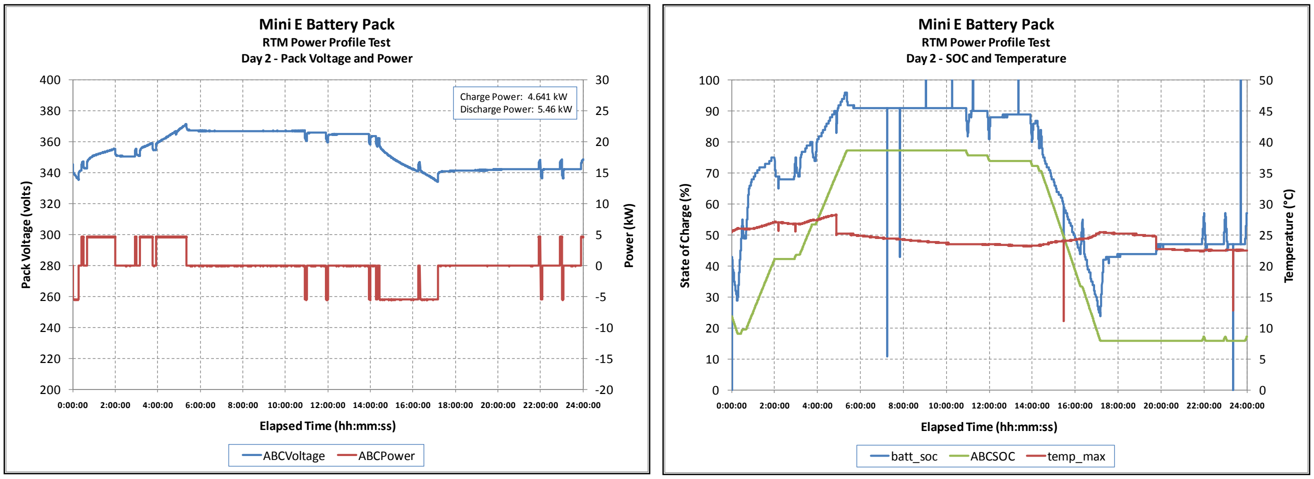

Figure 42 Left: Pack Voltage and Power. Right: SOC and Temperature during RTM Day 2. Source: AeroVironment

Table 13 Summary of Energy Throughput and Round Trip Efficiency. Source: AeroVironment

	kWh Out (Dchg)	kWh In (Chg)
Initial Discharge to 20% SOC	21.6	
Day 1	24.4	26.04
SOC Adjust		2.1
Day 2	18.8	17.6
Recharge to 100% SOC		22.1
Totals	64.8	67.8
Efficiency	95.6%	

5.6.2. Discussion of Battery Test Results

The battery pack's C/5 capacity was 77.2 Ah. This results in a 25 percent capacity loss from the nameplate capacity of 103.35 Ah. Some of the capacity loss may be due to the fact that the cells are not discharged in their full nominal voltage range, due to limits set on the test equipment. There was a 46.4°F (8°C) temperature rise over the course of the discharge. Due to an AeroVironment test requirement for this battery pack that did not allow unattended testing, the battery was re-charged three days later and had time to cool back to room temperature. The pack showed a 50°F (10°C) temperature rise during the 30A constant current-constant voltage charge. The pack also stayed well balanced and had a Max/Min delta cell voltage of 29 mV at the conclusion of this capacity test. The pack also showed an energy efficiency of 96 percent.

During the pulse power test, the discharge and charge power levels the test plan requested were not achieved. Instead, the battery pack hit the minimum pack voltage limit during the discharge pulses and the maximum pack voltage limit during the charge pulses. In each case the current was tapered to hold the pack voltage at each limit. The discharge pulses were stopped on time (10 seconds) or stopped when the minimum cell voltage reached the lower cell voltage limit. At the 10 percent and 30 percent DOD test points, the pack was able to complete a full 10 second discharge pulse, although at a limited current.
All the charge pulses were stopped due to the maximum cell voltage reaching the upper cell voltage limit. The longest charge pulse lasted for 3 seconds.

A Real Time Market (RTM) Power profile test was also performed. The power profile was generated by KnGrid and scaled to run on the Mini E battery pack. The profile was scaled based on the results of the C/5 capacity test. The power profile was intended to run between 20 percent and 80 percent SOC based on the available derated capacity. The maximum discharge power was scaled to be 5.46 kW for this test. The charge power, according to the power profile was 85 percent of the discharge power, 4.641 kW. Prior to running the power profile the pack needed to be discharge to 20 percent SOC, per the derated capacity. This discharge caused the pack to reach 93.2°F (34°C) prior to running the power profile. After the one hour rest period following the charge the pack cooled and the power profiles were started with the maximum temperature at 91.4°F (33°C). The power profile caused very little heating effects on the battery. Half way through Day 2 the battery pack was able to cool back down to room temperature. A VMS, supplied by BMW, was used to retrieve the Max/Min/Avg cell voltages and temperatures. It also reported an SOC based on the cell voltage readings. During this test the VMS reported SOC was always higher than the Ah integrated SOC the test software reported. This was due to the VMS not accounting for the battery pack’s capacity loss, whereas the test software used the derated capacity to calculate the SOC percentage.

The Mini E battery pack seemed well suited for some RTM applications based on the power profile tests. Based on the capacity test, the battery pack would also be ideal for demand applications if the power requirement was 5 kW or less and there was 5 hours allotted to recharge the battery pack.

5.6.3. Development of Control Algorithms

EV Charge Control / Demand Charge Management

Two important stationary applications that battery energy storage can provide to a commercial customer or the utility grid include EV charge control for Demand Charge Management and solar PV firming. With EV charge control, the battery energy storage system benefits the commercial customer by reducing the peak demand coming from charging an electric vehicle. With solar PV firming, the battery energy storage resource is used to provide a firm block of power to a utility customer. In this way, the utility is provided with predictable power over a predetermined period of time.

For development of the EV charge control algorithm, BMW chose to work with the California Center for Sustainable Energy. The California Center for Sustainable has been working with UC San Diego researchers and graduate students to develop an operational demand charge management algorithm. The operational algorithm has been tested in real-time on two battery packs located at the Hopkins Battery Test Facility. The two packs that have been tested are an A123 lithium iron phosphate ack (57 Ah nameplate) and an EnerDel manganese oxide pack (72 Ah nameplate). In the current demand charge management algorithm, one of the inputs is a building load from a meter at the UC San Diego microgrid. An EV charge control algorithm works in a similar fashion, with the building load replaced with the electric vehicle charging load.

The electric vehicle charging station co-located to the BMW Battery Container is separately metered and data from this meter is sent into the campus data warehouse, PI. The demand charge management algorithm tested and operated at the Hopkins Battery Test Facility, on two different battery packs, will utilize the charging station meter demand input and dispatch the BMW battery packs in a similar fashion to the A123 and EnerDel Packs.

Solar PV Firming

The solar PV firming algorithm was developed and tested on the A123 Battery Packs at the Hopkins Battery Test Facility. The solar PV firming algorithm was implemented in the software programming code Python and run through the Power Analytics software platform Paladin. The algorithm is programmed to begin at 1:30 pm, just as the typical PV load is peaking. The PV generation profile used in this algorithm is from a UC San Diego PV array located on its East Campus. The PV array generally has a daily peak load between 22 and 25 kW. The algorithm is programmed to respond to the fluctuating PV output and to provide the grid with a constant 17.5 kW. Therefore, the battery is required to discharge when the PV array drops below 17.5 kW and to charge when the PV array rises above 17.5 kW by the difference in PV load from 17.5 kW. At 1:30 pm, the battery typically begins charging, but as the day elapses, the battery discharge as PV production ramps down. The algorithm is programmed to terminate when the battery’s minimum cell voltage is 2.6 V (0.1 V above the minimum cell voltage limit). Successful implementation of the solar PV firming algorithm is confirmed in Figure 43.

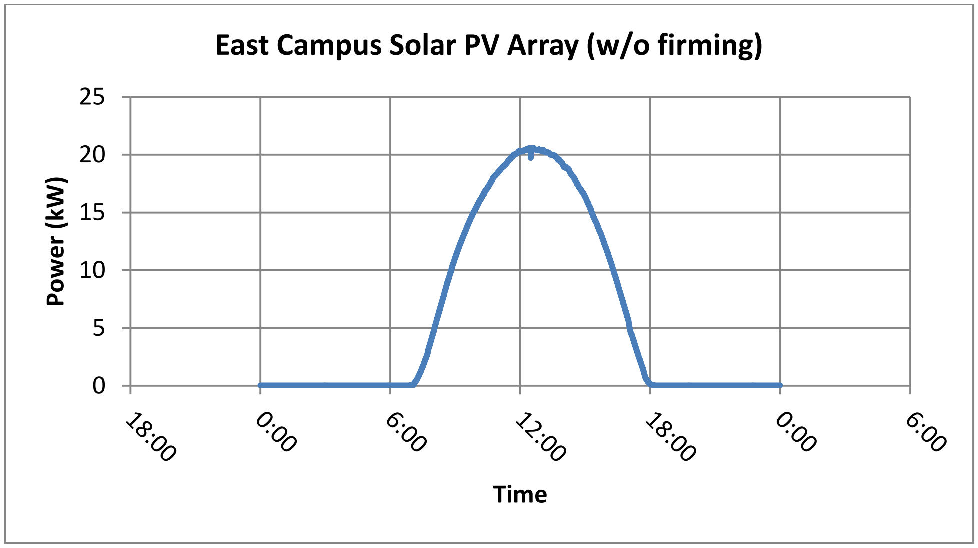

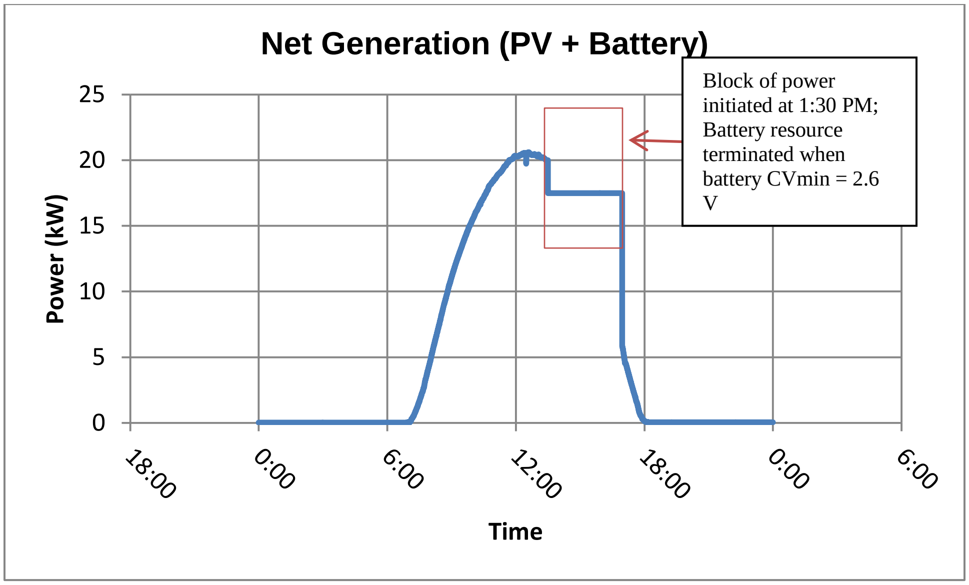

Figure 43: East campus solar PV array output without (top) and with (bottom) firming.

5.7 BMW Energy Storage Project Status as of March 31, 2014

All communication systems have been verified including, BMW Battery Management Systems, Super Battery Management System (SBMS), Site Controller and Princeton Power Systems (PPS) inverter. Functional testing of the BMS to Super BMS and to the site controller has been completed by EVGrid and UCSD. The functional testing of the inverter and communications to the site controller needs to be completed in April 2014 by Princeton Power Systems, the manufacturer of the 100 kW power inverter. Demonstration of the battery ground fault detection and protection function remains to be tested, as of March 31, 2014, by Princeton Power Systems as part of the inverter functional testing, and is required prior to full power operation.

Once the functional testing is completed in April 2014, the startup sequence will begin which will include full power charge and discharge of the energy storage system, followed by direct EV charging from a Blink Ecotality Level II charging station via the BMW energy storage system. This will complete all system commissioning and open the way for executing the test plan. The test plan includes the Reference Performance Test (RPT), Demand Charge Management (DCM), and Regulation Energy Management (REM). UCSD, BMW, EVGrid, Princeton Power and CCSE will prepare an addendum to the DOE Final Report and post it to the DOE High PV Penetration web portal.

5.8. Conclusions of field testing of demand charge management algorithms

UCSD developed a linear programming routine to optimize the energy storage dispatch schedule for a grid-connected, combined photovoltaic-battery storage system (PV+ system). The optimization strategy targets demand charge management through a targeted peak load reduction, and leverages PV power output and load forecasts to determine the best trajectory for the battery storage output power in order to minimize demand charges. We simulated a broad range of PV+ system designs and performed a cost analysis to compare the financial benefits of our optimized energy storage dispatch schedule with basic off-peak/on-peak charging/discharging and real-time dispatch strategies. The performance and value of the optimization method were quantified in terms of energy bill savings attainable over the lifetime of the battery array. The net present value (NPV) of the battery array increased significantly (in the range $100k - $450k – or $220/kWh to $270/kWh – for some PV+ configurations) when energy storage was dispatched on the optimized schedule over the simple dispatch schedules that did not use forecast information. Lithium-ion batteries are not a financially viable storage technology in demand side, energy bill management applications at current (2011) market prices. The estimated Lithium-ion batteries become profitable at an installed cost of about $450/kWh, which is about 45% of 2011 market prices. The value of PV power output and load forecasts for the application studied in this paper is $51,000 ± $35,000. This study underscores the need to develop tools and techniques for quantitative modeling and analysis to improve estimates of the economic value of energy storage and forecasting for both utility and demand side applications. The method is considered to be a simple yet feasible approach to that end, which is useful for energy storage manufacturers, financiers and other industry professionals seeking to quantify the value of their product and forecast investment returns.

Field testing showed that the PV+ system programmed with the operationally functional dispatch scheme is successful as a non-coincident DCM mechanism given the nature of the load and the sizing of the PV+ system. Disregarding weekends and holidays (omission made throughout analysis), which do not contain a conspicuous daytime load spike (and hence contain little or no load to be shaved), the PV+ system reduced the demand charge on every day in the simulation. The daily measured load profile is similar during a given month, as is the daily clear sky PV profile, so the potential for consistent peak demand reduction is high. Indeed, the algorithm achieves a relatively consistent daily reduction in peak demand (25.6% average and 5.9% standard deviation for July, 20.5% average and 3.9% standard deviation in November); the standard deviation decreases to 3.4% in July when days during which the battery failed are omitted. Variation in daily reduction is caused primarily by differences in PV generation and forecast accuracy, which drive long-term discharge (i.e., over a day); the quantity and timing of quasi-random load and PV fluctuations (e.g., untimely load spikes that stress the PV+ system when the battery capacity is low, or pre-sunrise load spikes that add undesired conservatism), which drive short-term battery discharge (i.e., over a 15 min interval); and the relative timing of the onset of PV and the elevated daytime load, which determines how much load can be shaved by PV alone.

6. Field Testing and Validation of Power Flow Models

6.1. Executive Summary

One of the significant objectives of the High Penetration solar research is to help the DOE understand, anticipate, and minimize grid operation impacts as more solar resources are added to the electric power system. This report presents detailed models developed to model, interconnect and ultimately operate a PhotoVoltaic (PV) power plant as anticipated in the DOE SunShot initiative. Power models are used in power system analysis software packages to assess the impact of the integration of PV systems into power systems. The models presented here are developed in Paladin DesignBase software but frequently begin in a different modeling application and are then converted to Paladin DesignBase. To make the models available to a wider engineering community, several conversion routines were developed (e.g. conversion to OpenDSS, Matlab®/Simulink® etc.), discussed, and reviewed in this paper. The approach and capabilities developed through the combined research, including the power modeling, forecasting, ramp control and energy storage (battery charging/discharging) have already been used in several commercial projects for island communities in Puerto Rico, which is widely considered the most stringent and difficult application for PhotoVoltaic integration, control and operation. This work was also largely presented in the Webinar provided by Power Analytics and attended by over 120 individuals on March 27, 2013.

6.2. PV Plant Power Flow Model

An appropriate steady-state model for PhotoVoltaic is implemented in the DesignBase Advanced Power Flow software. The model is based on steady-state behavior of a PV plant with sophisticated control strategy:

1. A photovoltaic power plant modeled as a generator in steady-state analysis.
2. The aggregated MVA of the plant which must be specified as the sum of individual inverter MVA ratings. (The active power dispatch is between 0 and the aggregate MVA.)
3. The default operating mode of the inverter is unity power factor (Qmax = Qmin = 0).
4. Some inverters operate with ± 0.95 power factor. Only 95% of the inverter current is available for kW dispatch. The difference remains for reactive power control. Qmax and Qmin should be provided and Q should remain within the limits.
5. If the inverter controls the voltage of a given bus, then the PV generator will operate in P-V mode, and the controlled bus should be specified.
6. PV Output Power depends on irradiance. Therefore, the PV Active Power Output depends on time. Variation of sun irradiance has to be considered as input power.

The following figures show the PV model load flow tab in both constant P-Q and constant P-V modes.

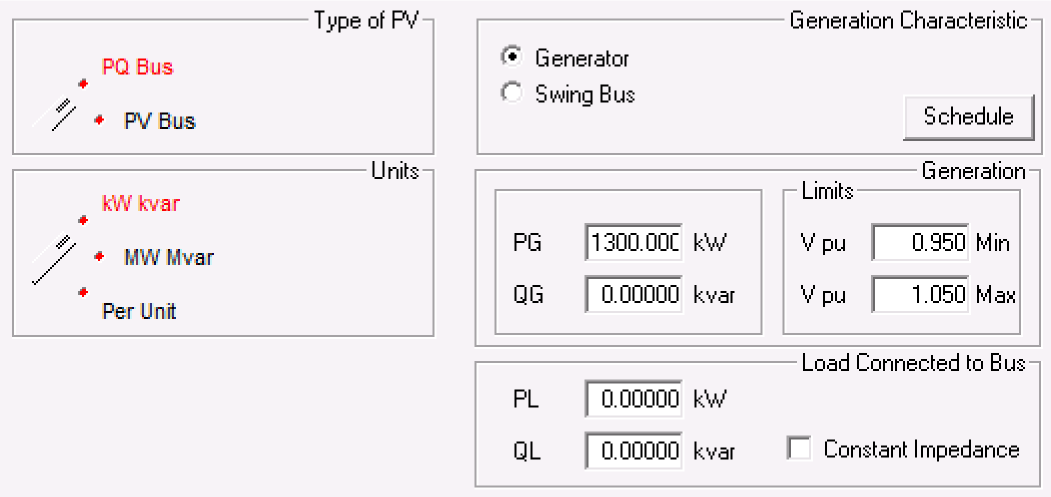

Type of PV
PQ Bus
PV Bus

Units
kW kvar
MW Mvar
Per Unit

Generation Characteristic
● Generator
○ Swing Bus

Generation
PG 1300.00 kW
QG 0.00000 kvar

Limits
V pu 0.950 Min
V pu 1.050 Max

Load Connected to Bus
PL 0.00000 kW
QL 0.00000 kvar
☐ Constant Impedance

Figure 44 - PV plant model as constant P-Q bus

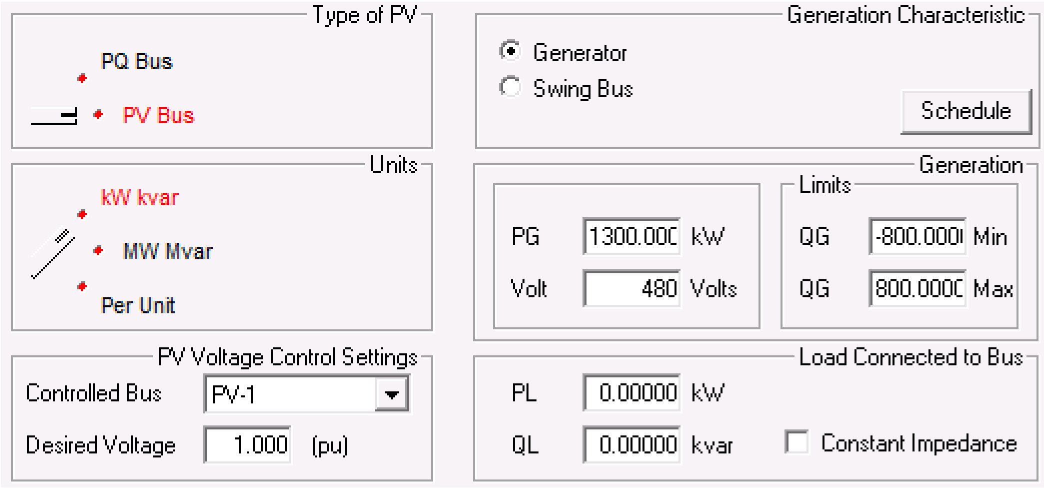

Type of PV: ○ PQ Bus ● PV Bus

Units: ● kW kvar ○ MW Mvar ○ Per Unit

Controlled Bus: PV-1

Desired Voltage: 1.000 (pu)

Generation Characteristic: ● Generator ○ Swing Bus

PG: 1300.00 kW

Volt: 480 Volts

QG: -800.000 Min

QG: 800.000 Max

PL: 0.00000 kW

QL: 0.00000 kvar

☐ Constant Impedance

Figure 45 - PV plant model as constant P-V bus

Typically, special consideration is given to variable irradiance data. Multiple power system studies are performed to evaluate the impact of volatile irradiance on PV plant ramp rates, frequency support, etc. One of the ways to study this phenomenon is to perform consecutive power flow studies by feeding the variable irradiance input to the system.

An example of doing this using Paladin Research Lab is presented next. The Paladin Research Lab interface enables writing the data to the DesignBase database, running the analysis and reading the results, all by using the custom tailored code in various software platforms. Multiple software tools can be used to programmatically interface with the DesignBase models. This example illustrates the use of MATLAB. The code presented next reads the variable irradiance data (recorded in 5-second interval), applies a ramping algorithm to maintain the ramp below the allowable level, and charges the battery where there is excess of sun energy or discharges the battery where there is not enough sun energy.

```
% function [Start,Obj,Text] = CasePV
clear
clc
ck1=clock;
T=load('IRR.mat');
% case 1---------------------------------------------
cIrr=T.covercast20121113;
Irr=T.overcast20121113;

% Instantiate the Model Object
model = actxserver('PA.ResearchLab.Model');
fprintf('\n ------------------------------------------------------------------------Creating Research-Lab Interface....\n');

% Open the MDB file, You need to set this path for MATLAB use
model.Open('C:\DesignBase5\Projects\PUERTORICO\PUERTORICO.MDB');

fprintf('\n ------------------------------------------------------------------------connecting to DesignBase succesfully....\n');
%     fprintf('   Time(Hour)        System Loss(kW)      Bus PCC Voltage(V)')

k=0; % counter
TotalPVGen=0; %PV MWh varaible
TotalPREPAGen=0;  %PREPA MWh variable
TotalLoss=0;    %System Loss Variable kWh
TotalBatteryPow=0;    %Total Battery Power MWh
TotalBatteryLD=0;    %Total Battery Power LDF Results MWh

% Sampling Information
samplingrate=5; %PV data sampling rate (=5 sec)
step=100;    %  down-sampling rate == step*sampling rate(=5 sec)
Nsample=24*60*60/samplingrate; % Number of total samples
nsample=Nsample/step; % Number of down-sampled data

% Battery
Nbatt=6; % Number of Battery Banks
SOCnom=Nbatt*1120; % Nominal SOC [kWh]
SOCmax=1*SOCnom; % Maximum SOC [kWh]
SOCmin=0.7*SOCnom; % Minimum SOC [kWh]

SOC(1)=Nbatt*0.9*1120; % Primary State of the Charge of the Battery [KWh] (SOCmin< SOC< SOCmax)

% Set some values
for r = 4320:step:13680
    k=k+1;

    PowerIrr(k)= Irr(r);    % MW
    Batt(k)= (cIrr(r)-Irr(r)); % MW: + Discharge  - Charging

    BattP(k)=min((max (Batt(k),-Nbatt*0.6)),Nbatt*1.1); % Battery Power Limitation [kW]  + Discharge  - Charging

    BKWh(k)=SOC(k)-BattP(k)*(samplingrate*step/3600);
        if BKWh(k) > SOCmax
          BattP(k)=min((max ((SOCmax-SOC(k))/(samplingrate*step/3600),-Nbatt*0.6)),Nbatt*1.1);
        end
        if BKWh(k) < SOCmin
          BattP(k)=min((max ((SOC(k)-SOCmin)/(samplingrate*step/3600),-Nbatt*0.6)),Nbatt*1.1);
        end
    SOC(k+1)= SOC(k)-BattP(k)*(samplingrate*step/3600);

    model.SetBusPropertyValue('BAT-1:P', BattP(k)*1000/Nbatt);
```

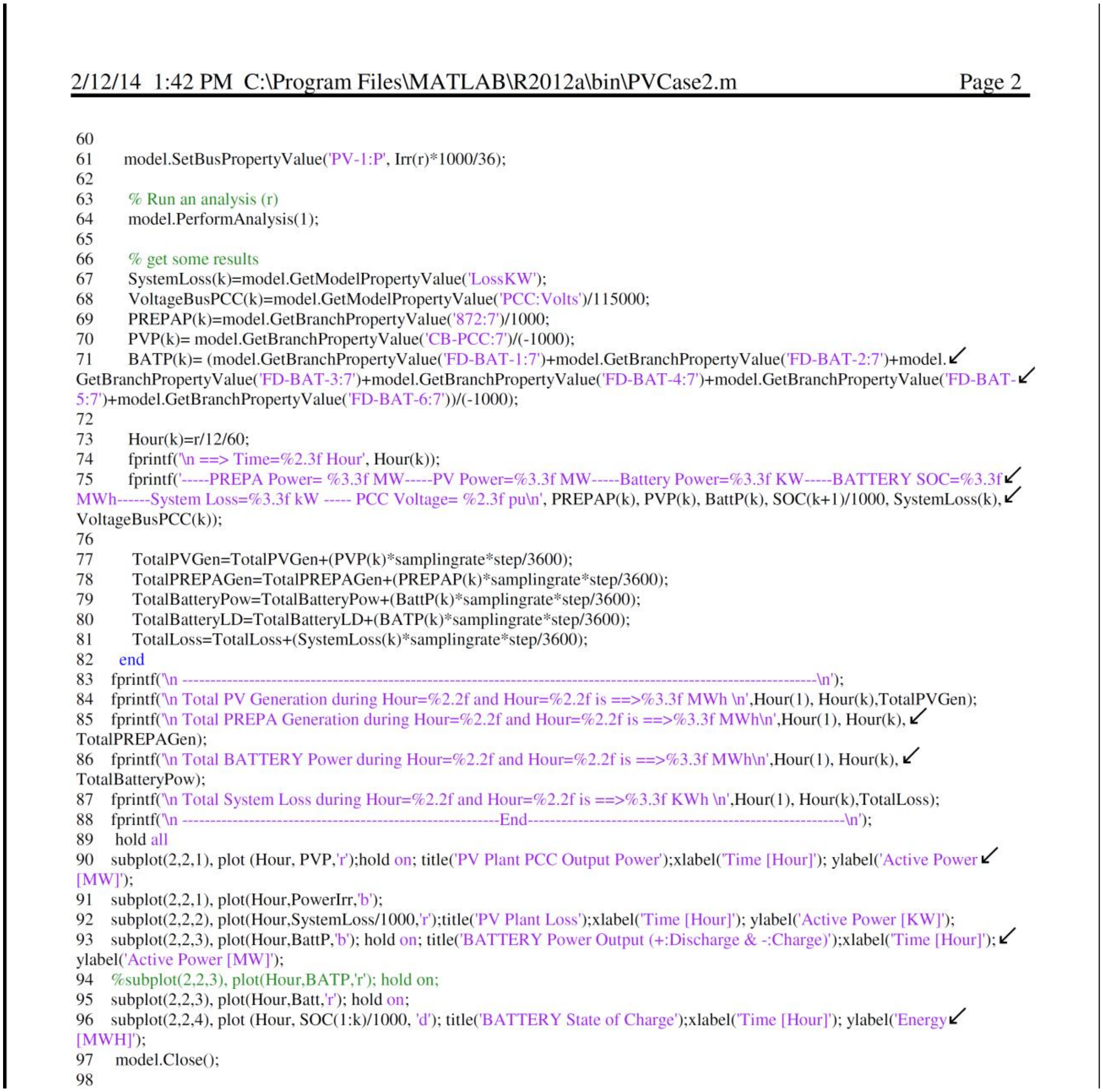

2/12/14 1:42 PM C:\Program Files\MATLAB\R2012a\bin\PVCase2.m Page 2

```

    model.SetBusPropertyValue('PV-1:P', Irr(r)*1000/36);

     % Run an analysis (r)
     model.PerformAnalysis(1);

     % get some results
     SystemLoss(k)=model.GetModelPropertyValue('LossKW');
     VoltageBusPCC(k)=model.GetModelPropertyValue('PCC:Volts')/115000;
     PREPAP(k)=model.GetBranchPropertyValue('872:7')/1000;
     PVP(k)= model.GetBranchPropertyValue('CB-PCC:7')/(-1000);
     BATP(k)= (model.GetBranchPropertyValue('FD-BAT-1:7')+model.GetBranchPropertyValue('FD-BAT-2:7')+model.↙
GetBranchPropertyValue('FD-BAT-3:7')+model.GetBranchPropertyValue('FD-BAT-4:7')+model.GetBranchPropertyValue('FD-BAT-↙
5:7')+model.GetBranchPropertyValue('FD-BAT-6:7'))/(-1000);

     Hour(k)=r/12/60;
     fprintf('\n ==> Time=%2.3f Hour', Hour(k));
     fprintf('-----PREPA Power= %3.3f MW-----PV Power=%3.3f MW-----Battery Power=%3.3f KW-----BATTERY SOC=%3.3f↙
MWh------System Loss=%3.3f kW ----- PCC Voltage= %2.3f pu\n', PREPAP(k), PVP(k), BattP(k), SOC(k+1)/1000, SystemLoss(k),↙
VoltageBusPCC(k));

      TotalPVGen=TotalPVGen+(PVP(k)*samplingrate*step/3600);
      TotalPREPAGen=TotalPREPAGen+(PREPAP(k)*samplingrate*step/3600);
      TotalBatteryPow=TotalBatteryPow+(BattP(k)*samplingrate*step/3600);
      TotalBatteryLD=TotalBatteryLD+(BATP(k)*samplingrate*step/3600);
      TotalLoss=TotalLoss+(SystemLoss(k)*samplingrate*step/3600);
  end
 fprintf('\n ------------------------------------------------------------------------------------------------------------------\n');
 fprintf('\n Total PV Generation during Hour=%2.2f and Hour=%2.2f is ==>%3.3f MWh \n',Hour(1), Hour(k),TotalPVGen);
 fprintf('\n Total PREPA Generation during Hour=%2.2f and Hour=%2.2f is ==>%3.3f MWh\n',Hour(1), Hour(k), ↙
TotalPREPAGen);
 fprintf('\n Total BATTERY Power during Hour=%2.2f and Hour=%2.2f is ==>%3.3f MWh\n',Hour(1), Hour(k), ↙
TotalBatteryPow);
 fprintf('\n Total System Loss during Hour=%2.2f and Hour=%2.2f is ==>%3.3f KWh \n',Hour(1), Hour(k),TotalLoss);
 fprintf('\n ---------------------------------------------------------End--------------------------------------------------------\n');
  hold all
 subplot(2,2,1), plot (Hour, PVP,'r');hold on; title('PV Plant PCC Output Power');xlabel('Time [Hour]'); ylabel('Active Power↙
[MW]');
 subplot(2,2,1), plot(Hour,PowerIrr,'b');
 subplot(2,2,2), plot(Hour,SystemLoss/1000,'r');title('PV Plant Loss');xlabel('Time [Hour]'); ylabel('Active Power [KW]');
 subplot(2,2,3), plot(Hour,BattP,'b'); hold on; title('BATTERY Power Output (+:Discharge & -:Charge)');xlabel('Time [Hour]');↙
ylabel('Active Power [MW]');
 %subplot(2,2,3), plot(Hour,BATP,'r'); hold on;
 subplot(2,2,3), plot(Hour,Batt,'r'); hold on;
 subplot(2,2,4), plot (Hour, SOC(1:k)/1000, 'd'); title('BATTERY State of Charge');xlabel('Time [Hour]'); ylabel('Energy↙
[MWH]');
  model.Close();

```

Figure 46 – Sample Code

Figure 35 is generated as one of the outcomes of the above code. It shows only one slice of the analyzed day, including volatile irradiance ramps, curtailed PCC power, and battery charging and discharging and its state of charge.

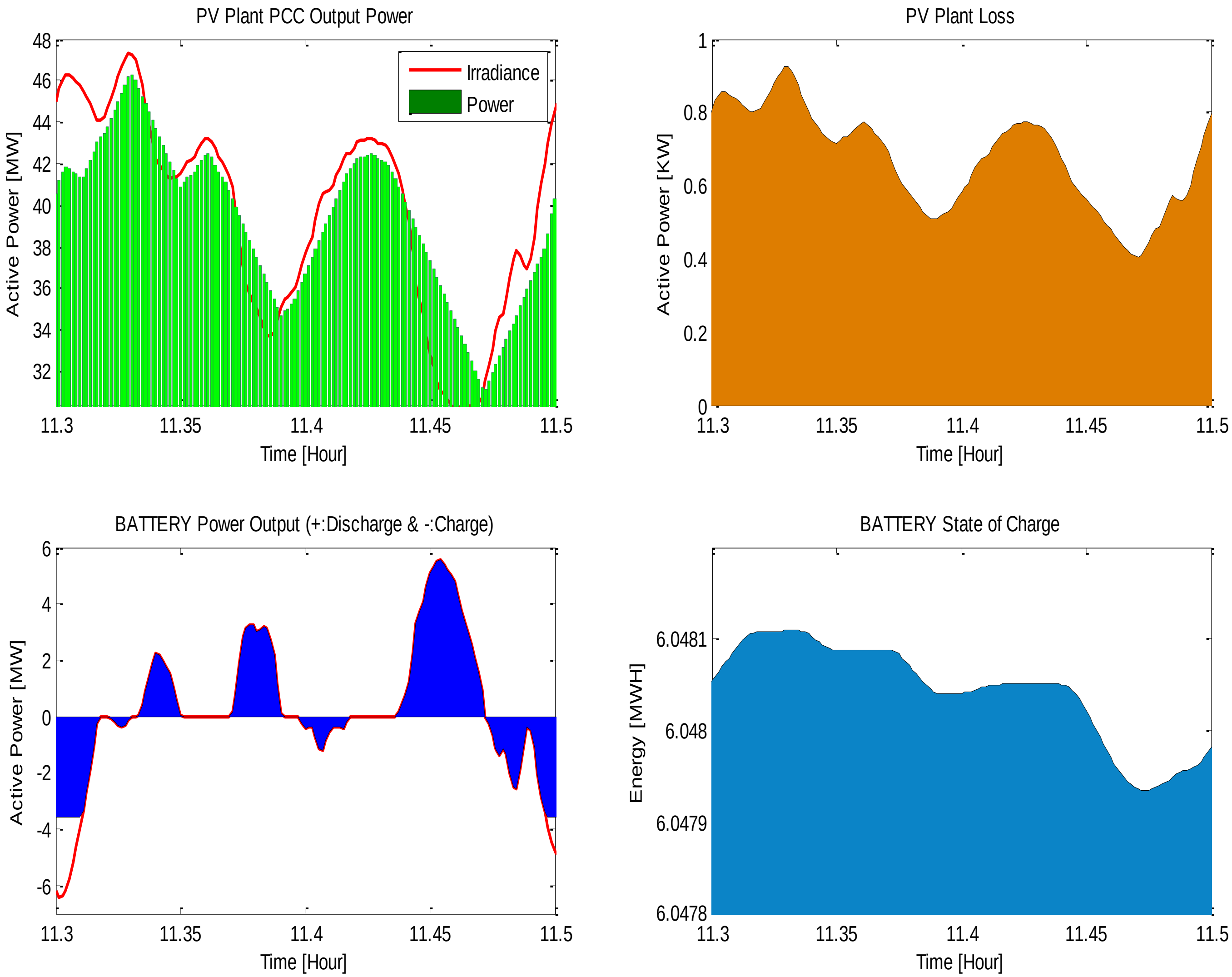

Figure 47 - PV plant output during a curtailment based on weather forecast and battery charge/discharge

6.3. PV Plant Transient Stability (Time Domain) Model

A generic PV/Inverter dynamic model has been implemented as a user-defined model in DesignBase's Advanced Transient Stability Program.

For most transient stability studies, the response of the plant to grid disturbances (faults) is of most interest. For these studies, the model should calculate the initial solar radiation based on the plant's active power output in the power flow solution. This radiation can be kept constant throughout the transient simulation time. The output power of the inverter and radiation result in a DC voltage that is a predictable function of the PV characteristics with virtually no dynamics. The DC voltage error is processed through a proportional-integral regulator whose output is the inverter direct axis current that results in active power production. Additional control for voltage regulation is also supported in this model.

The model also supports under/over-voltage protection in addition to under/over-frequency protection. Three levels of under-voltage tripping and one level of over and under-frequency tripping are included in the generic PV/inverter model. Each of these trip functions has an independent associated time delay.

The control block diagram of the 'Generic Photovoltaic/Inverter Model' is shown in next page. The following parts can be identified from this model:

- Photovoltaic array models considering the Lorenz equation
- Active and Reactive power controls
- Under-Voltage Protection
- Over/Under-frequency protection
- Irradiance input control

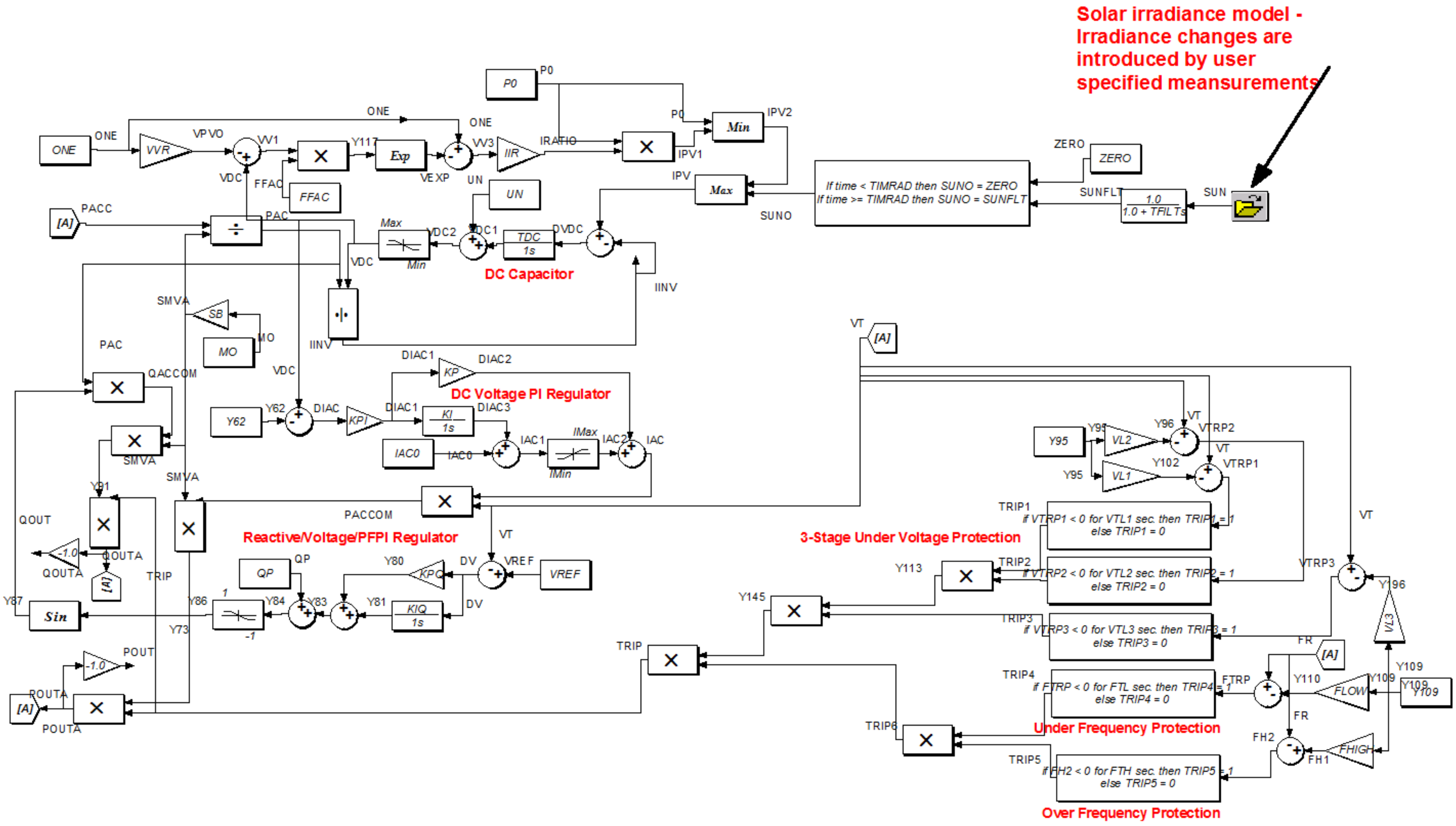

Solar irradiance model - Irradiance changes are introduced by user specified meansurements

Figure 48 - Generic PV/Inverter Model

6.3.1. Description of Functional Block within the PV Plant Transient Stability Model

A simplified presentation of the PV/inverter dynamic model is shown in Figure 5 and consists of a PV array model, Maximum Power Point Tracking system, voltage and active power controllers, and an inverter.

The irradiance model includes inputs for solar irradiance and active power output. The DC voltage is the only output. The DC capacitor is also included. The DC voltage output of the PV array is then fed into the MPPT model to calculate the optimum DC Voltage reference.

For most transient stability studies, the response of the plant to grid disturbances (short circuits) is of most interest. For these studies, the model should calculate the initial solar radiation based on the plant's active power output in the power flow solution. This radiation should be kept constant throughout the transient simulation time. The output power of the inverter and radiation results in a DC voltage that is a predictable function of the PV characteristics with virtually no dynamics. The DC voltage error is processed through a proportional-integral regulator whose output is the inverter direct axis current I_p that results in active power production.

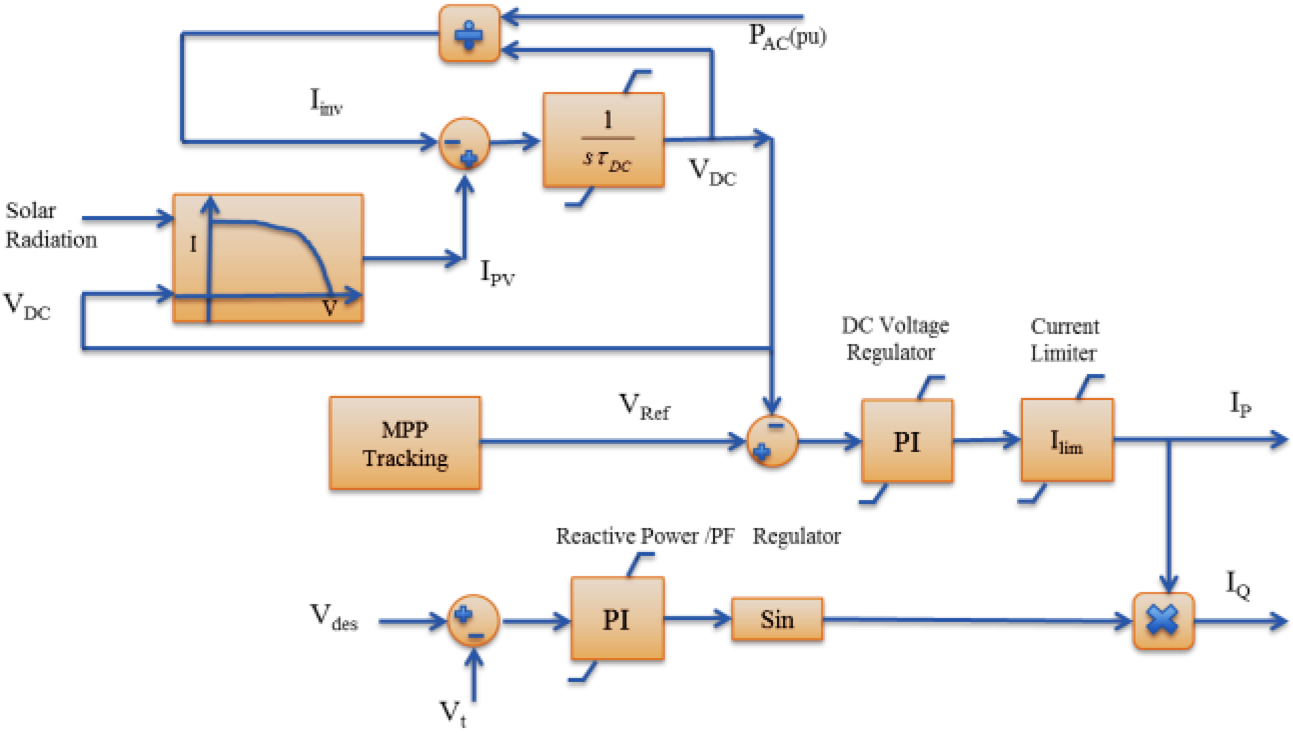

Figure 49 - PV/Inverter Model – Simplified Block Diagram

Irradiance Model:

The PV current, I_{PV}, is a function of the array output voltage V_{PV} (V-I characteristic of the array) which is calculated by:

$$I_{PV} = P_0 \times I_{IR}\left(1 - e^{\frac{\log(1-\frac{1}{I_{IR}})}{1-V_{VR}}(V_{DC}-V_{VR})}\right) \qquad \textbf{Equation 16}$$

Where:

- **I_{IR}:** Ratio of PV short circuit to peak power output current (Isc/Imp)
- **V_{VR}:** Ratio of PV open circuit voltage to peak power output voltage (Voc/Vmp)
- **V_{DC}:** DC Voltage
- **P_o:** Ratio of PV active power to Base Power (Inverter Rating)
- **I_{PV}:** PV output current

The following model presents the block diagram implemented this equation. In addition, the simulation results for injected V_{DC} signal output PV current are shown. In t=1 sec a disturbance (three phase bolted SC at PV terminal with Δt=0.1 sec) in the network causes a DC voltage rise momentarily and the PV current follows this disturbance according to its I-V curve.

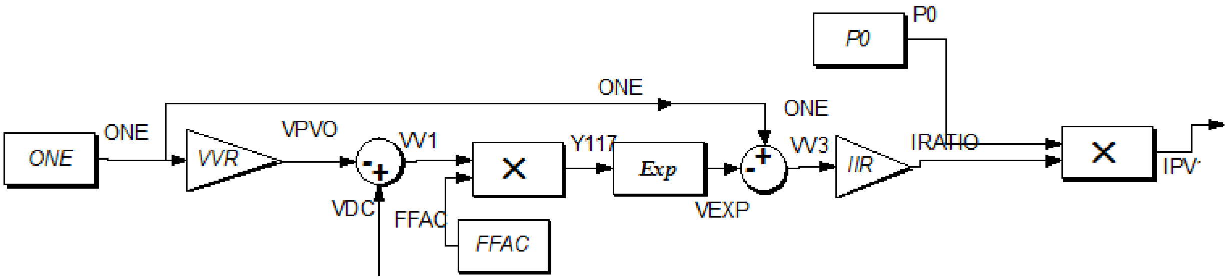

Figure 50 - PV Cell I-V characteristic implemented in DesignBase Transient Program

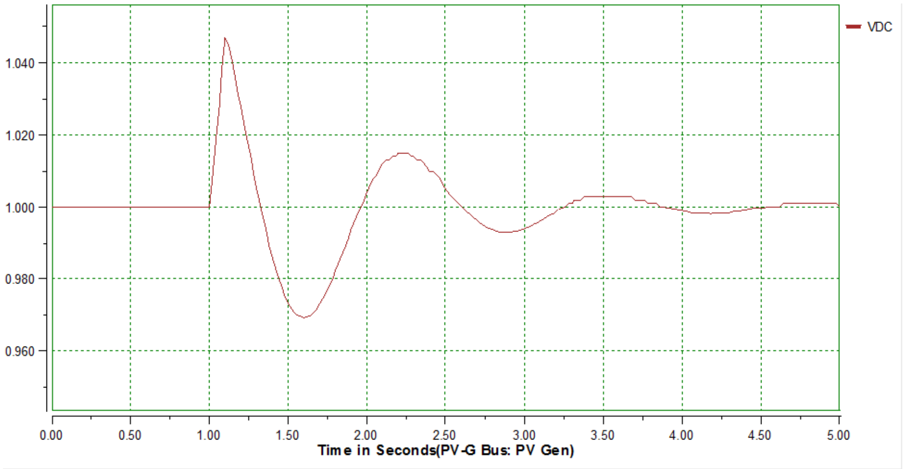

Figure 51 - PV cell I-V characteristic input V_{DC} transient signal during the network disturbance at t=1 sec

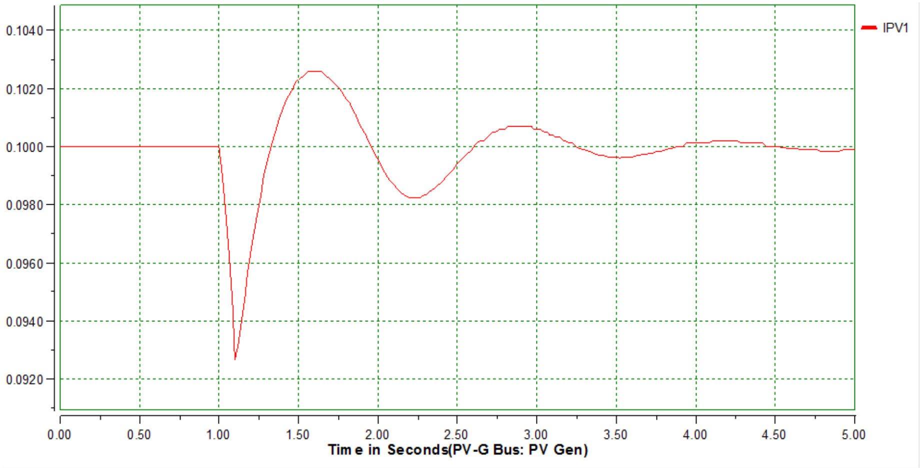

Figure 52 - PV cell I-V characteristic output I_{PV} transient signal during the network disturbance at t=1 sec

6.3.2. Transient simulation utilizing developed models

Several simulations in this section are used to illustrate the behavior of the model and the types of problems in which this model can be utilized.

Protection Simulation

This simulation demonstrates under-frequency protection. The frequency at PCC is decreased at t = 10 sec. As the system is working at the maximum power point, the inverter is not able to increase MW production in an attempt to regulate the frequency. At t =11.9 sec PCC frequency goes below 57 Hz and at t = 12.7 sec the trip signal takes out PV system.

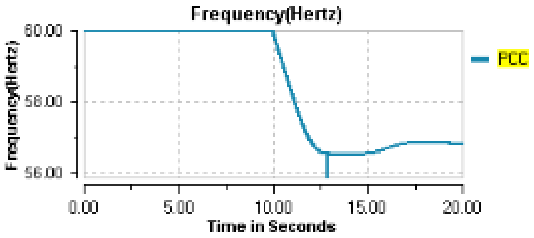

Figure 53 - Frequency at PCC during an under-frequency event

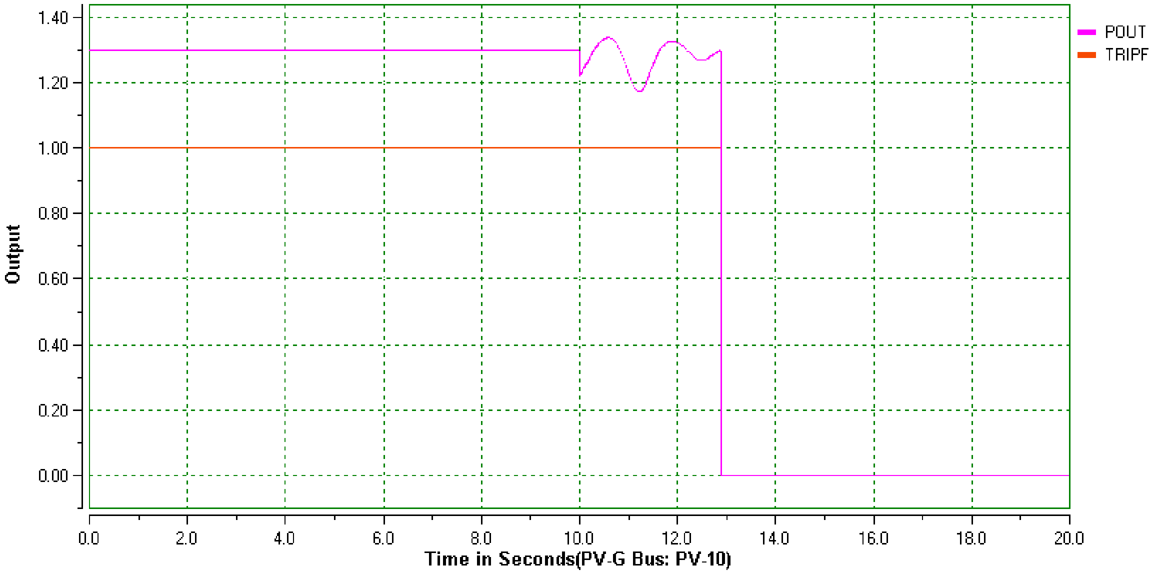

Figure 54 - Under-frequency PV trip

Voltage Regulation Simulation

Demonstration of voltage regulation capability is shown next. During the under-voltage conditions, the inverter supports voltage by injecting additional reactive power.

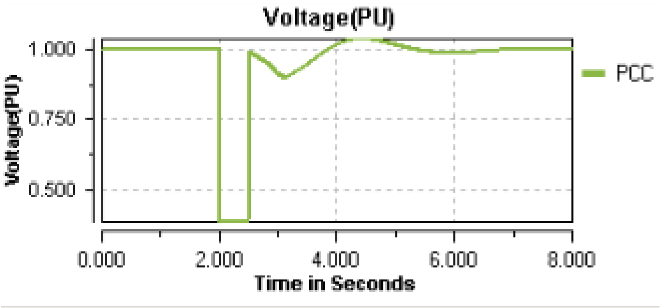

Figure 55 - PCC voltage during a fault

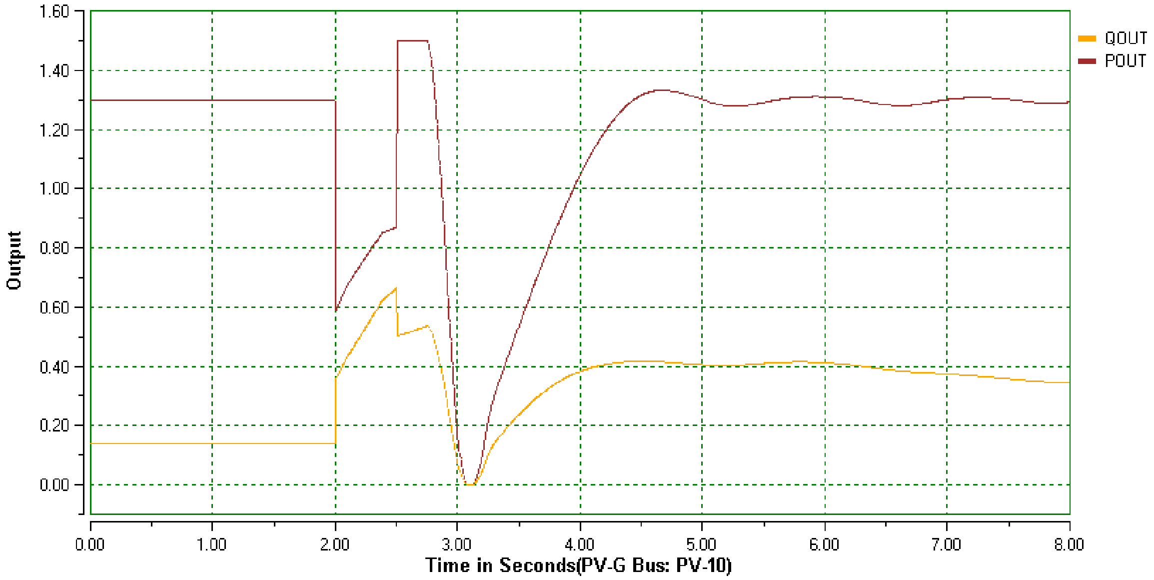

Figure 56 - Frequency support

Irradiance Variation Simulation

The figure below shows the impact of the variable sun irradiance on the power production of the PV plant; data for this sun irradiance variation is recorded at UCSD (real weather data). The data includes a fast transient from maximum power to 40% of the maximum power within 5 seconds and several subsequent power swings.

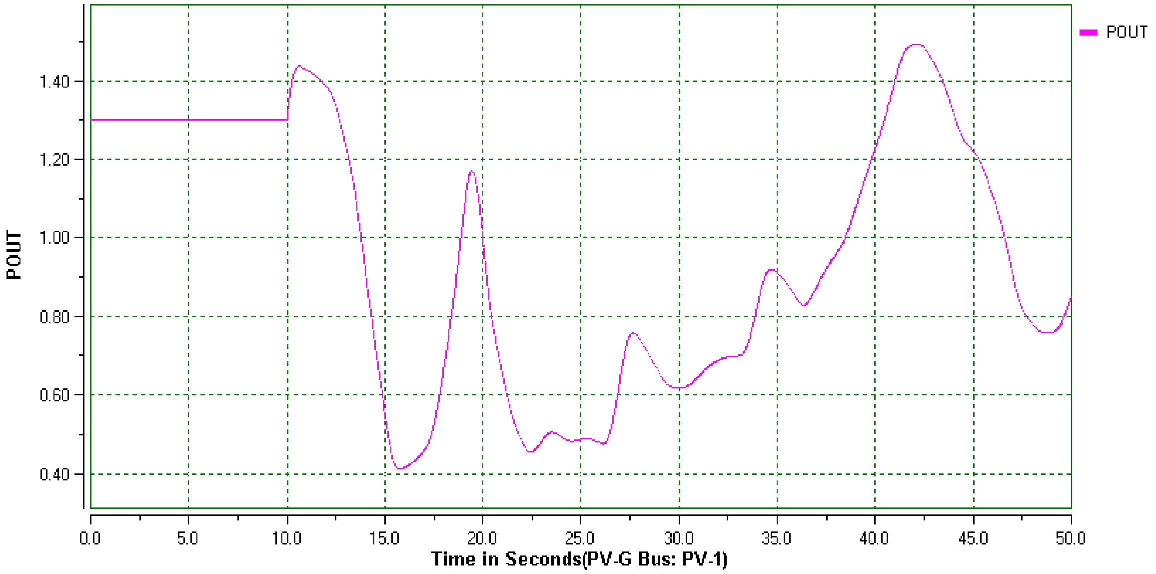

Figure 57 - Irradiance variability

6.4. Battery/Converter Generic Model

A generic model of a Lithium-Ion battery is included. The model can be easily adapted to any other battery technology depending on the final choice of the manufacturer. In addition the battery range of operation planned for the PV plant should be far from the maximum charge and total discharge where battery technology plays an important role. In other words, the model used here can represent different battery technologies for range of our application. Based on various manufacturers' data the following battery parameters are used in the simulation. The battery bank consists of groups wired both as series and parallel lithium-ion cells. The cell data are utilized to derive the total storage battery parameters for transient study. For instance, the assumed battery parameters based on the considered battery model for our study are presented in following table.

Table 14. Assumed Battery Parameters

No.	Parameter	Value	Unit
1	Rated Capacity @ time 30 min, 1 Hour, etc.	800	Ah @ 30 min
2	Maximum Capacity (MWh)	0.56	MWh @ 30 min
3	Maximum Discharge Power (MW)	1.1	MW
4	Maximum Discharge Current (A)	1900	A
5	Nominal Charge Power (MW)	0.6	MW
6	Max. Short duration Charge Power (MW)	1	MW
7	Nominal Voltage (V)	700	V
8	Maximum Recharge Voltage (V) [Fully Charged Voltage]	812	V
9	Open Circuit Voltage (V) [No-Load Voltage]	696	V
10	Discharge Termination Voltage (V)	609	V
11	Internal Resistance (Ω)	0.001	Ω
12	Battery response time (sec) [1]	30	Sec
13	Exponential Capacity Q_{exp} (MWh or Ah) [2]	240	Ah
14	Exponential Voltage (V) [3]	657.7	V

1: The response time of the battery. This is the time at which the change in battery voltage is 95% of its total charge due to a change in discharge current. It value represents the voltage dynamics for a current step change.

2: The state of charge or the energy storage at the end of the exponential period .Q_{exp} should be less than Q_{nom}.

3: The battery voltage at the end of the exponential period. This voltage should be in between V_{nom} and V_{full}.

Exponential Zone of Discharge Curve: The exponential voltage (V_{exp}) and the exponential capacity (Q_{exp}) corresponding to the end of the exponential zone. The voltage should be between V_{nom} and V_{full}. The capacity should be between 0 and Q_{nom}.

The lithium-Ion battery model is implemented in DesignBase software as shown in Figure 26, and is based on the battery dynamic behavior during the charging/discharging modes and system power request. This model receives the battery DC current as an input and calculates the battery DC voltage. This model is capable of tracking the state of the charge (SOC) of the battery during the simulation time and in addition provides appropriate transient behavior of battery voltage during charge and discharge modes by modeling the charge/discharge voltage curves versus the energy usage. This feature is not included in steady-state battery models (as the one depicted in Section 2) and therefore this will result in more precise simulation of battery behavior during the system dynamics rather than the load flow study.

In order to demonstrate the model performance in transient analysis, a simple case is run for switching between discharging to recharging modes by injecting the DC current step change according to Figure 29. This figure shows that the DC current in battery dynamic model is changed, for instance from 1378 A in discharging mode to 820 in charging mode at t=50 sec. The transient simulation results in the battery voltage changes in Figure 30. As shown in this picture the voltage starts to decrease during discharge (746.7 V to 738 V) and then starts to increase during the recharging (738 V to 750 V). The voltage changes are based on the charge/discharge curve versus the lost energy in the battery.

Accordingly, the state of the charge of the battery is calculated during simulation time and is shown in Figure 31. As is depicted in this figure, the state of the charge (SOC) starts to decrease from an assumed 100% to 97.51% in the discharging period and then starts to increase during the charging mode. Finally, the battery DC power output is shown in Figure 32. The positive power represents the power injected to the AC side (utility) and the negative sign is used to represent the power injected into the battery.

The battery dynamic model is also integrated with a converter model which maintains the output power in a desired value. As an application, the battery storage system is utilized to decrease power ramp ratings of the PV plant output power generation. Therefore, an appropriate power request signal is modeled as an input for the power controller of the AC/DC converter. The converter AC voltage is measured from the AC terminal to calculate AC current. This current in turn is converted to DC side current, using a converter AC current exchange to DC current equation. Then, the battery dynamic model results of the DC voltage are used to calculate DC side power as well. Consequently, the AC power is achieved by converting DC side power considering the converter efficiency. Finally, this power is injected by the Battery Model to the utility. The left side of the Figure 28 shows this control block implementation on the Lithium-Ion Battery/Converter Model.

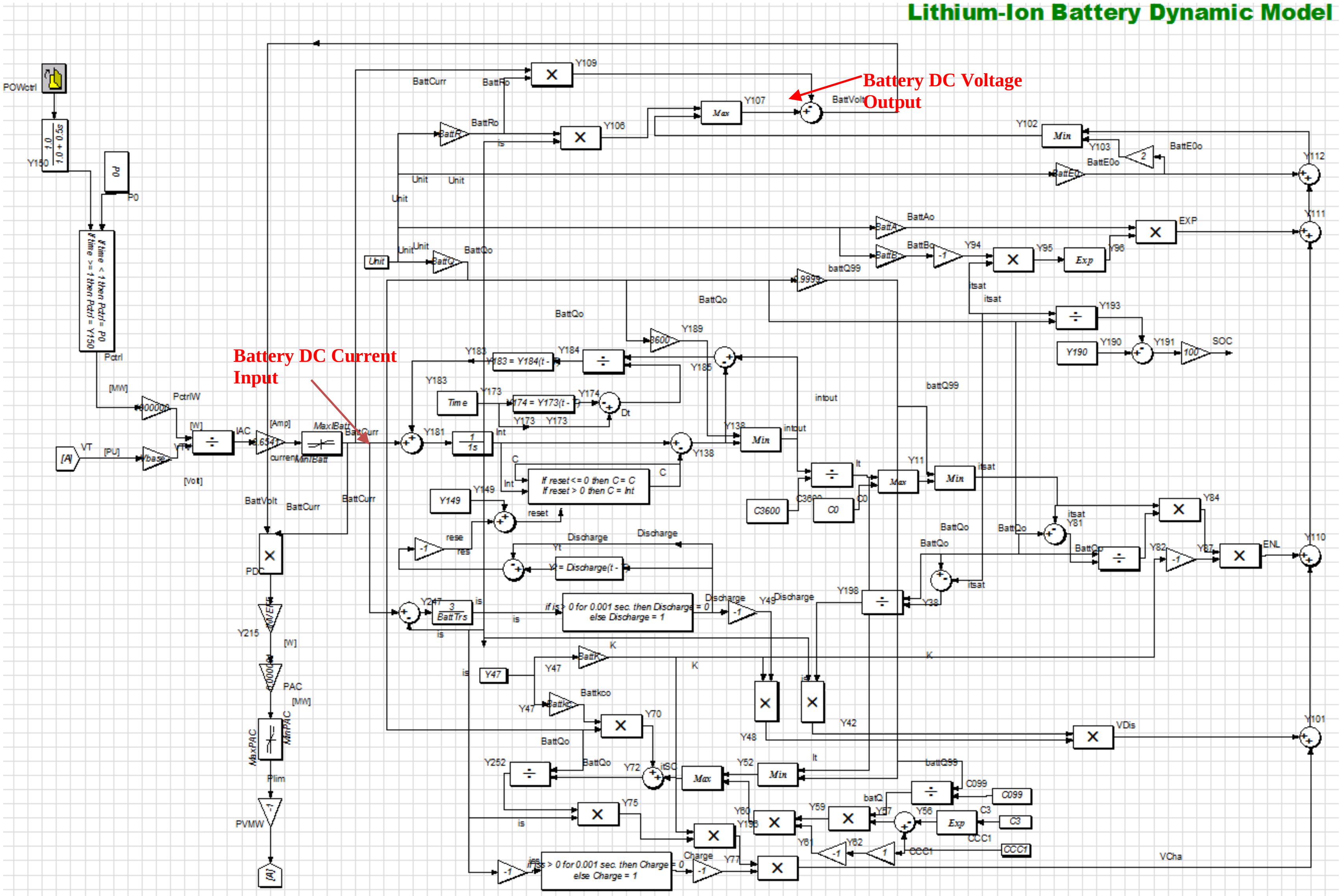

Battery DC Voltage Output

Battery DC Current Input

Figure 58 - Lithium-Ion Battery/Converter Control Model

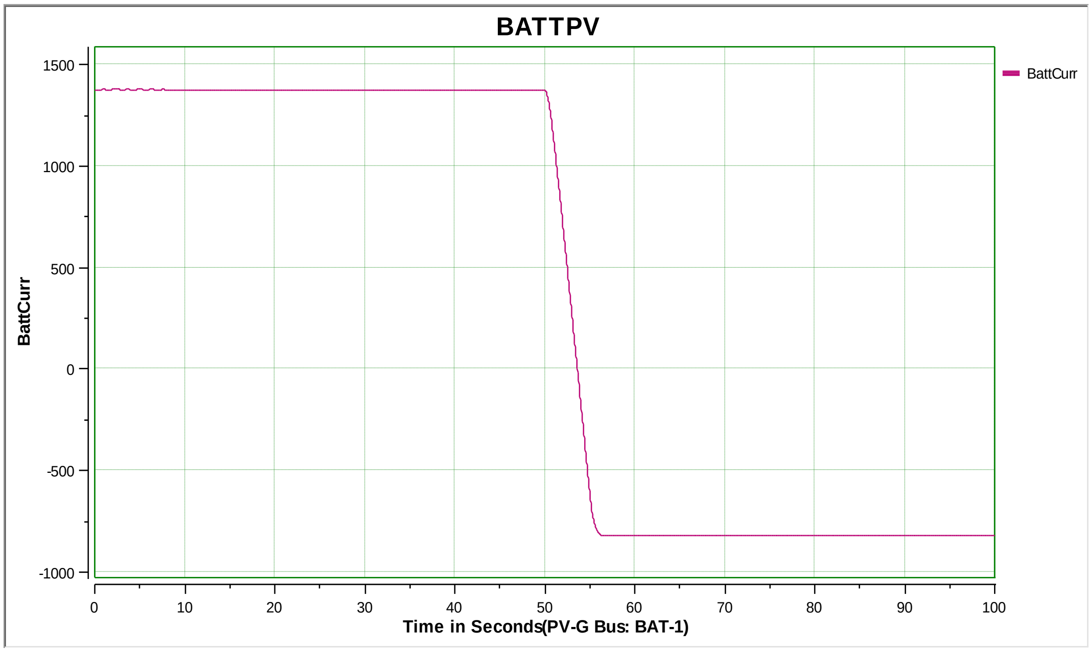

Figure 59 - Battery Storage DC Current

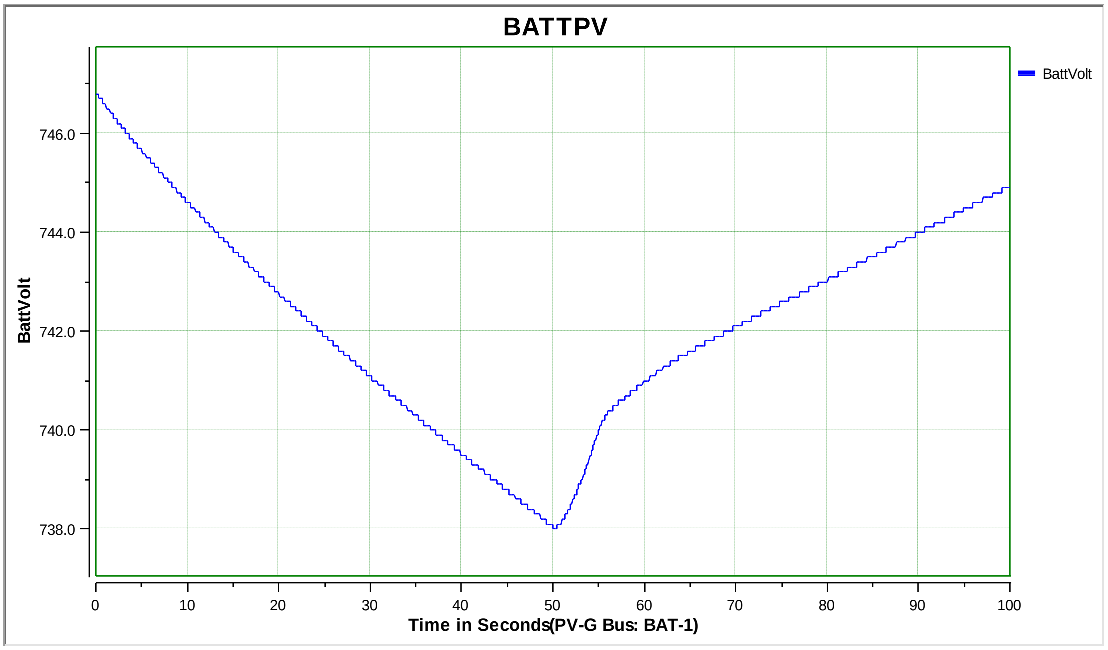

Figure 60 - Battery Storage DC Voltage

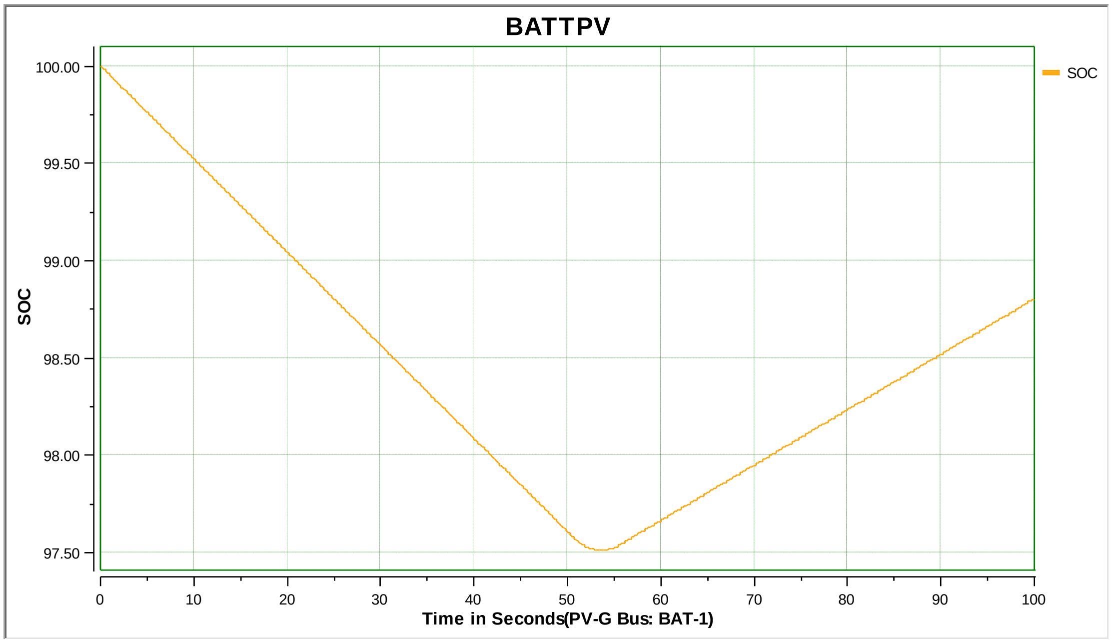

Figure 61 - Battery State of the Charge

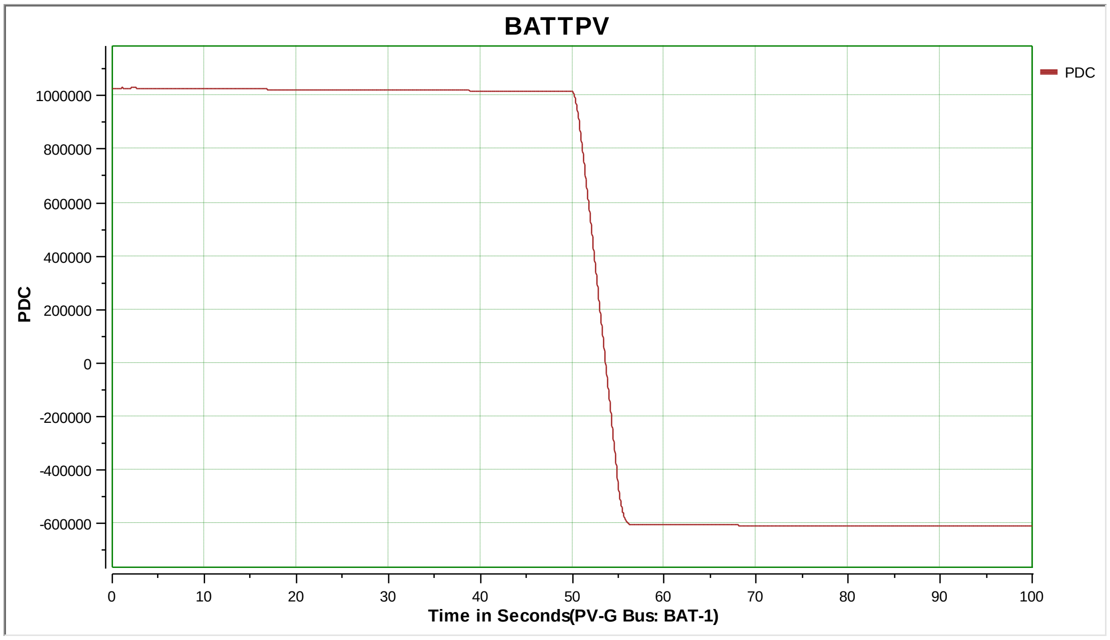

Figure 62 - Battery DC Power Output

6.5. Conversion of DesignBase Models into Other File Formats

There are multiple ways to transfer DesignBase models into different file formats and use the data in different software packages. In general, most available power system software packages have load flow modules and the load flow simulation presented here is possible in most packages. One exception is the interface with MATLAB through the Paladin ResearchLab module, which is not available in most commercial or off the shelf software applications.

The power flow data exchange is also possible via the IEEE common data format which has been a standard industry practice for decades. DesignBase can save the network data in IEEE common data format and other software applications can be used to import the data (if an import routine is available) or alternatively a network can be recreated based on the IEEE common data. In addition to this functionality, Power Analytics has developed a conversion routine that automatically transfers system data in OpenDSS. This process is explained in detail in Section 6.

A somewhat bigger challenge is transfer of dynamic data (control data) into other software applications. Most of the available power modeling software does not have the capability to perform this type of simulation, or the ability is limited to basic control functions. MATLAB/Simulink is typically the software of choice for control logic block diagrams; however it is generic and cannot be used to perform power system studies on a complex model. Nevertheless, researchers can design interfaces between MATLAB and commercial power system analysis software as is explained in this report. To that end, Power Analytics has replicated the general PV/Inverter model in Simulink as explained in Section 6.

6.6. Conversion to Open DSS

A conversion routine is created between DesignBase and OpenDSS. Any power system model created in DesignBase can be automatically converted to OpenDSS format by utilizing this tool. Figure 28 shows the interface for the conversion; the user has to choose the original DesignBase file and name the converted file.

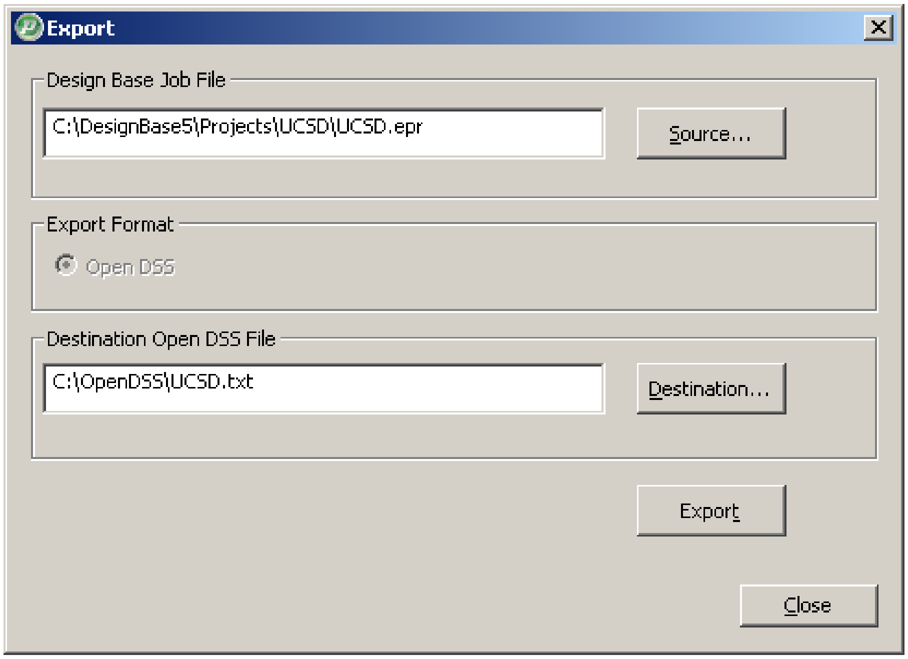

Design Base Job File: C:\DesignBase5\Projects\UCSD\UCSD.epr

Export Format: ● Open DSS

Destination Open DSS File: C:\OpenDSS\UCSD.txt

Figure 63 - OpenDSS Conversion

The rest of this section explains the limitations of the conversion and the format of the converted data.

The following are the limitations of the converted file because the functionality is very different between the DesignBase and OpenDSS software:

- This conversion only addresses power flow / short circuit data (i.e. system impedances). OpenDSS does not support complex control modeling as explained in Section 3. Power Analytics has developed an appropriate Simulink model to provide a comparison or validation with results matching the results obtained using DesignBase.

- OpenDSS does not support multiple scenarios. Only the first DesignBase scenario is converted in OpenDSS.

- DesignBase supports multiple temperatures (power flow temperature, short circuit temperature, impedance display temperature). Conversion to OpenDSS converts all resistances based on power flow temperature (typically this is 40^0C).

- OpenDSS supports only a single swing bus. Multiple swing buses are handled in the following way: only the first swing bus is converted to OpenDSS; every subsequent swing bus will be converted as PQ generator with P=Q=0 and will be commented out as shown below:
  // More than one swing bus detected; additional swing buses model as PQ buses with 0 injection and commented out:

```
// New generator.DBBusName Bus1=DBBusName kV=DBActualkV Model=1
kW=DBPG  Kvar=0
```

- If any equipment being converted is “opened” (e.g. open switch) in DesignBase, the following message will be provided:
  // Equipment “DBName” is opened in DesignBase. Please review OpenDSS data.

- In case any equipment used in DesignBase is not covered by the conversion routine (e.g. duplex reactor, zig-zag grounding, etc.) the following command line will appear in OpenDSS:
  // Equipment “DBName” is not covered with this conversion. Please enter it manually.

The following subsections show the conversion details for common power system elements.

Voltage Source:

The following DesignBase fields are used in conversion:

- Bus Name (DBBusName)
- System kV (DBSystemkV)
- Actual kV (DBActualkV)
- Voltage Angle (DBAngle)
- Max 3P MVA (DB3PMVA)
- Max LG MVA (DBLGPMVA)
- X/R1 (DBX/R1)
- X/R0 (DBX/R0)

Conversion syntax is:

```
New Circuit.DBBusName Bus1=DBBusName BasekV=DBSystemkV pu=(*) Angle= DBAngle
Frequency=(**) MVASC3= DB3PMVA MVASC1= DBLGMVA x1r1= DBX/R1 x0r0= DBX/R0
BaseFreq=(**)
```

(*) - pu is calculated as pu=DBActualkV/DBSystemkV
(**) - 60 for ANSI files, 50 for IEC files

Loads:

This section applies to all types of load and all types of motors available in DesignBase (load, mixed load, induction motor, synchronous motor, etc.).

The following DesignBase fields are used in conversion:

- Bus Name (DBBusName)
- Rated kV (DBRatedkV)
- kW & kVar (DBkW & DBkvar)
- Load Type (DBLoadType)

Conversion syntax is:

// Declare Loads
New Load.DBBusName Bus1=DBBusName kV=DBRatedkV kW=DBkW Kvar=DBkvar Model=(*)

(*) - If DBLoadType = constant kVA; Model=1
If DBLoadType = constant impedance; Model=2

Messages on unsupported DesignBase data:

- If "Reactive Power Compensation" is used as a function within a DesignBase load, the following message will be provided:

// "Reactive Power Compensation" is ignored. This function should be modeled manually.

- If DBLoadType = "constant current", the following message will be provided:

// Unsupported load type; converted to a constant kVA load.

- If DBLoadType = "functional load", the following message will be provided:

// Converted to a constant kVA load. Research Open DSS for instruction how to model ZIP loads;

Lines:

This applies to all types of feeders available in DesignBase (feeder, feeder in magnetic conduit, bus duct, transmission line, etc).

The following DesignBase fields are used in the conversion:

Branch Name	(DBBranchName)
From Bus	(DBFrom)
To Bus	(DBTo)
R+ X+ R0 X0	(DBR+ DBX+ DBR0 DBX0)
C1 C0	(DBC+ DBC0)
Cable Length	(DBLength)
Ampacity	(DBAmp)

Conversion syntax is:

// Declare Lines
New Line.DBBranchName Bus1=DBFrom Bus2=DBTo Length= DBLength/1000 R1=DBR+ X1=DBX+ R0=DBR0 X0=DBX0 C1=(*) C0=(*) Normamps=DBAmp BaseFreq=(**) Units=none

(*) - Capacitance is transferred in nF per unit length.
When DesignBase uses μF/1000', the value is multiplied by 2,000
When DesignBase uses mF/1000', the value is multiplied by 2,000,000

When DesignBase uses mMhos/1000’ the value is multiplied by 1,000,000/pi/f
(**) - For 60Hz files this step is omitted. For 50Hz files BaseFreq=50

Messages on unsupported DesignBase data:

- If DBLength = 0, the following message will be provided:
  // Per unit impedances used in DesignBase. Please review line data for line DBBranchName.

- If “mutual coupling” exists in DesignBase, the following message will be provided:

  // Mutual coupling used in DesignBase. Please review line data for line DBBranchName.

Transformers:

The following DesignBase fields are used in conversion:

○ Branch Name	(DBBranchName)	
○ From Bus	(DBFrom)	
○ To Bus	(DBTo)	
○ From Winding	(DBFromWind)	(e.g. delta, Y, etc.)
○ To Winding	(DBToWind)	
○ From Voltage	(DBFromV)	(nameplate voltages and not system voltages)
○ To Voltage	(DBToV)	
○ kVA Rating	(DBkVA)	
○ Primary Tap	(DBPTap)	
○ Secondary Tap	(DBSTap)	
○ R+%	(DBR+%)	
○ X+%	(DBX+%)	

Conversion syntax is:

```
//  Declare Transformers
New Transformer.DBBranchName Phases=3 Windings=2 XHL=DBX+%
~ wdg=1 bus=DBFrom Conn=DBFromWind(*) kV=DBFromV kVA=DBkVA %R=DBR+%/2
Tap=DBPTap
~ wdg=2 bus=DBTo Conn=DBToWind(*) kV=DBToV kVA=DBkVA %R=DBR+%/2
Tap=DBSTap
~ Basefreq=(**)
```

(*) - “Wye” or “Delta”
If winding is grounded through impedance, the following should be added to it:
rneut = grounding resistance in ohms
xneut = grounding reactance in ohms
If a winding is ungrounded, the following should be added to it: rneut = -10

(**) - For 60Hz files, omit this step. For 50Hz files, use BaseFreq=50

Generators:

Generators operating as swing buses are not considered here (see section Voltage Source).

The following DesignBase fields will be used in conversion:

Bus Name	(DBBusName)	
Generator Actual V	(DBGenAVolt)	
Generator Type	(DBGenType)	(PV or PQ)
PG	(DBPG)	
Max Q limit	(DBQMax)	(used only for PV type)
Min Q limit	(DBQMin)	(used only for PV type)
Desired Volt	(DBDesiredV)	(used only for PV type)
Max V	(DBVMax)	(used only for PQ type)
Min V	(DBVMin)	(used only for PQ type)
QG	(DBQG)	(used only for PQ type)
kVA Rating	(DBkVA)	
Grnd R & X	(DBGrR & DBGrX)	
%Xd” %Xd’ %Xd	(DBX” & DBX’ & DBX)	

Conversion Syntax for PV generators:

// Declare PV Generators
New generator.DBBusName Bus1=DBBusName kV=DBGenAVolt Model=3 kW=DBPG kVA=DBkVA Rneut=(*) Xneut=(*) Vpu=DBDesiredV Maxkvar=DBQMax Minkvar=DBQMin Xd=DBX Xdp=DBX’ Xdpp=DBX”

Conversion Syntax for PQ generators:

// Declare PQ Generators
New generator.DBBusName Bus1=DBBusName kV=DBGenAVolt Model=1 kW=DBPG Kvar=DBQG kVA= DBkVA Rneut=(*) Xneut=(*) Vminpu= DBVMin Vmaxpu=DBVMax Xd=DBX Xdp=DBX’ Xdpp=DBX”

(*) - For Solidly grounded generator this is omitted
For ungrounded generators this is set to -10
For generators grounded through impedance, this is set to DBGrR & DBGrX

Messages on unsupported DesginBase data:

- If “Load Connected to Generator Bus” ≠ 0, the following message will be provided:
  // “Load Connected to Bus” is ignored. This function should be modeled manually.

- If “Controlled Bus” ≠ “Generator bus”, the following message will be provided:

// “Control bus set to Generator bus”. Please research OpenDSS help on how to control a distant bus.

Switches, fuses, breakers, relays:

This applies to all types of switching devices in DesignBase: fuse, switch, circuit breaker (LV and HV) and relay. These devices are modeled as branches with finite impedances in DesignBase and represented as dummy lines in OpenDSS.

The following DesignBase fields will be used in conversion:

- Branch Name (DBBranchName)
- From Bus (DBFrom)
- To Bus (DBTo)
- R & X (DBR & DBX)
- Amp Rating (DBAmpRating)

Conversion syntax is:

```
//  Declare Dummy Lines – switching equipment is represented in DesignBase as branches with
// finite impedance. In OpenDSS this equipment is shown as dummy lines with the appropriate impedance
New Line.DBBranchName Bus1=DBFrom Bus2=DBTo Length=1 R1=DBR X1=DBX R0=DBR X0=DBX Normamps= DBAmpRating Units=none
```

6.7. Conversion to MATLAB/Simulink

In order to create an opportunity for further study and collaboration with other researchers, the dynamic model of a photovoltaic system is also implemented in MATLAB-Simulink software. The implemented model is shown n Figure 55 on the next page, and includes all the functions and logic presented in section 3.

As MATLAB Simulink is not designed for core power system studies (it is not capable of running different load flow algorithms and short circuit studies based on IEEE standards on the large and complex networks), we have implemented the dynamic control model with no power system interface. Connection of that model to OpenDSS or another software package is left for researchers interested in these studies.

The output of this dynamic model is the controlled active and reactive power. One can use the Simulink blocks to create a proper power source and connect it to his/her power system model inside of the power system toolbox MATLAB. Therefore, the best method for testing this model and verifying the results with DesignBase software is to use DesignBase closed loop (integrated power system-controller model) results as inputs for an open loop test (no power system interface) of the MATLAB-Simulink model. This procedure is depicted in following figure:

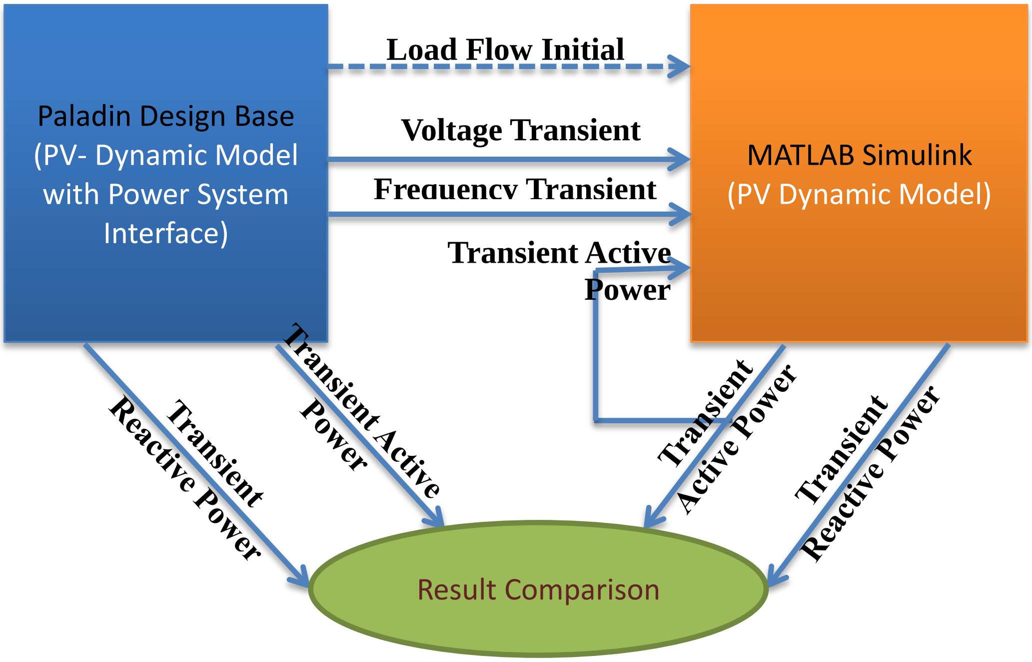

Figure 64 - Open loop testing of developed Simulink model

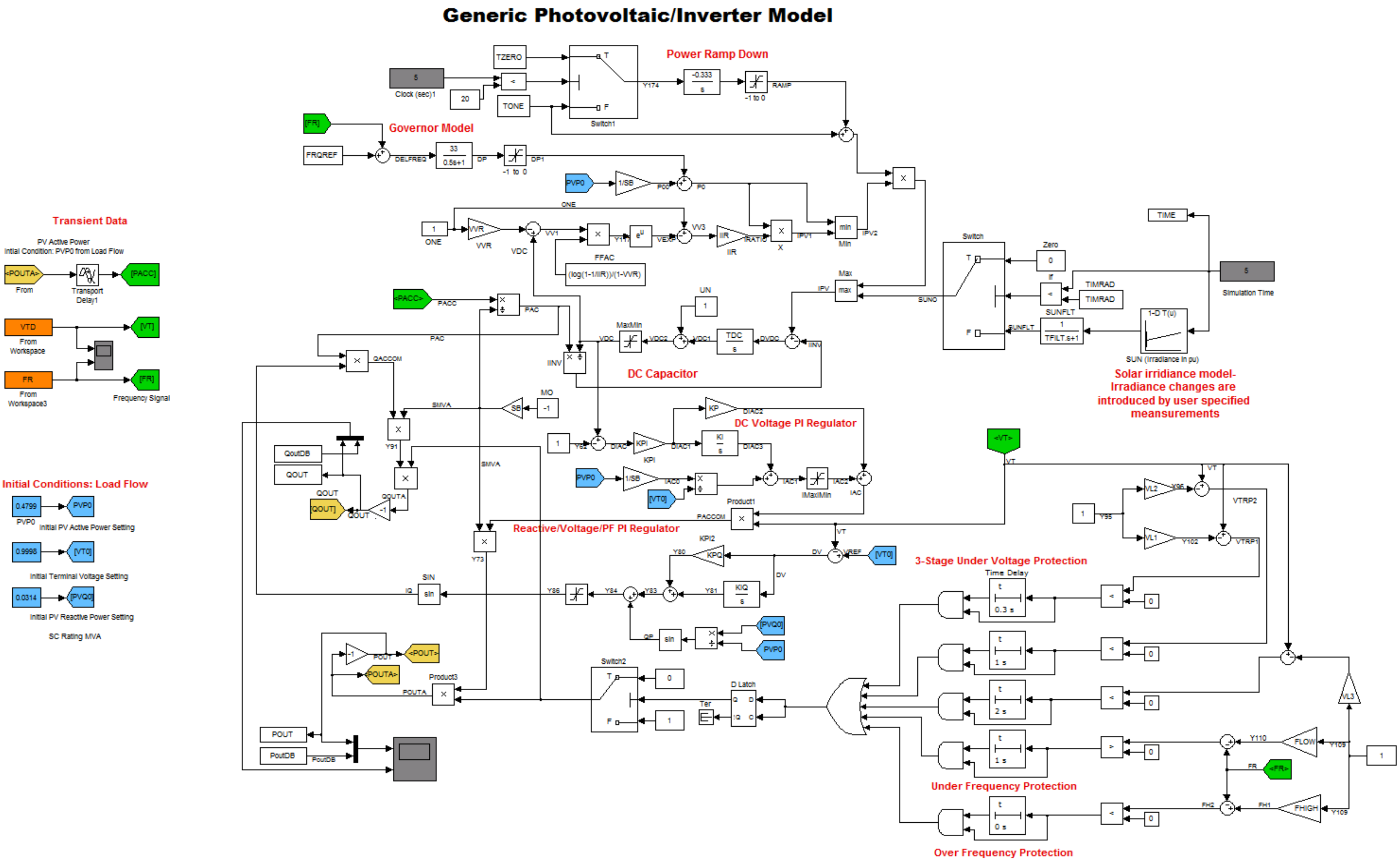

Figure 65 - Generic Model of PV/Inverter Developed in Simulink

As a test case, an SC event is considered on the PV bus in the DesignBase transient module and the voltage and frequency transient signals are transferred to the MATLAB Simulink model. Hence the closed loop behavior of the PV in DesignBase should be achieved by the open loop MATLAB simulation results. Finally the comparison between MATLAB Simulink and DesignBase is presented in the following figures. An SC fault event in the PV terminal bus for 0.3 sec duration is simulated and the models active and reactive power outputs are shown for result comparison. The models behaviors are identical. Therefore, the implemented MATLAB and DesignBase models are identical.

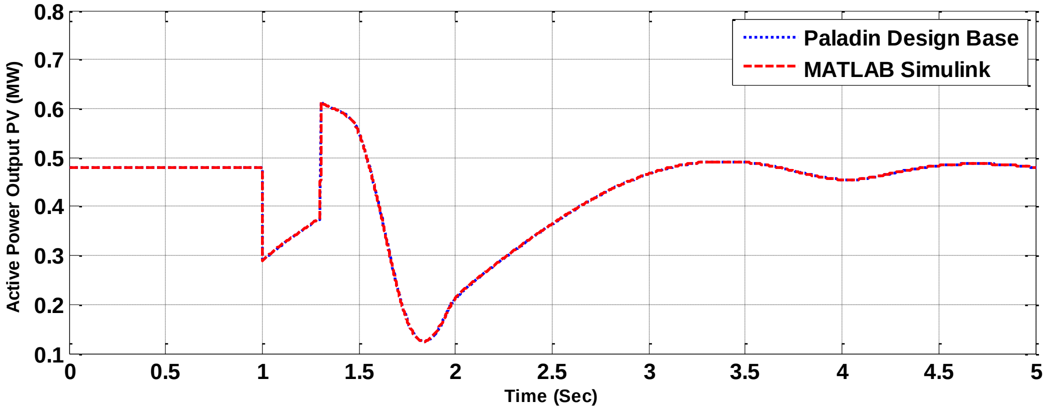

Figure 66 - DesignBase and MATLAB comparison – Active Power Output during the SC at PV bus

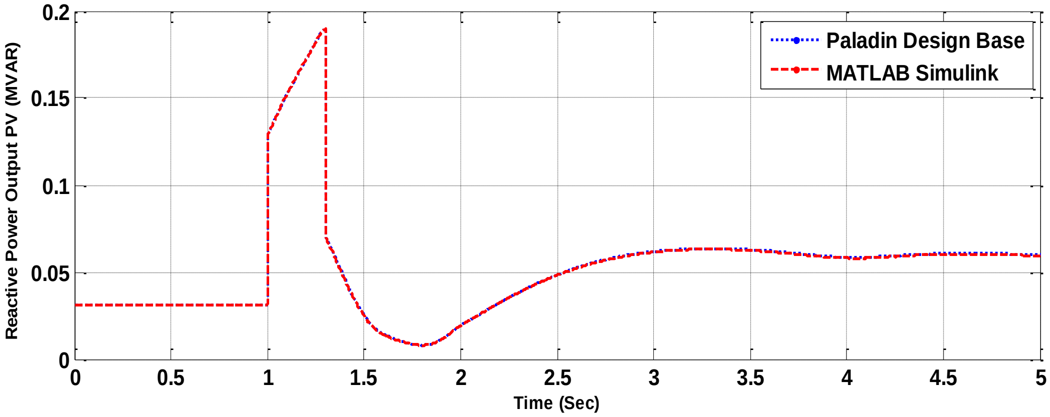

Figure 67 - DesignBase and MATLAB comparison – Reactive Power Output during the SC at PV bus

6.8. Benchmark Study for a use case 50 MW PV Power Plant

As we discussed in previous sections, two types of models are developed by Power Analytics to help in analysis and design of typical PV plants: a power flow model of the entire plant and the generic control models of the PV/Inverter and Battery/Converter.

The use case model of the PV Power Plant consists of 6 blocks, each containing 6×1.5 MW PV systems and one 1.1 MW battery (36 PVs and 6 batteries total). The 480V output of the PV and battery systems are stepped up by 42×36/0.48 kV transformers and all are brought to the same 36 kV bus. The voltage is increased once more by the 115/36 kV transformer and the plant is connected to the utility via a three mile-long transmission line. Expected system impedances (feeder size and lengths transformer impedances, etc.) are obtained from the practical network.

For the purpose of transient simulations the utility network is modeled as a set of swing buses (500MVA) and a load (100MW + 50 Mvar). Droop frequency control is assumed at the utility swing bus in order to be able to demonstrate the droop control feature of the PV plant. Generic controls models are developed for the PV/Inverter and PV/battery blocks. The controllers are explained in detail in the previous sections.

An example of the minimum requirements for interconnection of PV facilities to utility is listed below along with analysis results typically required for the interconnection agreement:

a) Low Voltage ride-through: all generation should remain online and be able to ride-through faults down to 0.0 per-unit or up to 600 ms.
b) Overvoltage ride-through: all generation should remain online and be able to ride-through overvoltage conditions specified by the following values:

Table 15. Overvoltage values

Overvoltage (pu)	Minimum time to remain online (seconds)
1.4 – 1.25	1
1.25 – 1.15	3
1.15 or lower	Indefinitely

c) Voltage regulation system: Constant voltage control shall be required.
d) Reactive Power Capability and Minimum Power Factor Requirements: The total power factor range shall be from 0.85 lagging to 0.85 leading. The +/- 0.90 power factor range should be dynamic and continuous.
e) Short Circuit Ratio (SCR)
f) Frequency ride through:
   - 57.5 – 61.5 Hz No tripping (continuous)
   - 61.5 – 62.5 Hz 30 sec
   - 56.5 – 57.5 Hz 10 sec
   - < 56.5 or > 62.5 Hz Instantaneous trip
g) Frequency response/regulation: the PV facility shall provide an immediate real power primary frequency response, proportional to frequency deviations from scheduled frequency, similar to governor response. The rate of real power response to frequency deviations shall be similar to or more responsive than the droop characteristic of 5% used by conventional generators.

h) Ramp rate control: The PV facility shall be able to control the rate of change of power output. A 10 % per minute rate (based on nameplate capacity) limitation shall be enforced.
i) Power Quality
j) Special Protection Schemes
k) Transient mathematical model

We are addressing these minimum technical requirements with proper modeling and simulation of the PV power plant using steady-state power flow calculations and dynamic transient simulation results.

6.8.1. Power Flow Calculations

This section summarizes the loss calculation in this typical PV system. These calculations are based on a power flow algorithm applied to the model as explained before and the irradiance / kW data is assumed to be real sun irradiance (obtained form UCSD) data which are separated into three categories: sunny, overcast and partly cloudy days. Representative sunny, partly cloudy and overcast days are chosen for further power flow analysis. Power flow analysis is performed for all three days in 5-second intervals. For each of these days two cases have been studied:

- Raw data (no curtailment and no ramping limitation)
- The best possible curtailment algorithm.

The first case is useful to quantify thermal losses in the system (RI2). The second case helps to quantify the minimum possible loss due to the optimal ramp-rate curtailment; in other words we quantify the energy that could not be captured in the battery due to its maximum charging rate limitation. It should be understood that the second case puts a lower bound on the losses, meaning the losses may be significantly higher depending on the goodness of the forecast and control algorithm.

In next sections, two simulations are performed to show the effectiveness of using a battery for decreasing the power ramp rating of the PV plant power output. The PV irradiance data for 300 seconds of a partly cloudy day is considered for every PV transient model as an input signal.

Case 1

Power flow calculations are performed using the raw data as presented in the previous section. The irradiance data is transferred into kW output based on the size of the plant and the efficiency of inverters. Battery and PV curtailment were not considered in this case. The goal of the simulations is to estimate the level of thermal losses in the power system – losses in transformers, cables and transmission lines between the inverters and the point of common coupling.

Based on the data summarized in following table, distribution system losses vary between 0.8 and 1.6%; the sunnier the day, the more current is injected in the system – and the losses are higher.

Table 16. Power Flow Results for the Case 1

Load Flow Study Results	Sunny Day	Overcast Day	Partly Cloudy Day
Daily Energy at PCC	348.786 MWh	145.518 MWh	275.553 MWh
Maximum Power at PCC	47.81 MW	49.042 MW	52.52 MW
Daily System Losses	5.575 (1.57) MWh (%)	1.191 (0.81) MWh (%)	4.025 (1.44) MWh (%)
Total Available Energy	354.361 MWh	146.709 MWh	279.578 MWh

Figures 57provides visualization of the results, showing the power at PCC (green area) and the losses (red area).

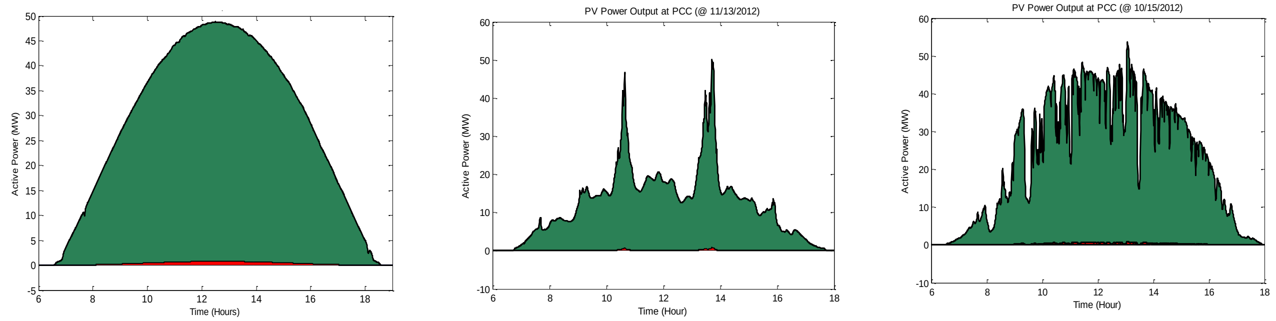

Figure 68 - Power and Losses for clear, overcast and partly cloudy days

Case 2
Power flow calculations are performed next utilizing both a curtailment algorithm and batteries. The storage battery is selected according to 10% of the PV plant nominal power. Six batteries with the following characteristics are used in the simulations:

Capacity (MWh- 30 min)	= 0.56 MWh
Max Discharge Power	= 1.1 MW
Max Charge Power	= 0.6 MW
Assumed Maximum Depth of Discharge	= 70% [784 KWh]
Assumed Maximum Charged	= 100% [1120 KWh]
Assumed Initial State of Charge	= 90% [1008 KWh]

The best possible curtailment algorithm is assumed by fitting the desired PV production in between the raw data, maintaining the slope of fitted data below ± 5MW/1min. An example of data fitting is shown below. The blue curve represents the expected raw power plant production in MW and the green curve represents the fitted data that will never exceed the ramping requirements. It should be understood that the above algorithm is the best possible and hard to implement in real-time: it assumes a perfect forecast and a perfect controller.

Figure 69 - PV Curtailment

It has also been assumed that during the period where extra energy is available (the blue curve is above the green curve), the energy is stored in the battery with the maximum charging power being 0.6 MW. When the additional energy is needed (the blue curve is below the green curve), the battery has been discharged with the maximum discharging power being 1.1 MW. No case is observed (within these 3 days) where the battery has reached the maximum discharge limit; several cases have been observed where the battery has reached its maximum charging limit. The latter case contributes to the increase in system losses as extra sun energy was available but could not be stored.

Results of the simulations are presented in the following table. As expected no changes were observed for the sunny days as no curtailment was necessary. Increased level of losses on other days is attributed to the period where more energy was available than could have been stored. However, this increase is very small due to the curtailment algorithm applied.

Table 17. Power Flow Results for the Case 2

Load Flow Study Results	Sunny Day	Overcast Day	Partly Cloudy Day

Daily Energy at PCC	348.786 MWh	145.611 MWh	274.704 MWh
Maximum Power at PCC	47.81 MW	48.9 MW	52.6 MW
Daily System Losses	5.575 (1.57) MWh (%)	1.194 (0.81) MWh (%)	4.039 (1.44) MWh (%)
Daily Battery Usage	0	+ 0.076 MWh	-0.799 MWh
Maximum Battery Power	0	[-3.77, 4.3] MW	[-3.6, 6] MW
Dissipated Sun Energy (not stored)	0	0.02 (0.013) MWh (%)	0.036 (0.012) MWh (%)
Total Available Energy	354.361 MWh	146.709 MWh	279.578 MWh

The following pictures provide the visualization of the results.

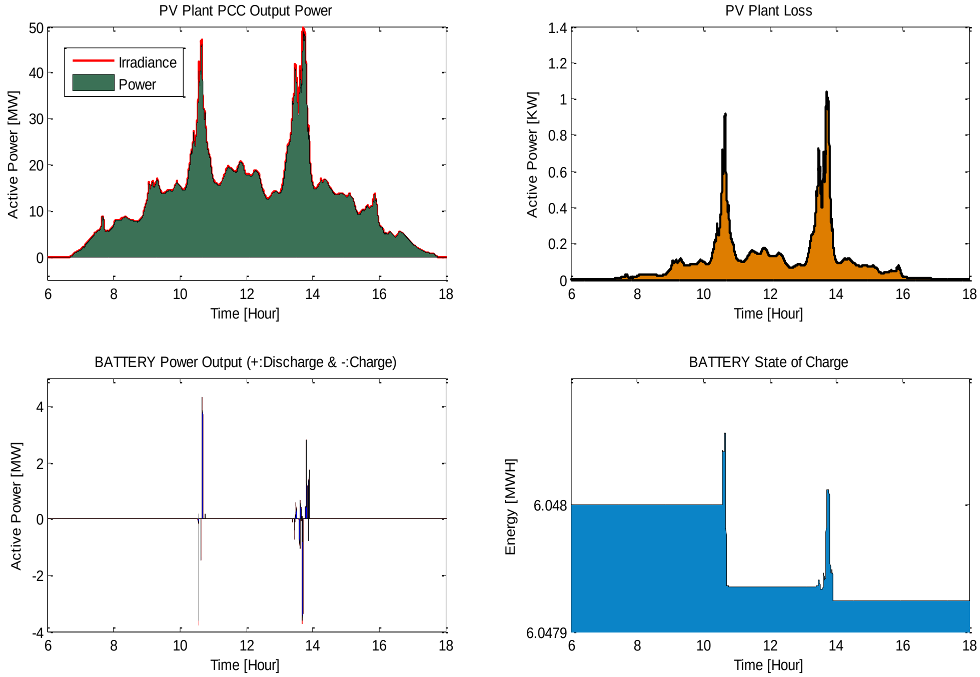

Figure 70 - Plant Output and Loss, Battery Output and Loss for Overcast Day

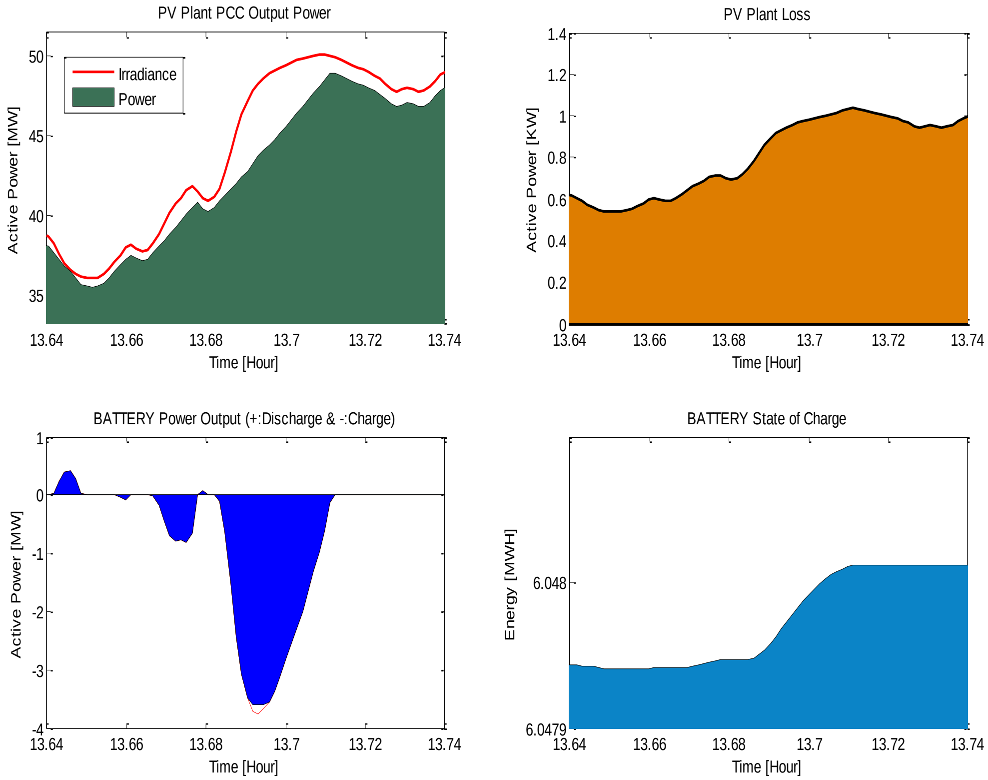

Figure 71 - Overcast Day Zoomed In

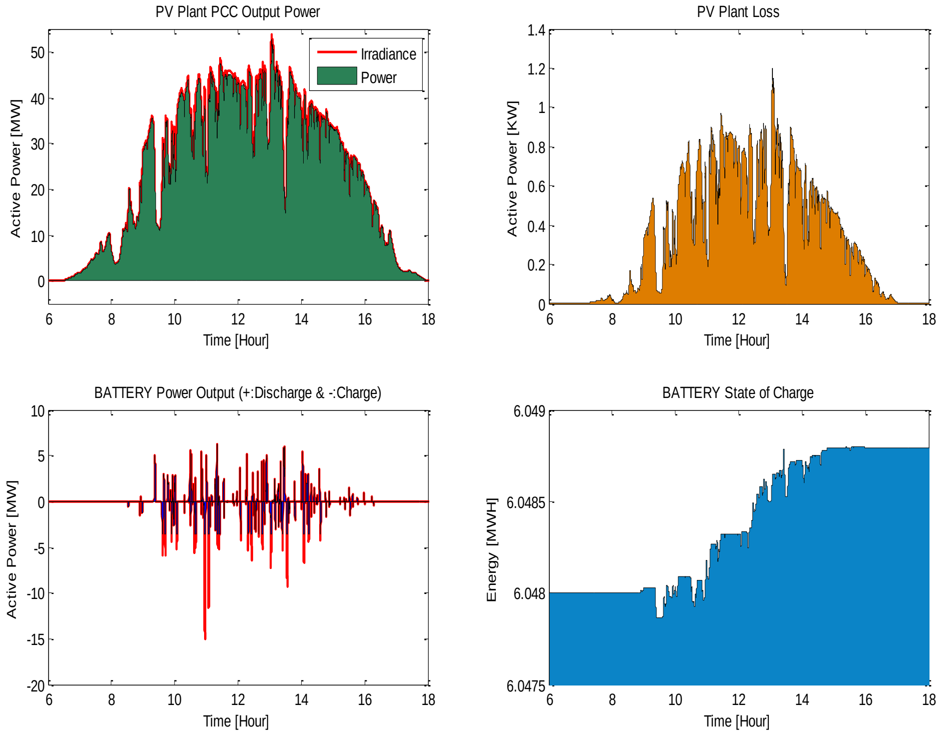

Figure 72 - Plant Output and Loss, Battery Output and Loss for Partly Cloudy Day

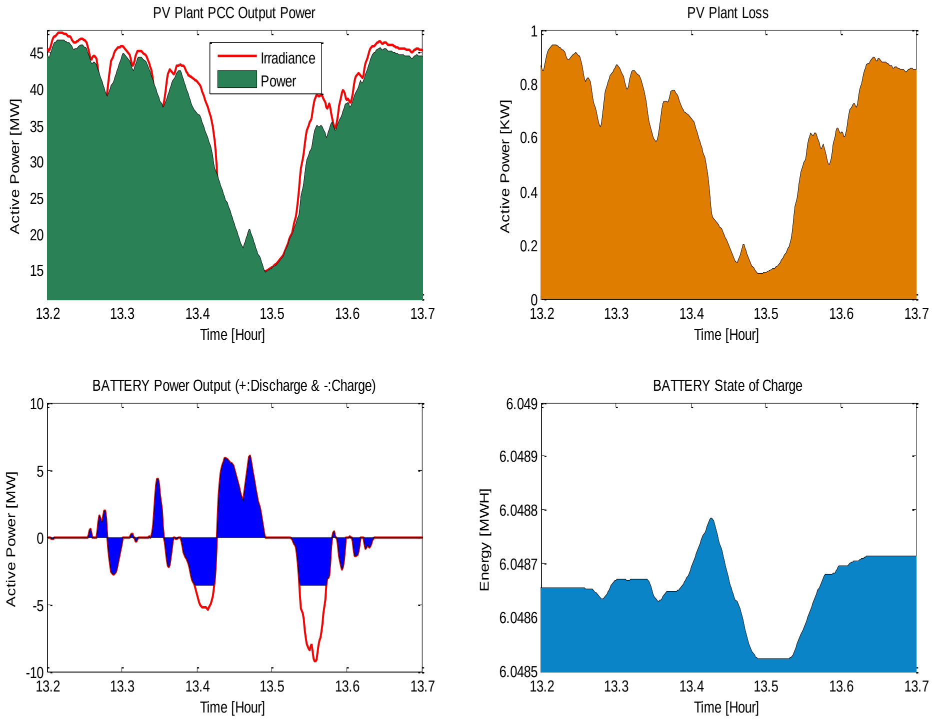

Figure 73 - Partly Cloudy Day Zoomed In

6.8.2. Transient Stability Studies

Multiple transient stability studies are performed to demonstrate the capability of the system to satisfy a utility's minimum technical requirements (MTR).

The model considered here is not an as-built power system model, and does not consider models of the particular PV, battery, inverter and controller. The simulations also do not consider a faulty weather forecast, all the possible weather patterns, etc. These types of simulations will be possible after the particular equipment is chosen, the plant layout and rating is finalized and more information on the weather forecast becomes available.

The simulations shown in this section are based on generic PV/inverter and battery/inverter models developed by Power Analytics. The models and power system are explained in the previous sections.

The model explained above had to be enhanced to include the following control functionality required by utility MTRs:

- Frequency droop controller ("governor")
- Power ramp down and rate limiter
- Tuning of the parameters of the previous model

The final PV/Inverter control model is given in Figure 8.0. The additions to the model do not represent control logic by any particular manufacturer but they do include basic control circuits developed by Power Analytics. Power Analytics expects that commercial inverter controllers will have the level of sophistication at or beyond the level presented here.

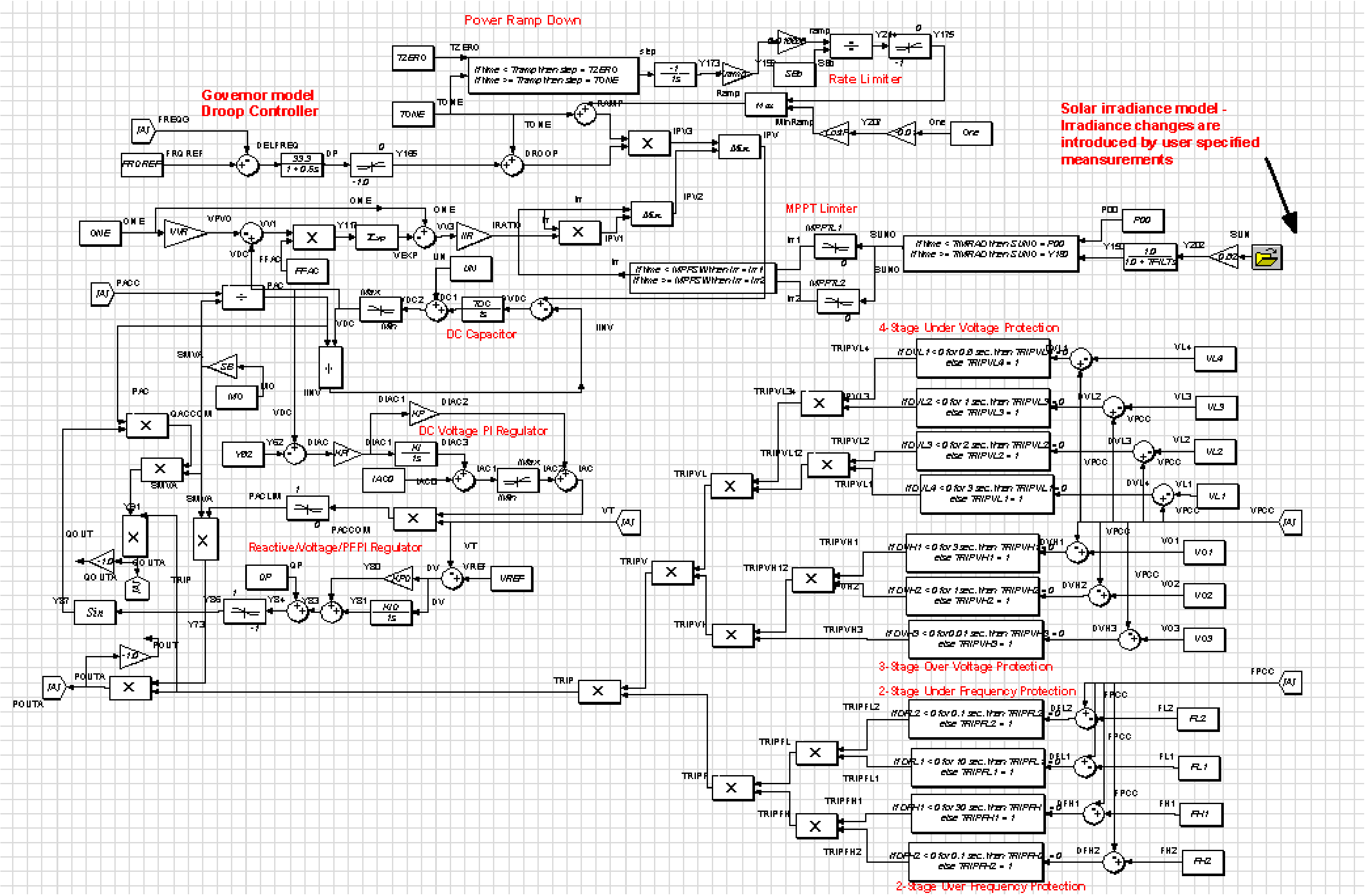

Figure 74 - Generic PV/Inverter Control Model

6.8.3. Frequency Response and Frequency Ride-Through

Compliance with these utility requirements is used to demonstrate the following simulations:

Over-frequency Instantaneous trip
Based on most utilities requirements the plant should trip instantaneously if the frequency exceeds 62.5 Hz. The following simulation demonstrates the capability. The frequency at PCC is increased by dropping 120 MW load at t = 10 sec. At t=14.8 sec the PCC frequency goes above 62.5 Hz and the trip signal takes out all the PV systems. The MW output of the PV system goes to zero even before the trip signal as the frequency droop control was faster than the protection. Following the frequency event, the 120MW load is switched on and the frequency is stabilized at PCC; the frequency is below 60 Hz as all the PV systems are out.

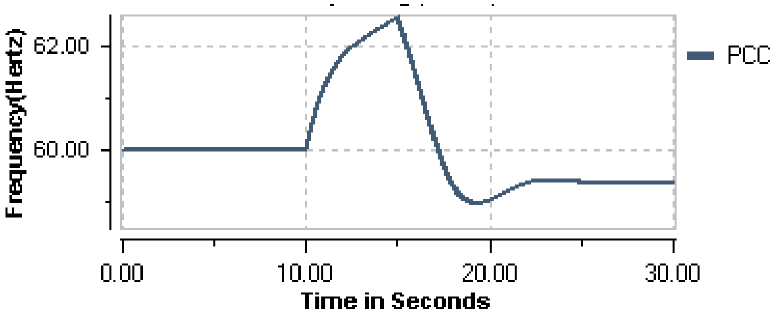

Figure 75 - PCC Frequency

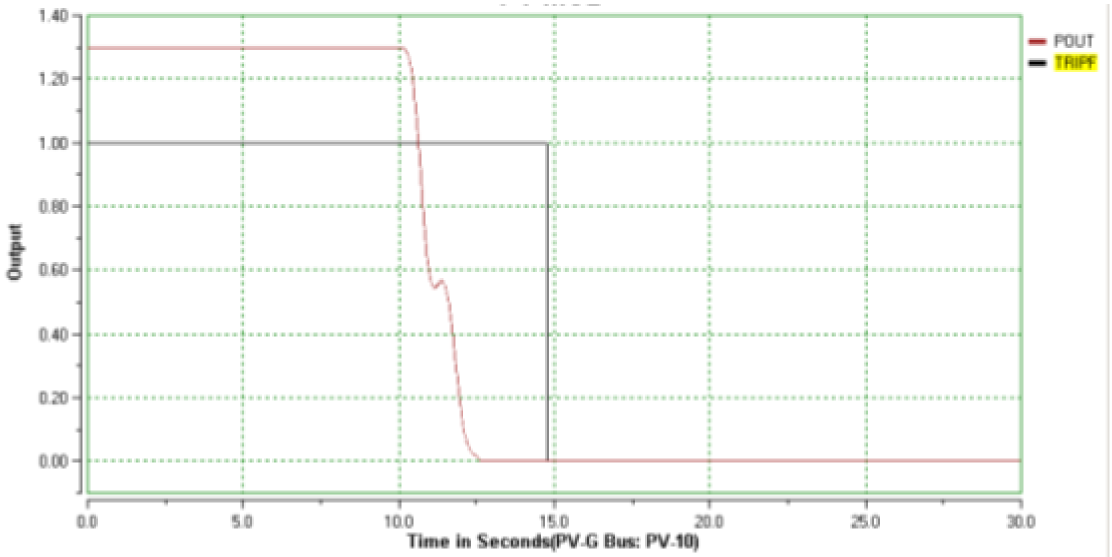

Figure 76 - MW Output and Trip Signal at PV/Inverter

Under-frequency Instantaneous trip:

Based on MTR requirements the plant should trip instantaneously if the frequency drops below 56.5 Hz. The next simulation demonstrates this capability. The frequency at PCC is decreased by adding 200 MW load at t = 10 sec. As the PCC frequency goes below 56.5 Hz the trip signal takes out all the PV systems. As the system was already working at the maximum power point, the inverter was not able to increase MW production in an attempt to regulate frequency.

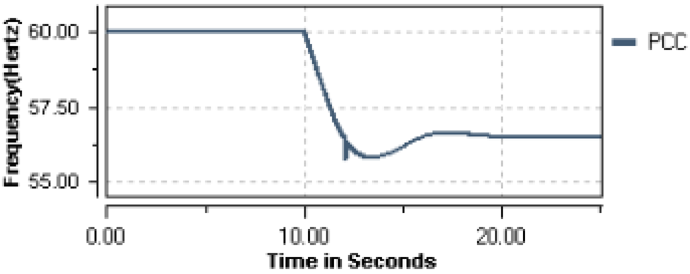

Figure 77 - PCC Frequency

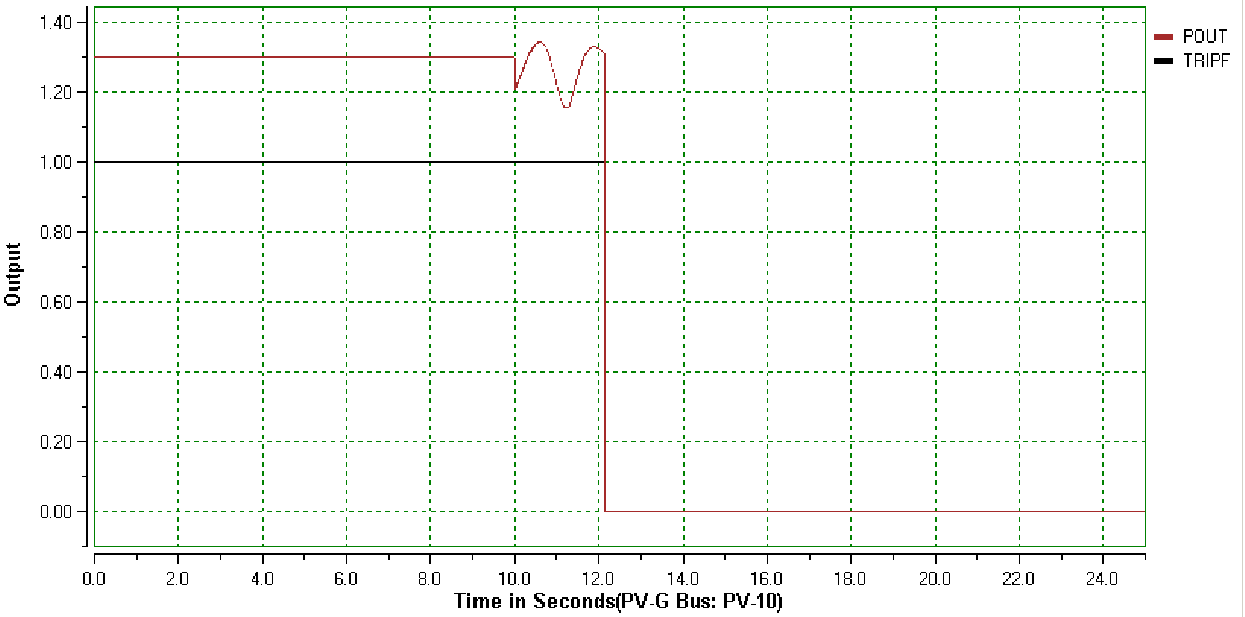

Figure 78 - MW Output and Trip Signal at PV/Inverter

Over-frequency Delayed trip:

Based on MTR the plant should trip after 30 seconds if the frequency stays between 61.5 and 62.5 Hz. The following simulation demonstrates this capability. The frequency at PCC is increased by dropping load at t = 10 sec. At t =12 sec the PCC frequency goes above 61.5 Hz and at t = 42 sec the trip signal takes out all the PV systems.

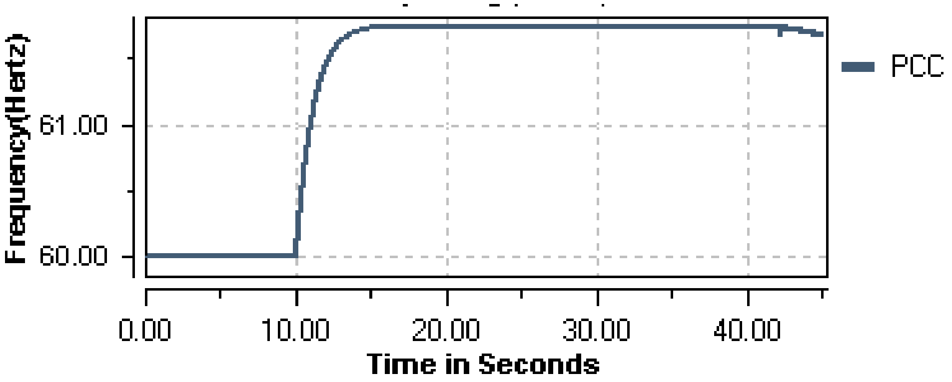

Figure 79 - PCC Frequency

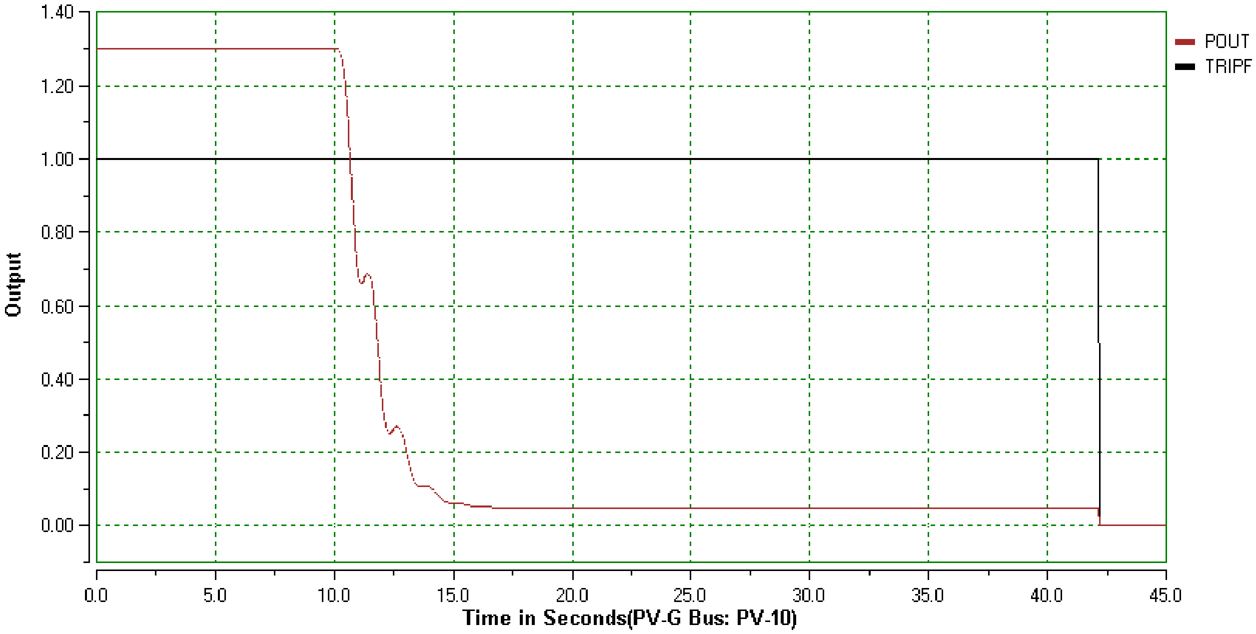

Figure 80 - MW Output and Trip Signal at PV/Inverter

Under-frequency Delayed trip:

Based on MTR the plant should trip after 10 seconds if the frequency stays between 56.5 and 57.5 Hz. The following simulation demonstrates this capability. The frequency at PCC drops below 57.5 Hz at t = 11.5 sec but recovers above 57.5 sec at t = 15.5 sec. Since the event lasted less than 10 seconds no trip has been initiated. At t =18.3 sec the PCC frequency again goes below 57.5 Hz and stays there over 10 seconds. Consequently at t = 28.3 sec the trip signal takes out all the PV systems.

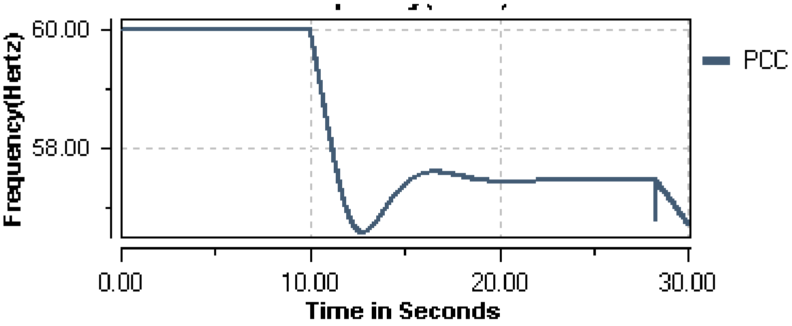

Figure 81 - PCC Frequency

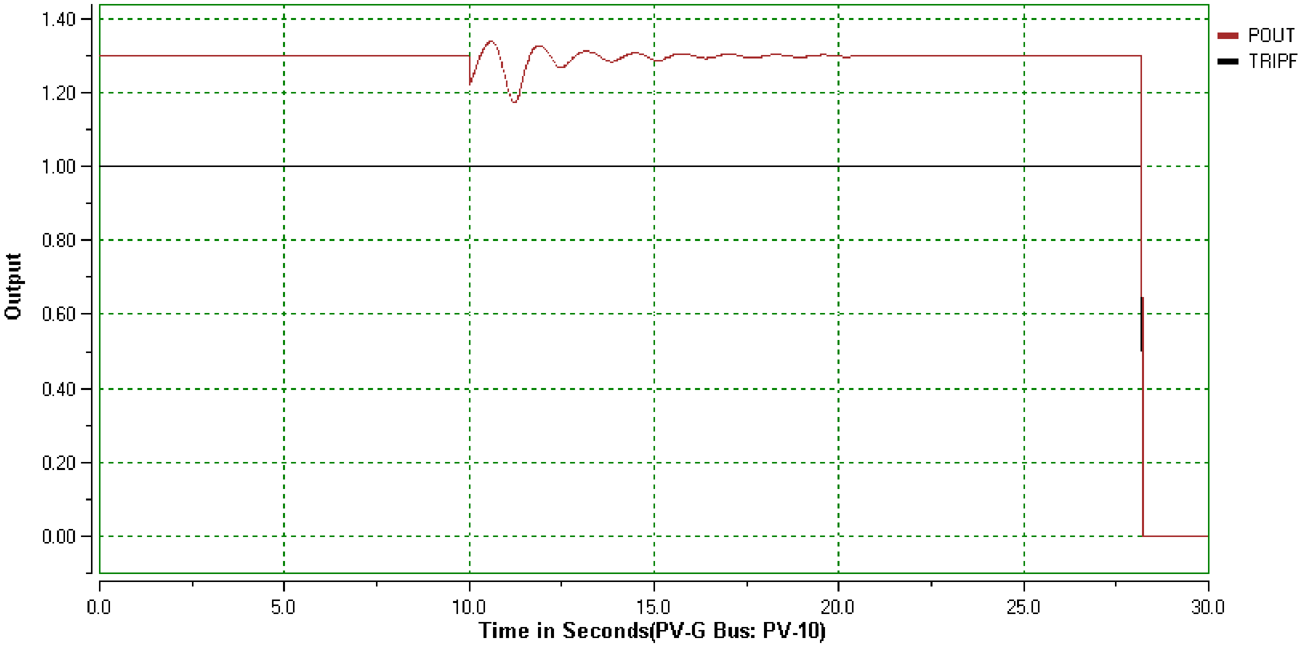

Figure 82 - MW Output and Trip Signal at PV/Inverter

Frequency Response:

Based on MTR the plant should provide an immediate real power frequency response proportional to the frequency deviation and similar to governor response. The following simulations demonstrate the capability.

Figures 72 and 73 show the event caused by dropping 30% of the load in the system. The frequency is regulated by the droop controller at all inverters and by the assumed droop controller at the utility bus. The controller brings the PV away from the maximum power point and hence reduces the active power injected in the system. Table 13 demonstrates the required droop response for the range of frequency events.

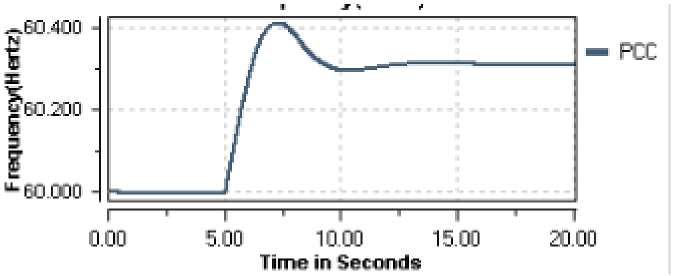

Figure 83 - PCC Frequency

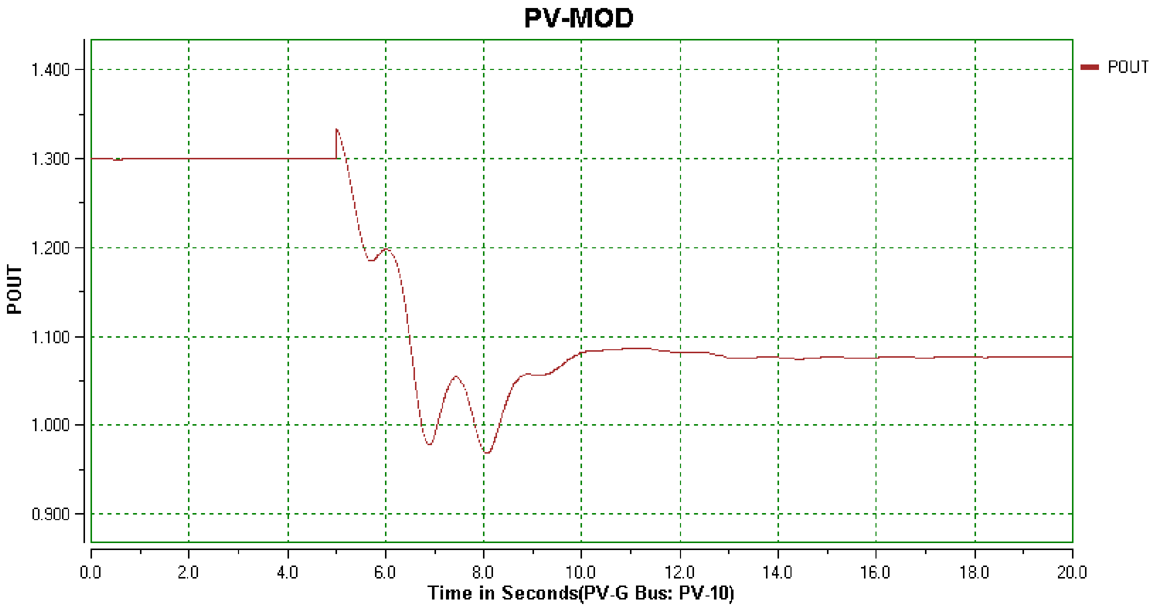

Figure 84 - MW Output of PV/Inverter

Table 18. Frequency Regulation

Load Shedding Percentage [%]	Frequency (Hz)		Utility Power [MW]		PV Plant Power [MW]		Freq. Deviation Δf [Hz]	Utility Power Share %	PV Plant Power Share %
	Before	After	Before	After	Before	After			
10	59.99	60.10	54.2	46.8	45.9	43.3	0.11	74	26
20	59.99	60.21	54.2	39.5	45.9	40.7	0.22	73.8	26.2
30	59.99	60.31	54.2	32.3	45.9	38	0.32	73.4	26.6
40	59.99	60.41	54.2	24.8	45.9	35.4	0.42	73.68	26.32
50	59.99	60.52	54.2	17.5	45.9	32.7	0.53	73.5	26.5
60	59.99	60.62	54.2	10.1	45.9	30.1	0.63	73.6	26.4
70	59.99	60.73	54.2	2.8	45.9	27.4	0.74	73.53	26.46

Figures 74 and 75 demonstrate the capability of the system to regulate under-frequency events if the PVs are kept away from the maximum power point. In this simulation frequency is reduced by bringing back 20% of the load that caused the PV plant to its increase power output.

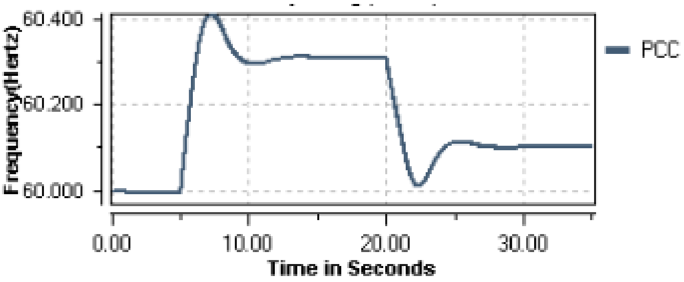

Figure 85 - PCC Frequency

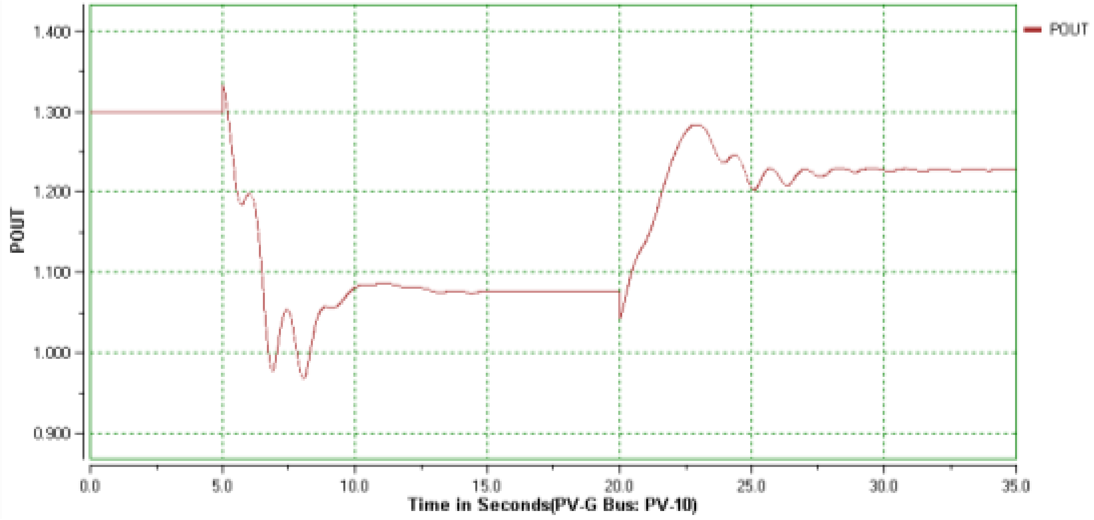

Figure 86 - MW Output of PV/Inverter

6.8.4. Voltage Regulation and Voltage Ride-Through

Compliance with these MTRs is demonstrated by the following simulations:

Overvoltage Instantaneous trip:

Based on MTR the plant should trip instantaneously if the voltage exceeds 1.4 pu. The following simulation demonstrates this capability. The voltage at PCC is increased by introducing a large capacitive load and the PV systems are disconnected instantaneously.

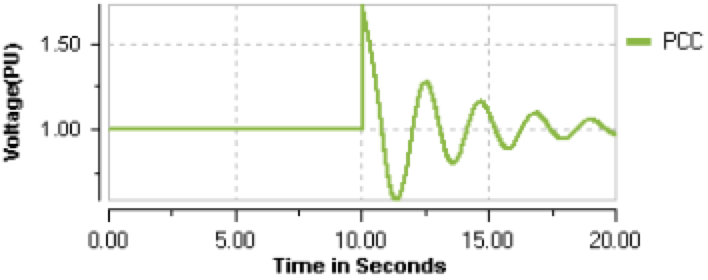

Figure 87 - PCC Voltage

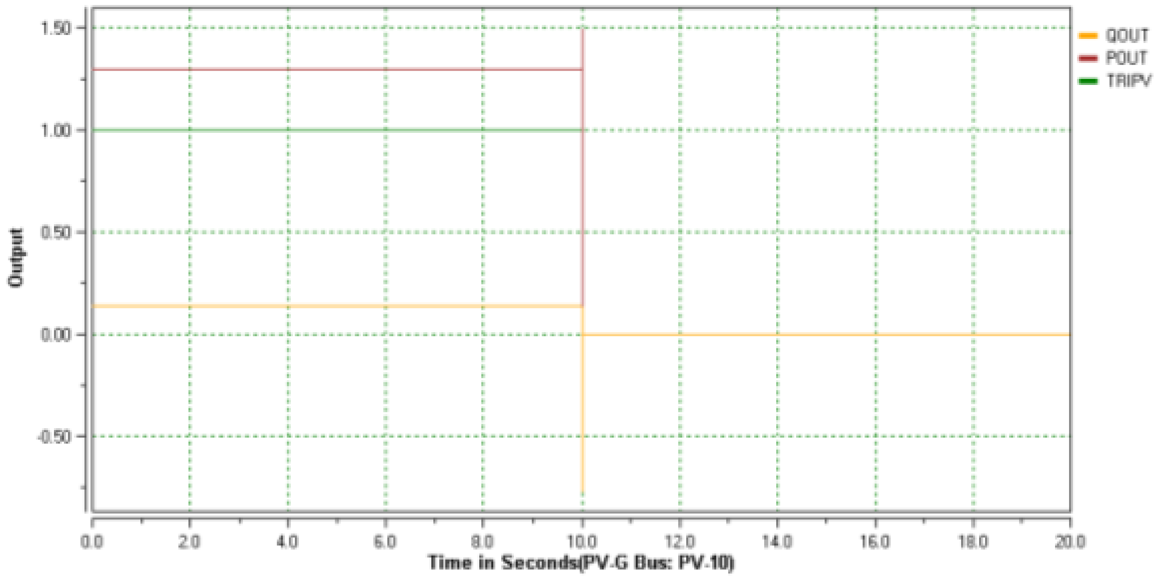

Figure 88 - MW, Mvar and Trip Signal at PV/Inverter

Overvoltage delayed trip:

Based on MTR the plant should trip after 3 seconds if overvoltage between 1.15 and 1.25 pu is observed; or, it should trip after 1 second for overvoltage between 1.25 and 1.4 pu. The following simulations demonstrate the capability. Figures 78 and 79 show a 3-second delayed trip; at t = 10.8 sec voltage at PCC goes above 1.15 pu and PV/Inverters are tripped at t = 13.8 sec. Figures 82 and 83 show a 1-second delayed trip.

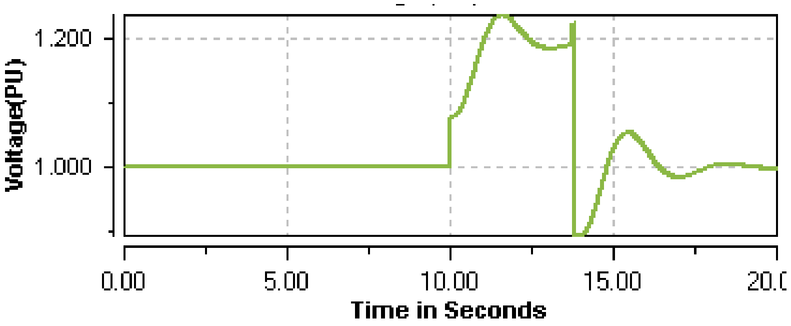

Figure 89 - PCC Voltage

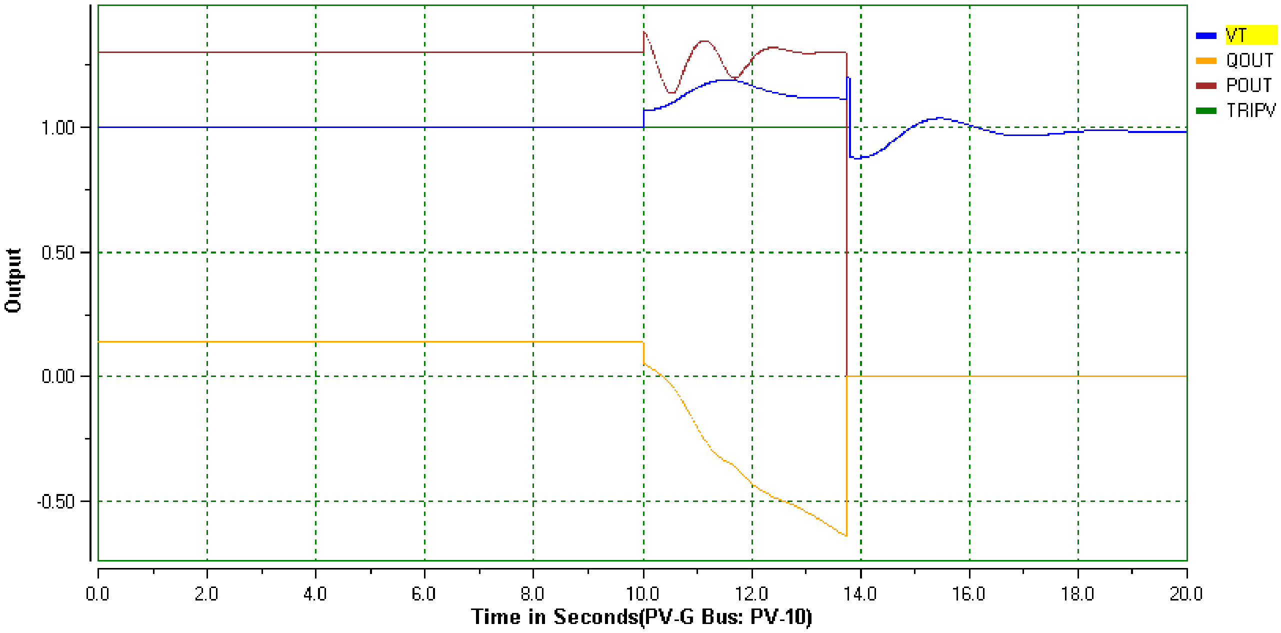

Figure 90 - MW, MVar, V_T and Trip Signal at PV/Inverter

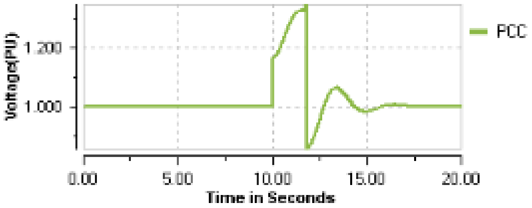

Figure 91 - PCC Voltage

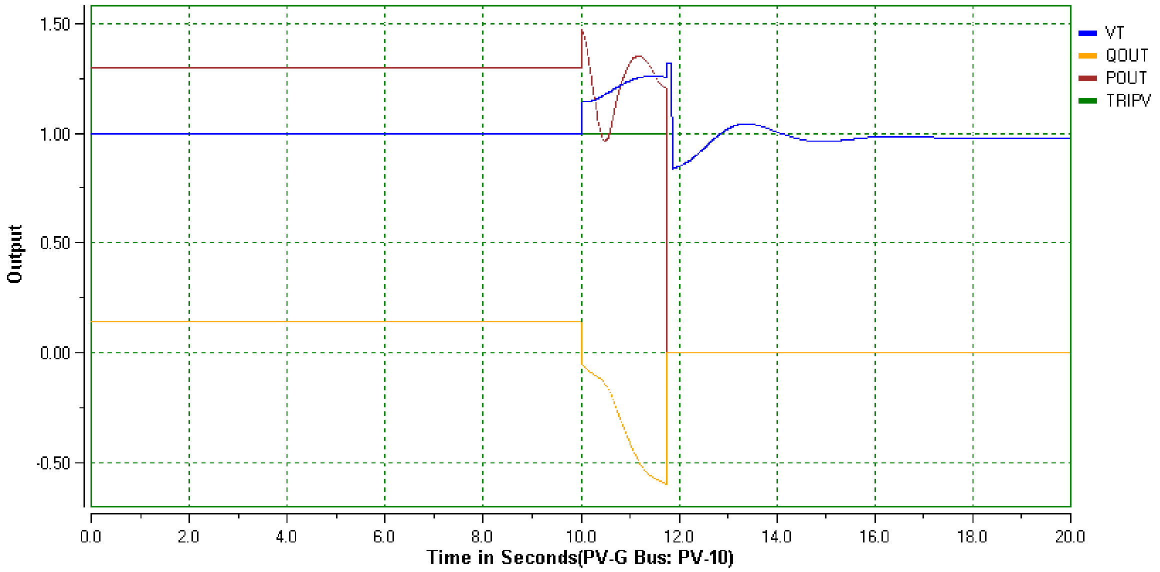

Figure 92 - MW, Mvar, V_T and Trip Signal at PV/Inverter

Under-voltage delayed trip:

The utility requires continuous voltage ride through the curve which is modeled and verified as four step V-t function. Figures 82 through 84 show tripping the plant at V<0.1pu after 600ms, at V<0.225pu after 1s, at V<0.53pu after 2s and V<0.85pu after 3s. Higher resolution is certainly possible and will be verified when the particular inverter is selected.

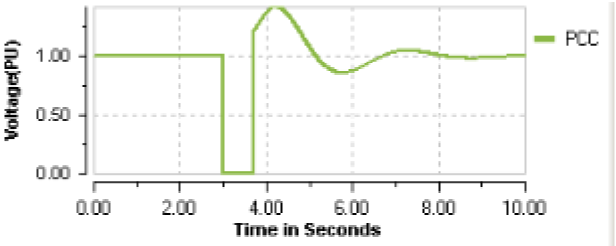

Figure 93 - PCC Voltage – at 3s goes to 0

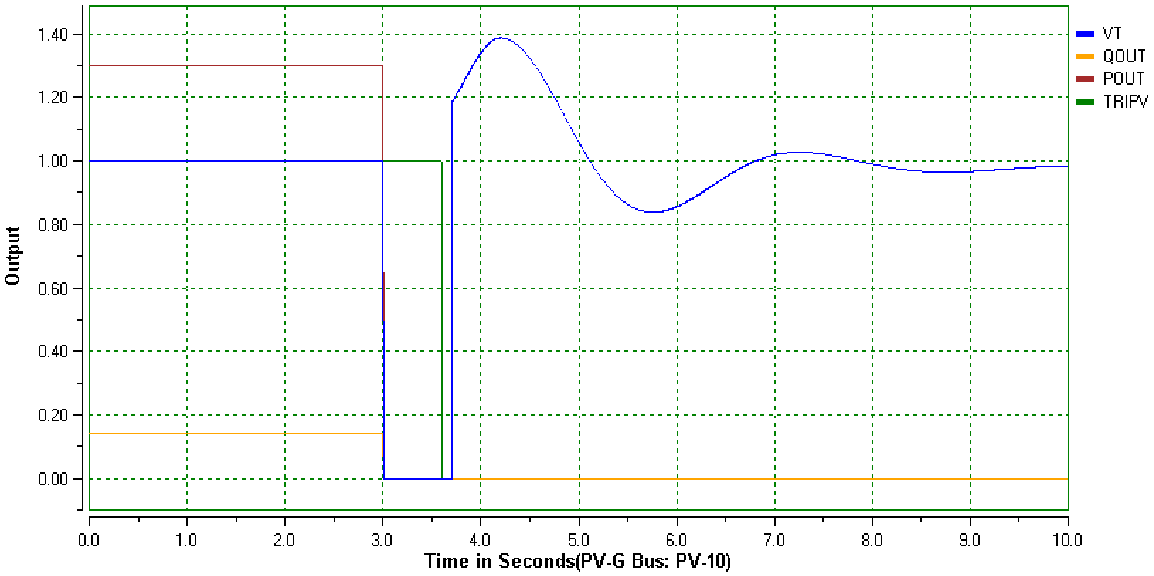

Figure 94 - MW, Mvar, V_T and Trip Signal at PV/Inverter (trip after 0.6 second)

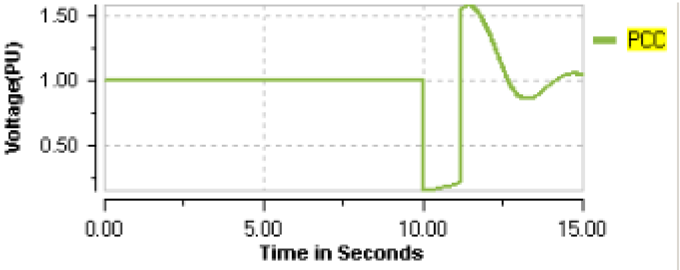

Figure 95 - PCC Voltage – at 10s goes below 0.225 pu

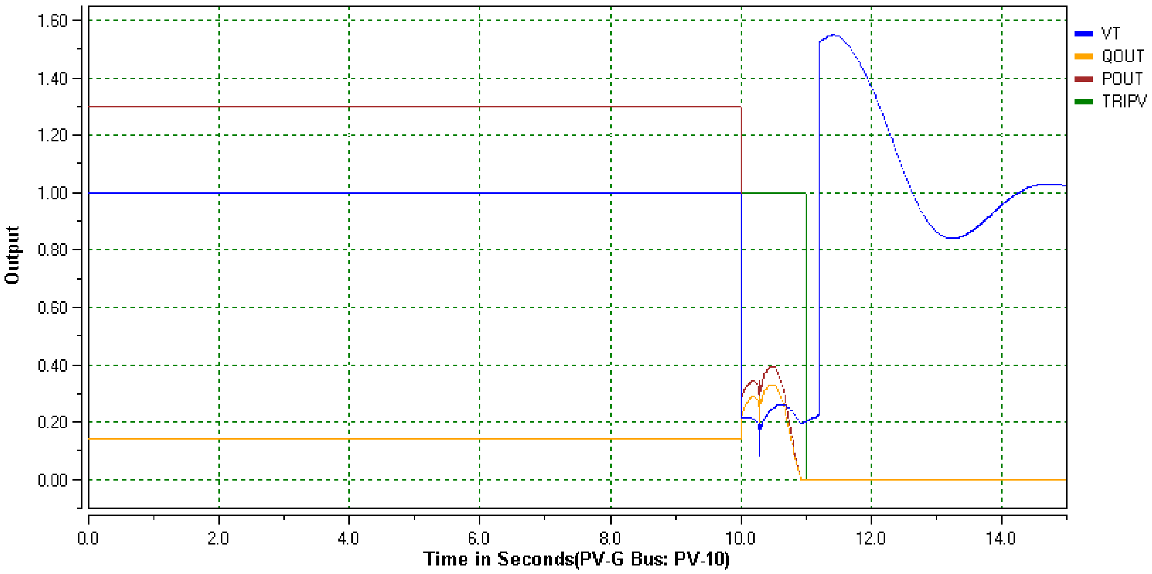

Figure 96 - MW, Mvar, V_T and Trip Signal at PV/Inverter (trip after 1 second)

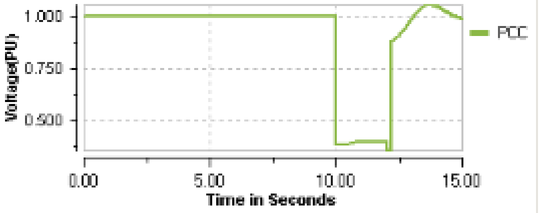

Figure 97 - PCC Voltage – at 10s goes below 0.53 pu

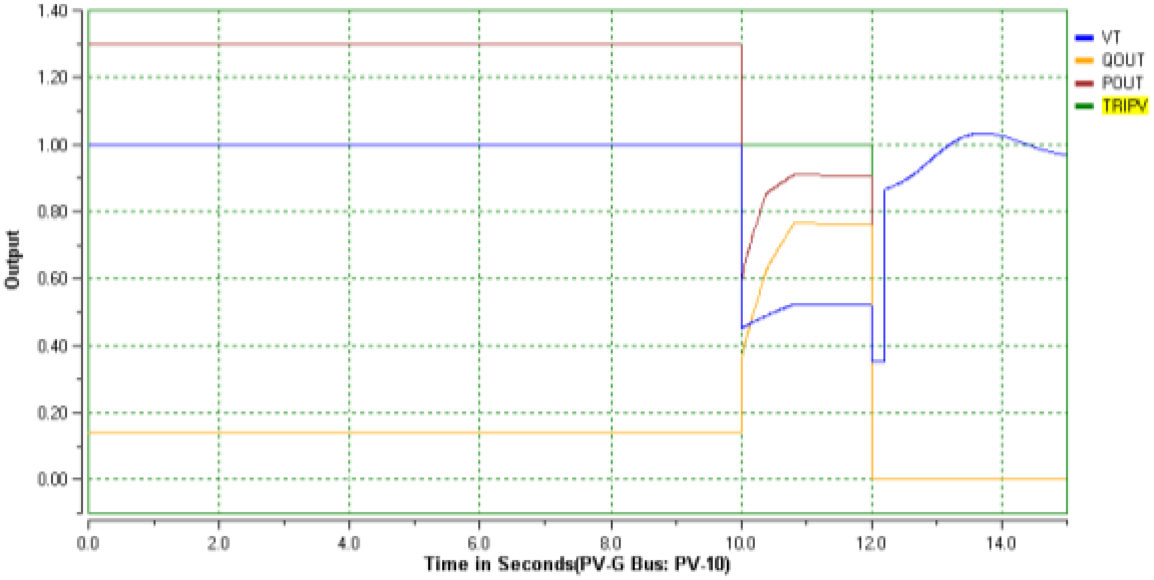

Figure 98 - MW, Mvar, V_T and Trip Signal at PV/Inverter (trip after 2 seconds)

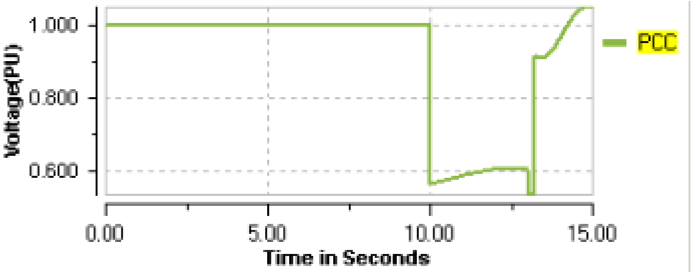

Figure 99 - PCC Voltage – at 10s goes below 0.85 pu

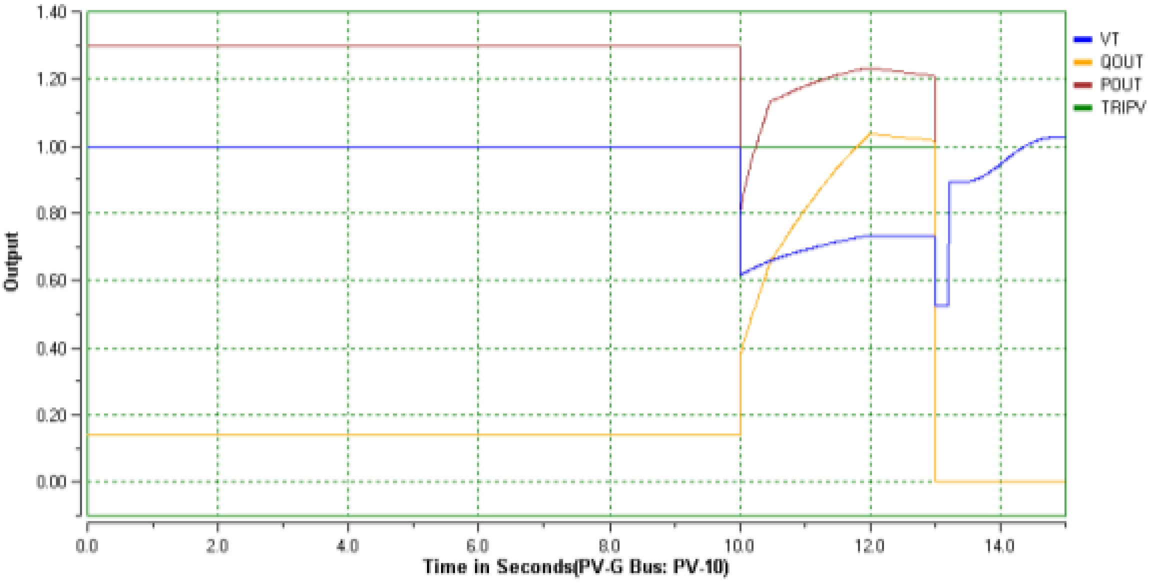

Figure 100 - MW, Mvar, V_T and Trip Signal at PV/Inverter (trip after 3 seconds)

Voltage Regulation:

Demonstration of voltage regulation capability is given in figures 90 and 91. During the under-voltage conditions the inverter supports voltage by injecting additional reactive power. The simulation is similar to one shown in Figures 8.19 and 8.20 but in that case terminal voltage was depressed to zero and no voltage support was possible.

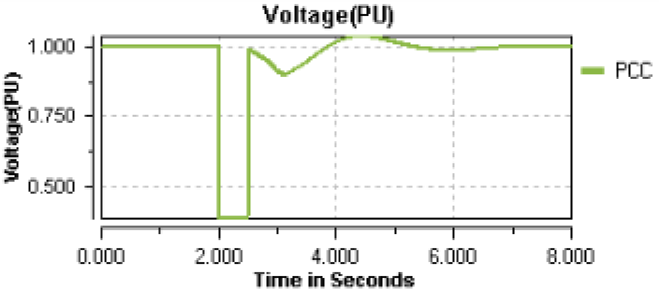

Figure 101 - PCC Voltage

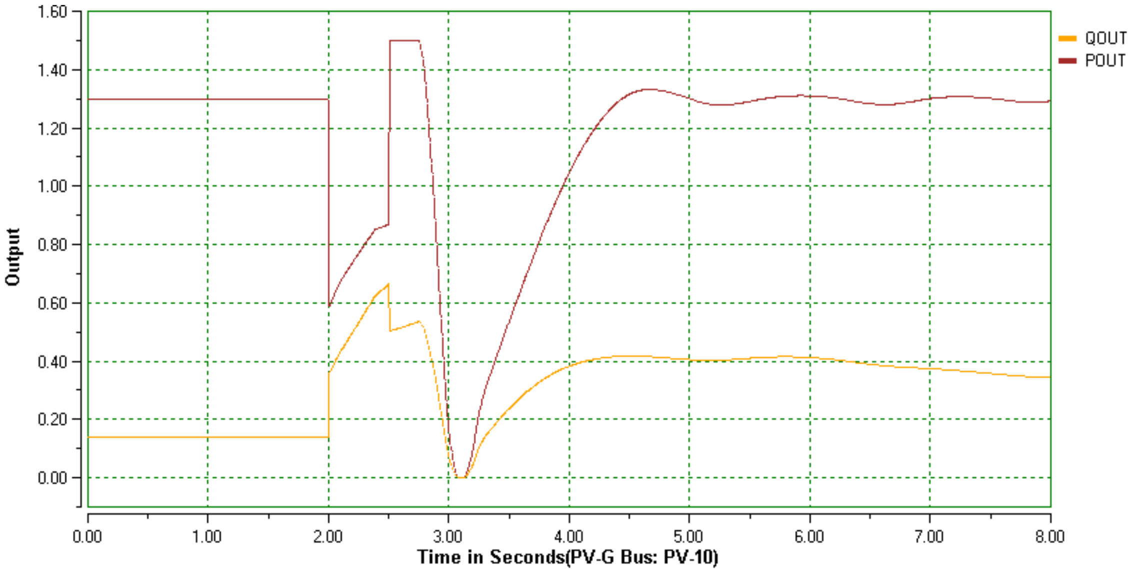

Figure 102 - MW and Mvar outputs of PV/Inverter

6.8.5. Ramping Capabilities

Compliance with the ramping MTR is demonstrated by the following simulations.

Figure 92 shows ramp with the slope of 6 MW/min; ramping command is given at time t=5sec and the ramping level is define as 0.45 MW. The simulation is done on a single PV/Inverter (out of 36 systems). Power at PCC is decreased by 1.05 MW within 10.5 seconds. Sun irradiance is considered constant during this simulation.

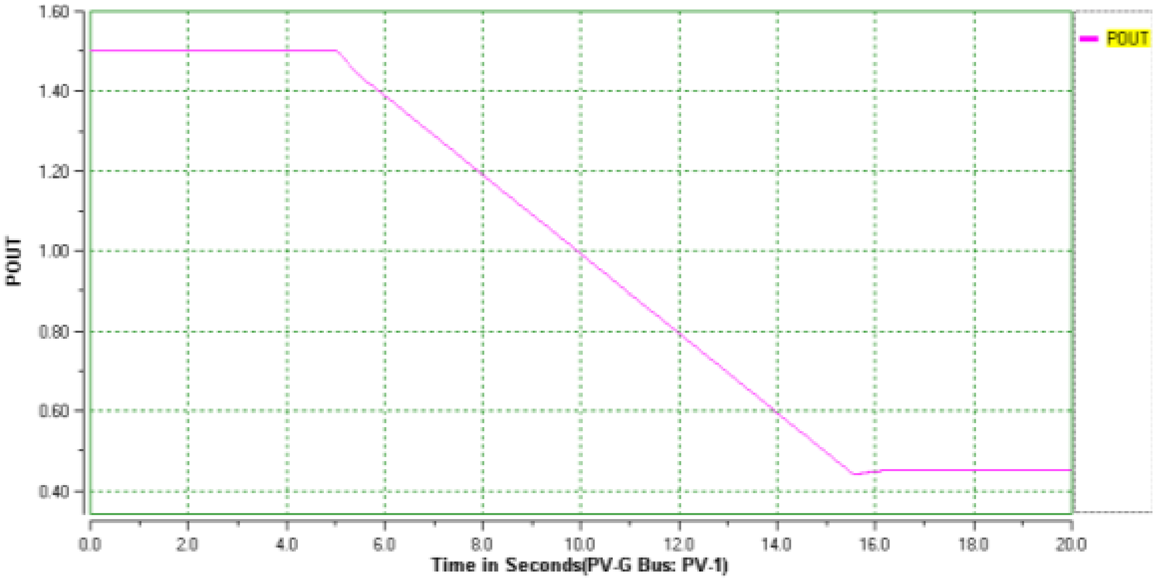

Figure 103 - 6 MW/min ramp

Figure 93 shows the impact of the variable sun irradiance on the system; data for this sun irradiance variation was recorded at UCSD (real weather data). The data includes fast transient from maximum power to 40% of the maximum power within 5 seconds and several subsequent power swings.

Figure 94 shows superposition of the ramping command and irradiance data. It demonstrates that the controller will work as desired. Ramp is applied before the weather event and system reaches requested point (0.75 MW per one PV/Inverter unit for this simulation). Subsequent weather variations will not increase the production as long as the ramping signal is present. Certainly, weather can cause the system to reduce the production if there is not enough sun energy available.

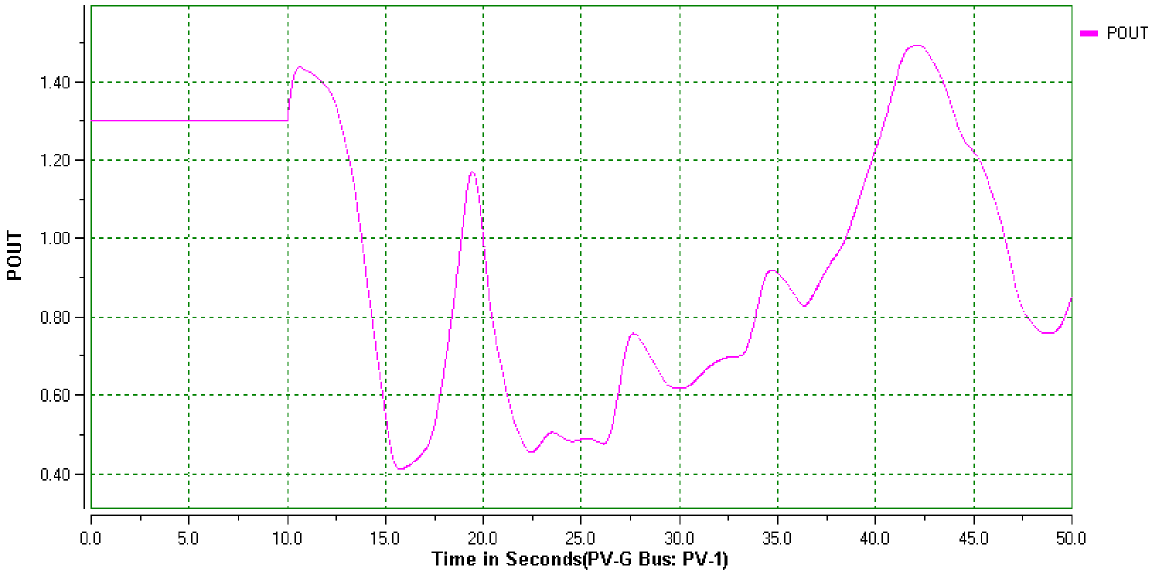

Figure 104 - Impact of Weather Variability on PV Production

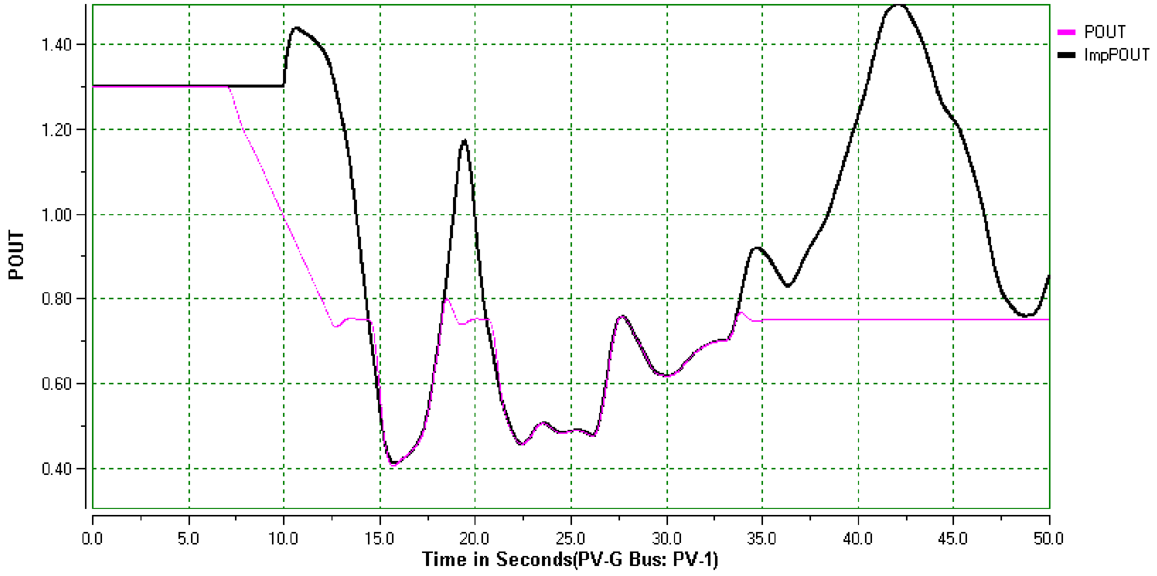

Figure 105 - Superposition of Ramming and Weather Variability

6.8.6. Transient Simulation of Battery/ Converter Model

The battery parameters in Table 14, which are based on various manufacturers' data, are used in this simulation. This data is extracted from the Intensium Max energy storage system for Saft Company. The battery bank consists of 174 series and 20 parallel lithium-ion VL41M cells with the parameters shown presented in Table 15 and Figure 95. These data are utilized to derive the total storage battery parameters for the transient study and the resulting parameters are shown in Figure 88.

Table 19. Energy Storage System Parameters

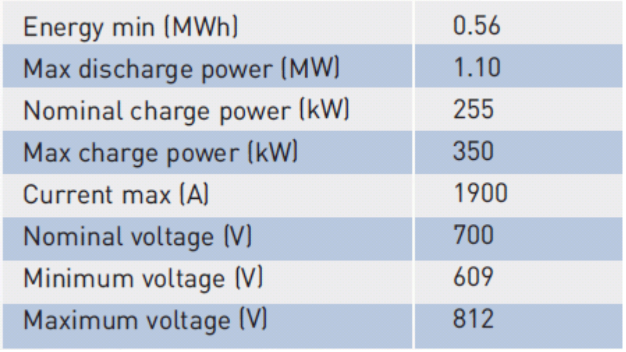

Energy min (MWh)	0.56
Max discharge power (MW)	1.10
Nominal charge power (kW)	255
Max charge power (kW)	350
Current max (A)	1900
Nominal voltage (V)	700
Minimum voltage (V)	609
Maximum voltage (V)	812

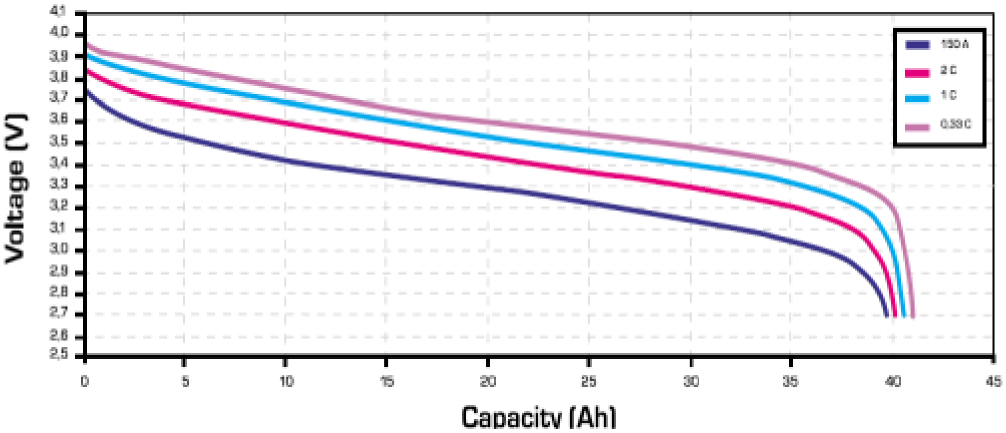

Figure 106 - VL41M Cell capacity and voltage according to current @ 20°C

Table 20. Electrical characteristics of VL41M Battery Cell

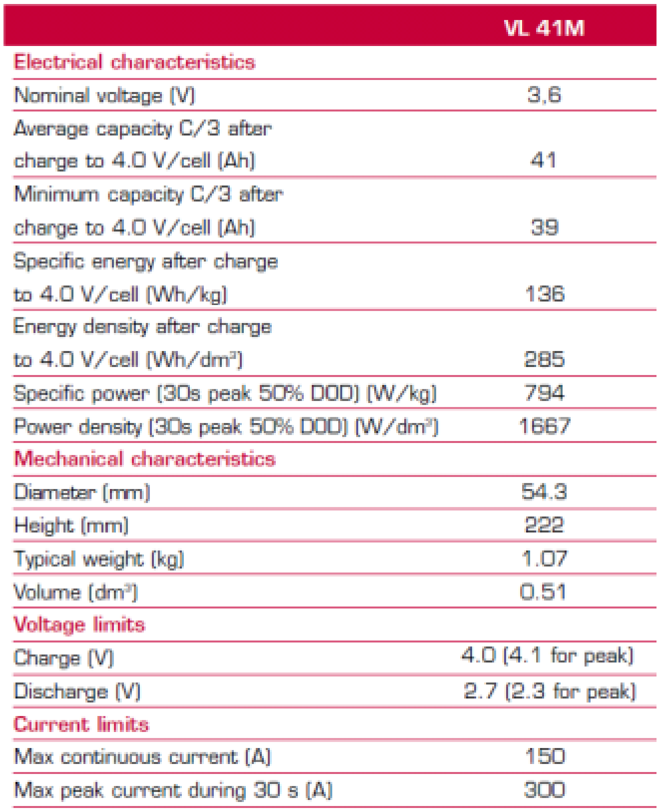

	VL 41M
Electrical characteristics	
Nominal voltage (V)	3,6
Average capacity C/3 after charge to 4.0 V/cell (Ah)	41
Minimum capacity C/3 after charge to 4.0 V/cell (Ah)	39
Specific energy after charge to 4.0 V/cell (Wh/kg)	136
Energy density after charge to 4.0 V/cell (Wh/dm^3)	285
Specific power (30s peak 50% DOD) (W/kg)	794
Power density (30s peak 50% DOD) (W/dm^3)	1667
Mechanical characteristics	
Diameter (mm)	54.3
Height (mm)	222
Typical weight (kg)	1.07
Volume (dm^3)	0.51
Voltage limits	
Charge (V)	4.0 (4.1 for peak)
Discharge (V)	2.7 (2.3 for peak)
Current limits	
Max continuous current (A)	150
Max peak current during 30 s (A)	300

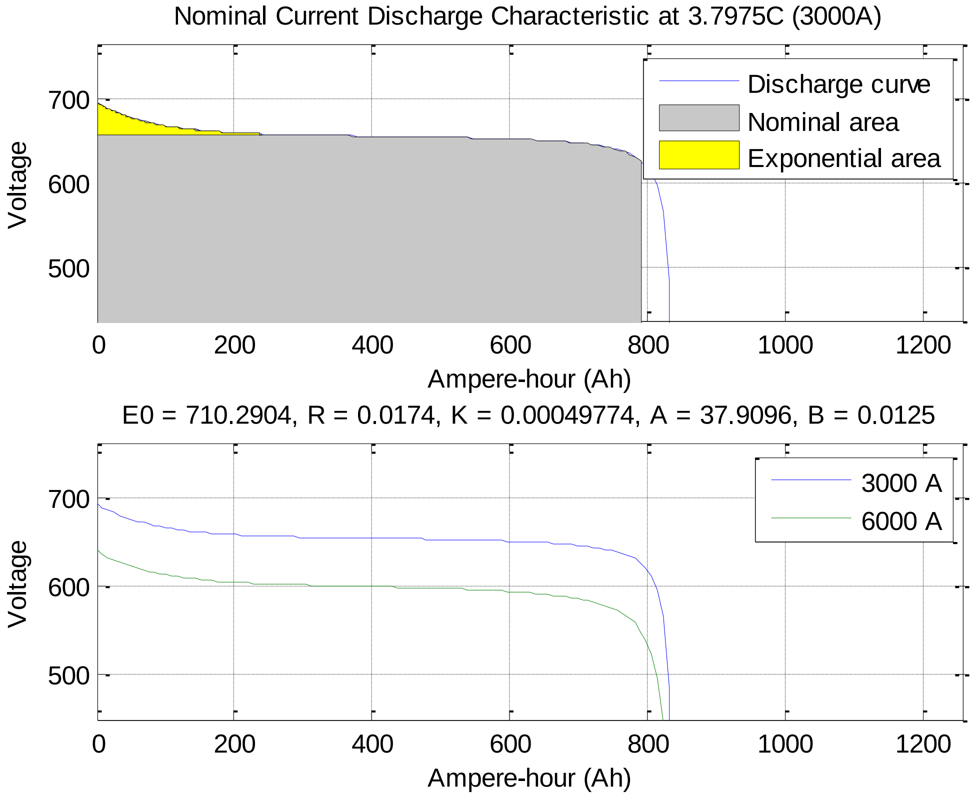

Figure 107 - VL41M Cell capacity and voltage according to current @ 20°C

6.9. Case A: PV Plant without Battery Storage

In the first case, batteries are not considered and there is no control on the PV Plant output power. Figure 97 shows one of the PV's input irradiance signal (pu), active power output (MW), voltage terminal (pu) and frequency (pu).

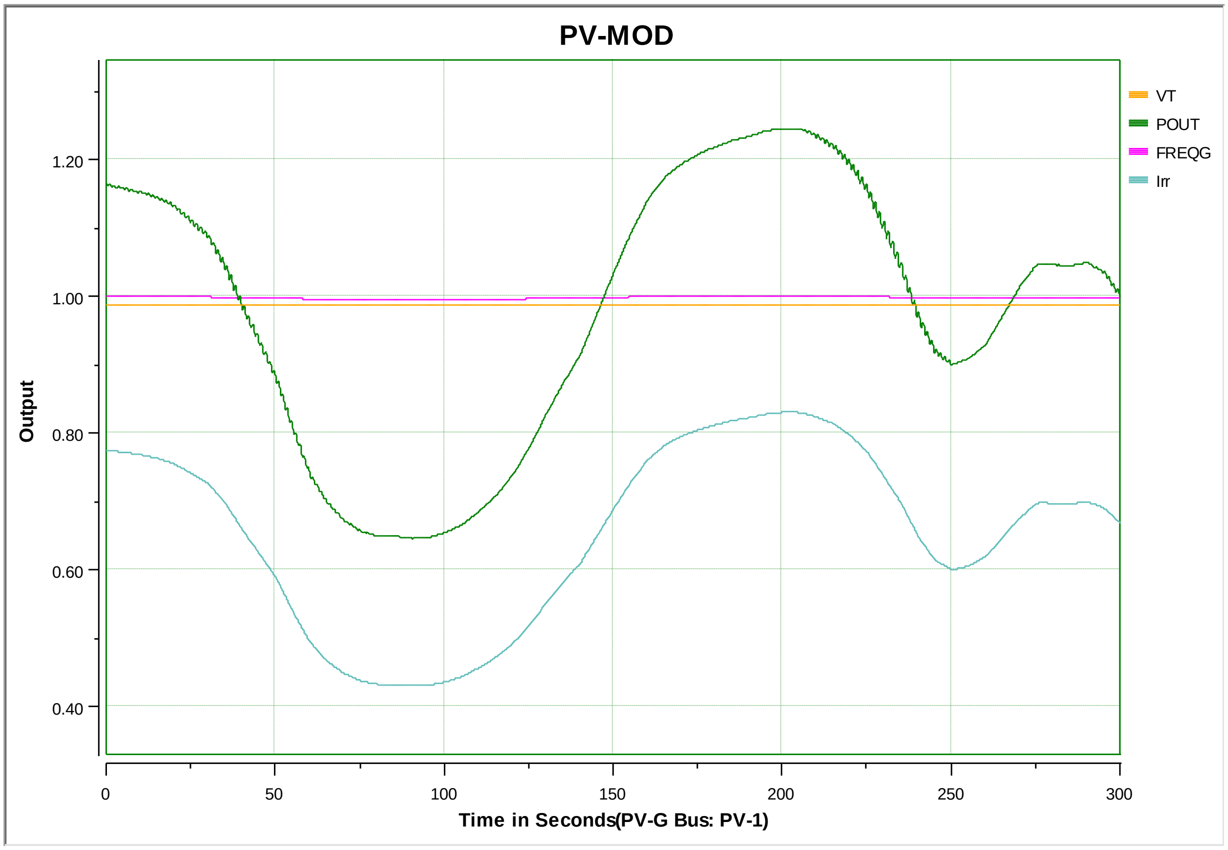

Figure 108 - One of the PV's irradiance (pu), output power (MW), voltage (pu) and frequency (pu)

The PV power plant output active power (MW), voltage (pu) and frequency (Hz) of Point of Common Coupling (PCC) are shown in Figure 98. The frequency of PCC point is almost following the PV generation level.

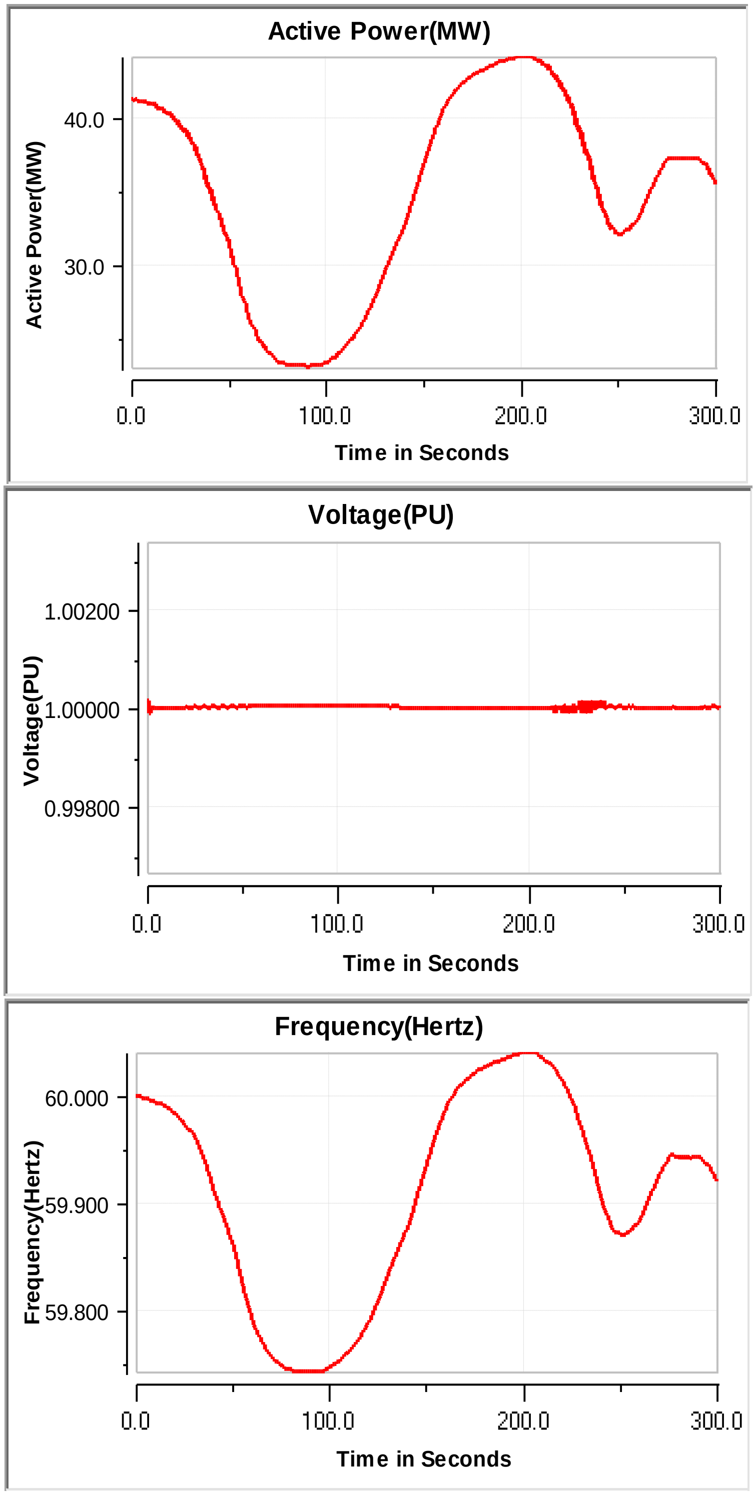

Figure 109 - PV Plant output power (MW), voltage (pu) and frequency (pu)

6.10. Case B: PV Plant with Battery Storage

In the second case, battery storage is considered using the same concept for smoothing the power ramp rates for the total PV generation. To achieve this, the output power control signal is calculated for each battery to decrease the ramping rate of PV generations to 5MW/1min and is shown in Figure 8.7.33. Using this signal will lead to the DC current waveform shown in Figure 8.7.34. The positive current means discharging and the negative current presents the recharging mode. The DC power and current are limited to the battery storage device design specifications which occurs at t=160 seconds in recharging mode. This is already considered in control power signal.

The battery voltage is then calculated using the battery dynamic model which is illustrated in Figure 93. The state of charge of the battery is also presented in Figure 94 and assumed to be 100% in beginning of the simulation. During the discharge SOC drops to 96.6%. Finally, battery output power is shown in Figure 95 which is totally following the power control signal and injects this amount of power to the AC side. The small difference is related to the converter efficiency which is set to 97%.

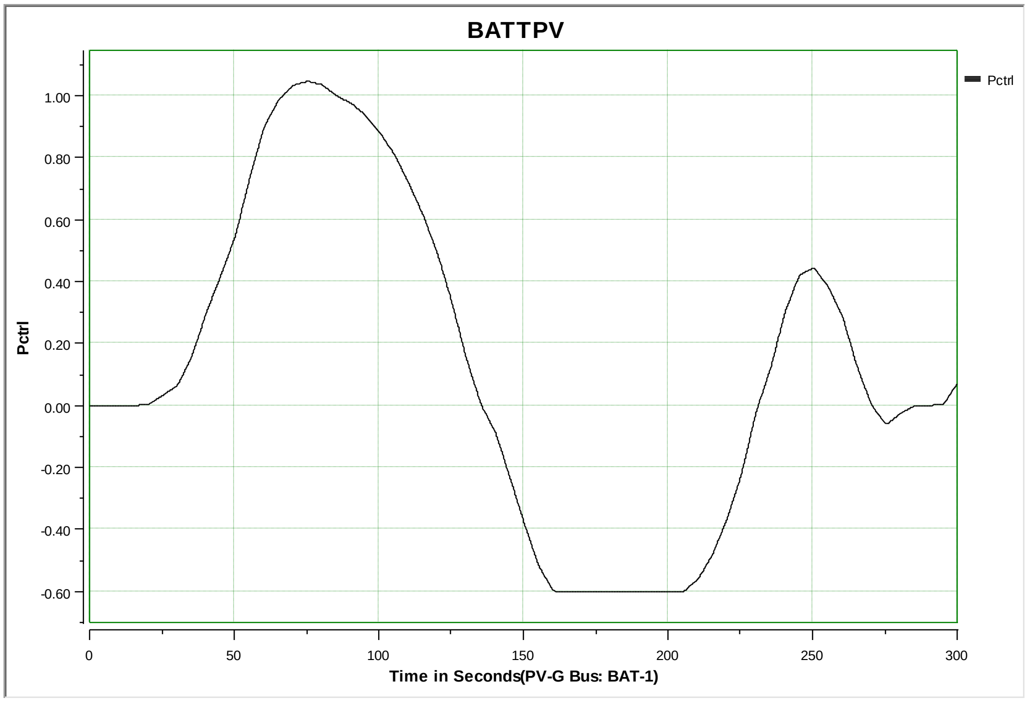

Figure 110 - Battery Power Control Signal [MWatt]

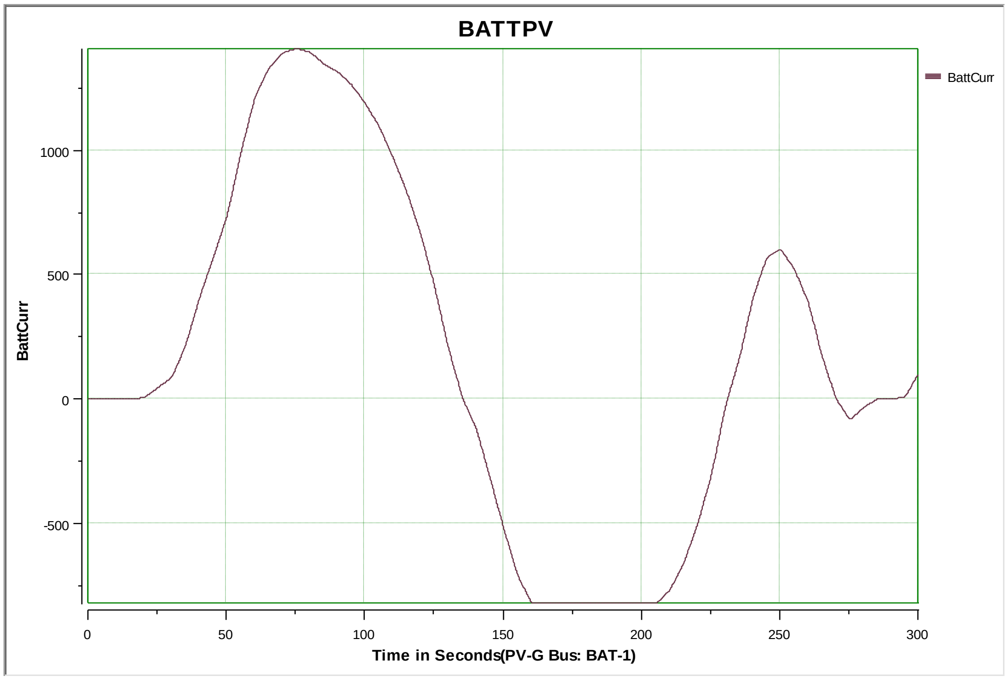

Figure 111 - Battery DC Current [Amp]

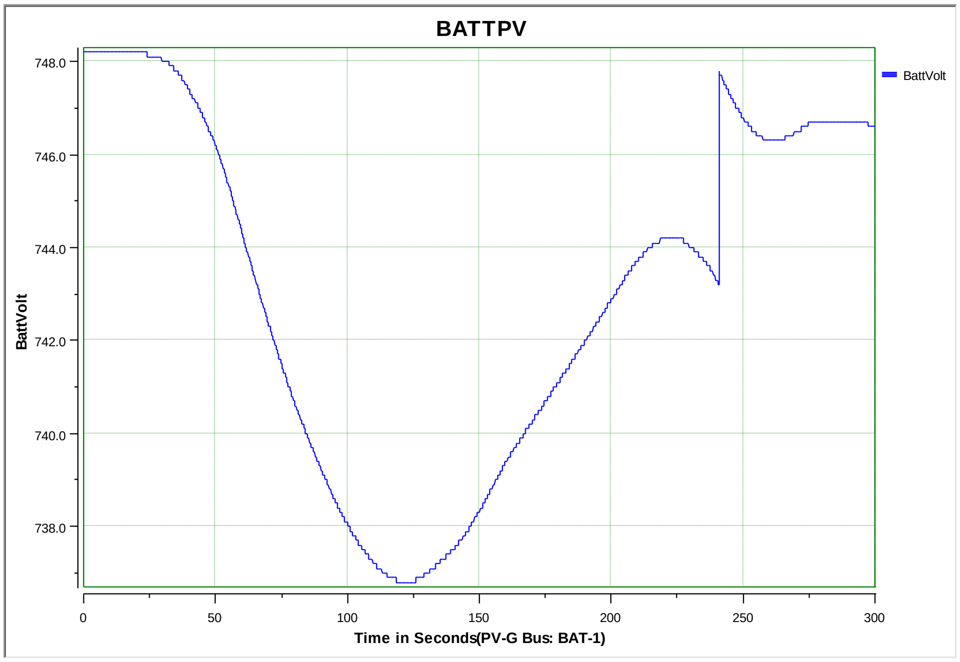

Figure 112 - Battery DC Voltage [Volt]

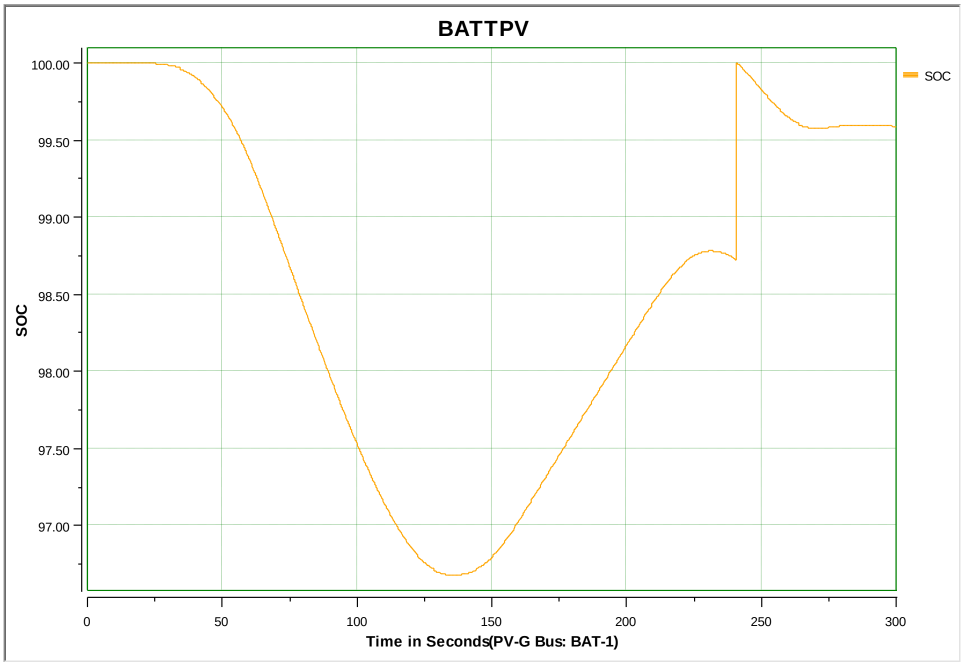

Figure 113 - Battery State of the Charge [%]

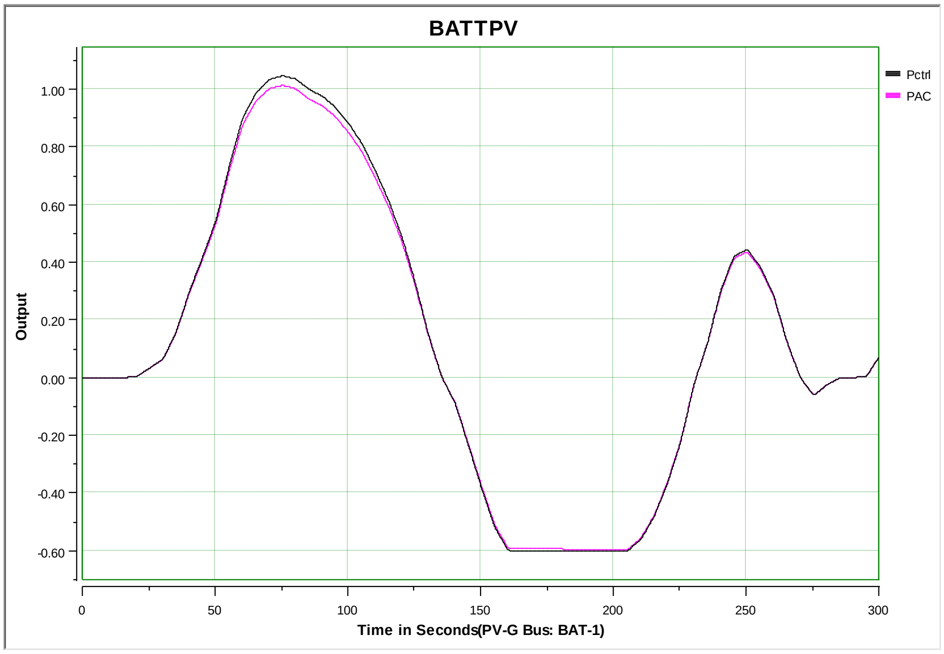

Figure 114 - Battery Storage Active AC power output versus the control signal [MW]

Similar to the previous case, the PV power plant output active power (MW), voltage (pu) and frequency (Hz) of Point of Common Coupling are shown in Figure 104.
The PV Plant output power [MW] with (Red line) and without (Black line) Battery Storage System is shown in Figure 105 for better comparison between deploying storage systems for limiting plant output power ramp ratings. As clearly shown this control methodology will enhance the PV system operation integrated with a power system by considering all power quality constrains.

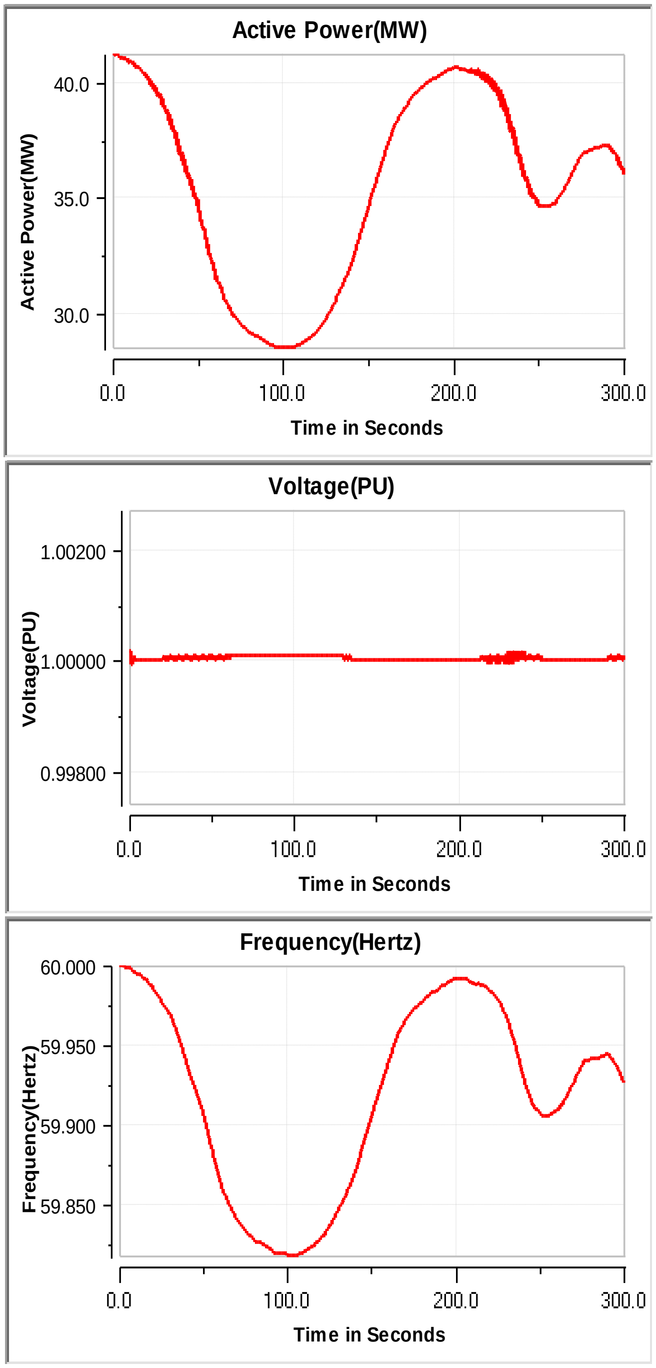

Figure 115 - PV Plant output power (MW), voltage (pu) and frequency (pu) with Battery Usage

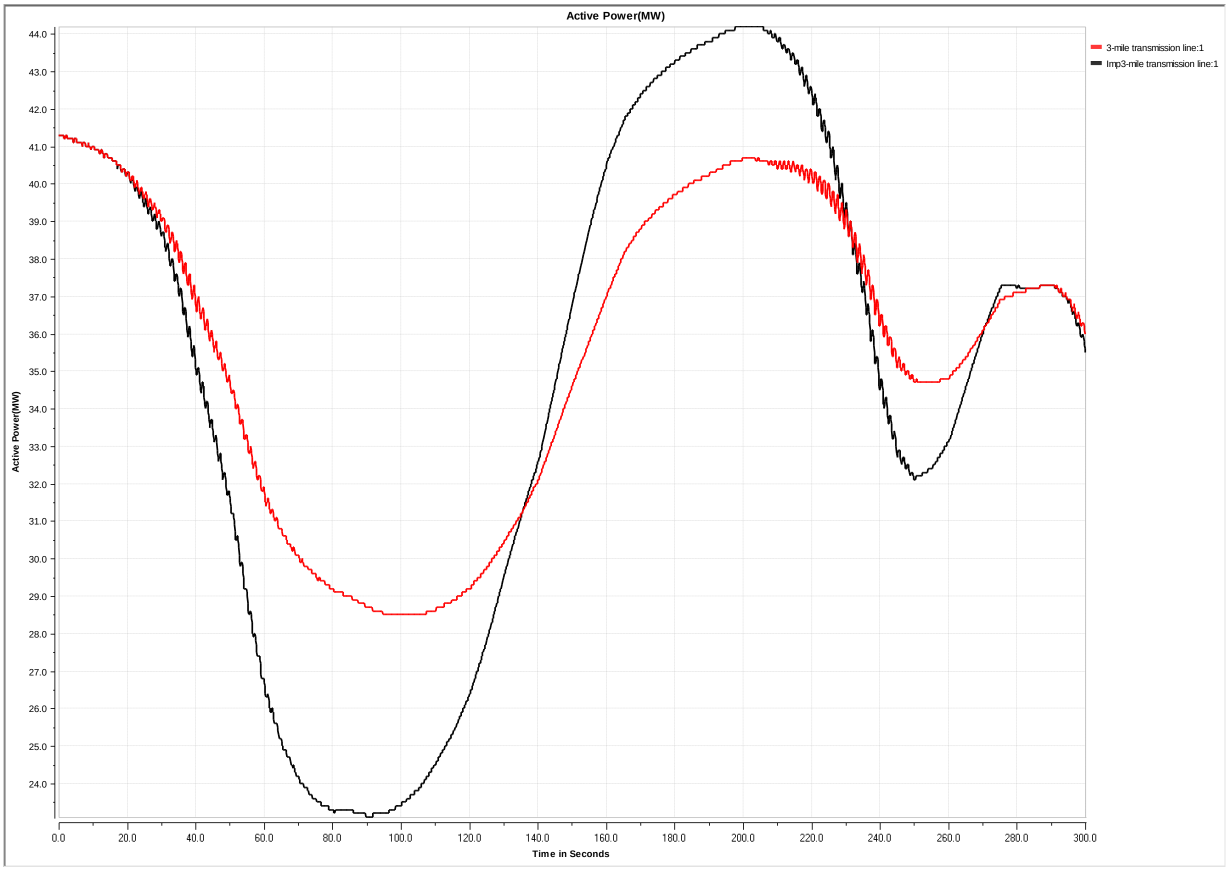

Figure 116 - PV Plant output power [MW] with (Red line) and without (Black line) Battery Storage System

Consequently, the developed battery dynamic model can be utilized for:

- Sizing the battery according the PV plant size, statics of annual irradiance and its application for power regulating and smoothing
- Modeling the dynamic behavior of the Battery Charge/Discharge Curve for transient studies under different events and scenarios by tracking its voltage and state of charge
- Considering Energy storage device limitations in charge/discharge power, depth of discharge and maximum stored power
- Developing real-time control methodology for mitigating worse power ramp rates in PCC point using storage devices with/without forecasted data
- Optimizing control parameters for the objective application usage of storage devices and performance evaluation for several sun irradiance profiles

6.11. Summary

Power Analytics has been involved and engaged with advancing the integration of photovoltaic power systems with particular focus on interconnect simulations, integration of control and integration of irradiance forecasts. This combined approach is central to the Power Analytics ability to bring these simulations into a real-time operating strategy so essential to moving past simulation and focusing on deployment of photovoltaic farms. In addition to the simulations made possible as a result of this work (including dynamic simulations), the combined approach of modeling, forecasting, control and operation including charging/discharging of energy storage promises to provide the most exciting advances in High Penetration PV.

7. Publications under this Award and References

[1.] Chow CW, Urquhart B, **Kleissl J**, Lave M, Dominguez A, Shields J, Washom B, Intra-hour forecasting with a total Sky Imager at the UCSD solar energy testbed, *Solar Energy*, doi:10.1016/j.solener.2011.08.025, September 2011

[2.] Nottrott, A, **Kleissl J**, Washom B, Financial Benefits of Energy Storage Dispatch Schedule Optimization, Electrical Energy Storage Applications & Technology Conference, San Diego, 2011

[3.] Lave M, **J Kleissl**, J Stein, A Wavelet-based Variability Model (WVM) for Solar PV Powerplants, IEEE Transactions on Sustainable Energy, 99, 2012, 10.1109/TSTE.2012.2205716

[4.] Nottrott, A, **J Kleissl**, Energy dispatch schedule optimization and cost benefit analysis for grid-connected, photovoltaic-battery storage systems, Renewable Energy, 55:230-240, 2013.

[5.] Lave, M, **J Kleissl**, Cloud Speed Impact on Solar Variability Scaling - Application to the Wavelet Variability Model, Solar Energy, 91:11-21, 10.1016/j.solener.2013.01.023., 2013.

[6.] Ery Arias Castro, **J Kleissl**, M Lave, Jason Schweinsberg, Ruth Williams, A Poisson model for anisotropic solar ramp rate correlations, Solar Energy, 2014, in press.

[7.] Yang, H, B Kurtz, A Nguyen, B Urquhart, CW Chow, M Ghonima, **J Kleissl**, Solar irradiance forecasting using a ground-based Sky Imager developed at UCSD, Solar Energy, in press, 2014

[8.] Daria S, Meagher K, Guidelines for large photovoltaic system integration,Transmission and Distribution Conference, IEEE PES, Orlando 2012

[9.] Meagher, K, Solar Data and the Cloud, Utility And Grid Analytics Symposium, Washington DC, June, 2013

[10.] Meagher, K, Modeling of Photo Voltaic Power Plants, IEEE PES Conference, Austin, July, 2012

[11.] Meagher, K, Koopman, R, Microgrid challenges and opportunities with connectivity, standards and the future, UCAIug, Austin, November, 2012

[12.] Meagher, K, Practical lessons of a Microgrid, Microgrid World Forum, Irvine, March 2013

[13.] Meagher, K, Big Data & Analytics for the Future of the Smart Grid, Softgrid, San Francisco, August, 2012

[14.] Meagher, K, Washom, B, Seifert, G, Manz, L, UCSD Case Study, Microgrid Virtual Summit, March, 2012

[15.] Meagher, K, Enhancing Distribution – Increasing Reliability, Smart Grid Distribution Automation, Raleigh, November, 2013

[16.] Meagher, K, Solar PV Integration at the Distribution Level, EUCI, Golden, November 2012

[17.] Salehi, V, Ramp Rate Control of Photovoltaic Power Plant Output Using Energy Storage Devices, IEEE PES, Washington DC, July, 2014

References

Allmen, M. & Kegelmeyer, W., 1996. The computation of cloud-base height from paired whole-sky imaging cameras. *Journal of Atmospheric and Oceanic Technology,* Volume 13, pp. 97 - 113.

Amsbary, S. & Slack, P., 2011. *Grid-Interop Foundational Session: Smart Grid Interoperability Maturity [PPT Presentation],* Phoenix, AZ: s.n.

Anon., 2011. *IEEE Guide for Smart Grid Interoperability of Energy Technology and Information Technology Operation with the Electric Power System (EPS), End-Use Applications, and Loads.* s.l.:IEEE Standard 2030™.

Arias-Castro, E., Kleissl, J. & Lave, M., 2014. A Poisson model for anisotropic solar ramp rate correlations. *Solar Energy,* Volume 101, pp. 192 - 202.

Beaubien, M. & Freedman, J., 2001. *Comparison of Two Imager-based Methods for Determination of Winds Aloft..* s.l., s.n.

Benjamin, S. et al., 2010. *Improvements in NOAA modeling and data assimilation to improve guidance for the renewable energy industry..* s.l., s.n.

Cano, D. et al., 1986. A method for the determination of global solar radiation from meteorological satellite data. *Solar Energy,* Issue 37, pp. 31 - 39.

Ceglia, M. et al., n.d. *New Technology Development Committee, Smart Grid, NTDC Smart Grid Meeting Summary [PPT Presentation],* s.l.: s.n.

Chen, C., Duan, S., Cai, T. & Liu, B., 2011. Online 24-h solar power forecasting based on weather type classification using artificial neural network. *Solar Energy,* 85(11), pp. 2856 - 2870.

Chow, C. W. et al., 2011. Intra-hour forecasting with a total Sky Imager at the UCSD solar energy testbed. *Solar E nergy,* Volume 85, pp. 2881 - 2893.

Cleveland, F. et al., 2008. *Smart Grid: Interoperability and Standards, An Introductory Review,* s.l.: Utility Standards Board.

Curwin, T., 2012. *Virtual Power Plants Are for Real.* [Online]
Available at: http://www.cnbc.com/id/46892511/Virtual_Power_Plants_Are_for_Real

Farr, T. G. et al., 2007. The shuttle radar topography mission. *Reviews of Geophysics,* 45(2).

Ghonima, M. et al., 2012. A method for cloud detection and opacity classification based on ground based Sky Imagery. *Atmospheric Measurement Techniques,* Volume 5, pp. 2881 - 2892.

GridWise Architecture Council, 2009. *Environmental Benefits of Interoperability: The Road to Maximizing Smart Grid's Environmental Benefit.* [Online]
Available at: http://www.gridwiseac.org/pdfs/environmentalffiinteroperability.pdf

GridWise Architecture Council, 2009. *Financial Benefits of Interoperability: How Interoperability in the Electric Power Industry Will Benefit Stakeholders Financially,* s.l.: s.n.

GridWise Architecture Council, 2010. *Introduction to Interoperability and Decision-Maker's Interoperability Checklist Version 1.5,* s.l.: s.n.

GridWise Architecture Council, 2011. *The Smart Grid Interoperability Maturity Model,* s.l.: U.S. Government.

GridWise Architecure Council, 2009. *Reliability Benefits of Interoperability,* s.l.: s.n.

Gunther, E., 2008. *Smart Grid Development, Interoperability and Coordination,* s.l.: IEEE 2008 T&D Show, Smart Grid Super Session - SS02, [PPT Presentation].

Hamill, T. & Nehrkorn, T., 1993. A short-term cloud forecast scheme using cross correlation.. *Wea. Forecasting,* Issue 8, pp. 401 - 411.

Heinle, A., Macke, A. & Srivastav, A., 2010. Automatic cloud classification of whole sky images. *Atmos. Meas. Tech.*, Issue 3, pp. 557 - 567.

Huang, H. et al., 2012. *Correlation and local feature base cloud motion estimation.* s.l., ACM, pp. 1 - 9.

Huang, J., Korolkiewicz, M., Agrawal, M. & Boland, J., 2013. Forecasting solar radiation on an hourly time scale using a coupled autoregressive and dynamical system (CARDS) model. *Solar Energy*, Volume 87, pp. 136 - 149.

Huo, J. & Lu, D., 2009. Cloud determination of all-sky images under low visibility conditions. *J. Atmosph. Oceanic Technology*, 26(10), pp. 2172 - 2180.

Huo, J. & Lu, D., 2010. Preliminary retrieval of aerosol optical depth from allsky images. *Adv. Atmos. Sci.*, 27(2), pp. 421 - 426.

Ineichen, P. & Perez, R., 2002. A new airmass independent formulation for the Linke turbidity coefficient. *Solar Energy*, Volume 73, pp. 151 - 157.

ISO New England Inc., 2009. *Overview of the Smart Grid -- Policies, Initiatives, and Needs,* s.l.: s.n.

Johnson, R., Shields, J. & Koehler, T., 1991. *Analysis and Interpretation of Simultaneous Multi-Station Whole Sky Imagery,* San Diego, CA: SIO Ref. 91-3, PL-TR-91-2214.

Johnson, R., W., H. & Shields, J., 1989. *Automated visibility and cloud cover measurements with a solid-state imaging system,* San Diego, CA: SIO Ref. 89-7, GL-TR-89-0061.

Kalisch, J. & Macke, A., 2008. Estimation of the total cloud cover with high temporal resolution and parameterization of short-term fluctuations of sea surface insolation. *Meteorol. Z.*, Issue 17, pp. 603 - 611.

Kassianov, E., Long, C. & Christy, J., 2005. Cloud-base-height estimation from paired ground-based hemispherical observations. *J. Appl. Meteor.*, Issue 44, pp. 1221 - 1233.

Katzenbeisser, S. et al., 2011. *Privacy and Security in Smart Energy Grids.* Germany, s.n., pp. 62 - 68.

KEMA, Inc., 2010. *Innovation Day White Paper: The Virtual Power Plant,* Oakland, CA: s.n.

Koch, E. & Piette, M. A., 2007. *Architecture Concepts and Technical Issues for an Open, Interoperable Automated Demand Response Infrastructure.* Albuquerque, NM, s.n.

Koch, E. & Piette, M. A., 2008. *Scenarios for Consuming Standardized Automated Demand Response Signals.* Atlanta, GA, s.n.

Lara-Fanego, V. et al., 2011. Evaluation of the WRF model solar irradiance forecasts in Andalusia (southern Spain). *Solar Energy.*

Lave, M. & Kleissl, J., 2013. Cloud speed impact on solar variability scaling -- application to the wavelet variability model. *Solar Energy*, Volume 91, pp. 11 - 21.

Lave, M., Kleissl, J. & Arias-Castro, E., 2012. High-frequency irradiance fluctuations and geographic smoothing. *Solar Eenrgy*, 86(8), pp. 2190 - 2199.

Lave, M., Kleissl, J. & Stein, J. S., 2012. A wavelet-based variability model (WVM) for solar PV power plants. *IEEE Transactions on Sustainable Energy*, Volume 99, pp. 501 - 509.

Li, D. & et al., 2012. *Efficient Authentication Scheme for Data Aggregation in Smart Grid with Fault Tolerance and Fault Diagnosis.* Washington, DC, s.n., pp. 1 - 8.

Long, C. J., Sabburg, J., Calbó, J. & Pagès, D., 2006. Retrieving cloud characteristics from ground-based daytime color all-sky images. *J. Atmos. Ocean. Technol.*, Volume 23, pp. 633 - 652.

Lorenz, E. et al., 2007. *Forecast of ensemble power production by grid-connected PV systems.* 3 - 9, s.n.

Lorenz, E. et al., 2009. *Benchmarking of different approaches to forecast solar irradiance.* Hamburg, Germany, s.n., pp. 21 - 25.

Marquez, R. & Coimbra, C. F. M., 2013. Intra-hour DNI forecasting based on cloud tracking image analysis. *Solar Energy,* Volume 91, pp. 327 - 336.

Marquez, R. & Coimbra, C. F. M., 2013. Proposed metric for evaluation of solar forecasting models. *Journal of Solar Energy Engineering,* Volume 135, pp. 011016-(1-9).

Marquez, R., Pedro, H. T. C. & Coimbra, C. F. M., 2013. Hybrid solar forecasting method uses satellite imaging and groudn telemetry as inputs to ANNs. *Solar E nergy,* Volume 92, pp. 176 - 188.

Mathiesen, P. & Kleissl, J., 2011. Evaluation of numerical weather prediction for intra-day solar forecasting in the continental United States. *Solar Energy,* 85(5), pp. 967 - 977.

McCartney, E., 1976. *Optics of the Atmosphere: Scattering by Molecules and Particles.* s.l.:John Wiley & Sons.

Musser, D., 2012. *Demand Responsible. [Blog, "On a Tangent"]*. [Online]
Available at: http://www.tangentenergy.com/2012/04/demand-responsibly/

National Energy Technology Laboratory for the U.S. Department of Energy, Office of Electricity Delivery and Energy Reliability, 2007. *Appendix B1: A Systems View of the Modern Grid, Version 2.0 Integrated Communications,* s.l.: s.n.

National Institute of Standards and Technology (NIST), 2010. *NIST Framework and Roadmap for Smart Grid Interoperability Standards, Release 1.0,* s.l.: U.S. Department of Commerce.

Paoli, C., Voyant, C., Muselli, M. & Nivet, M.-L., 2010. Forecasting of preprocessed daily solar radiation time series using neural networks. *Solar Energy,* 84(12), pp. 2146 - 2160.

Pereira, E. et al., 2000. Effects of burning of biomass on satellite estimations of solar irradiation in Brazil. *Solar Energy,* Volume 68, pp. 91 - 107.

Perez, R. et al., 2002. A new operational model for satellite-derived irradiances: description and validation. *Solar Energy,* Volume 73, pp. 307 - 317.

Perez, R. et al., 2010. Validation of short and medium term operational solar radiation forecasts in the US. *Solar Energy,* Volume 84, pp. 2161-2172.

Pfister, G. et al., 2003. Cloud coverage based on all-sky imaging and its impact on surface solar irradiance. *Journal of Applied Meteorology and Climatology,* 42(10), pp. 1421 - 1434.

Piette, M. A. et al., 2007. *Design and Implementation of an Open, Interoperable Automated Demand Response Infrastructure.* Albuquerque, NM, s.n.

Piette, M. A. et al., 2008. *Linking Continuous Energy Management and Open Automated Demand Response.* Atlanta, GA, s.n.

PREPA, 2012. *Puerto Rico electric power authority minimum technical requirements for photovoltaic generation (PV) projects.* s.l.:s.n.

Remund, J., Perez, R. & Lorenz, E., 2008. *Comparison of Solar Radiation Forecasts for the USA.* Valencia, Spain, s.n., pp. 1.9 - 4.9.

Rigollier, C., Lefèvre, M. & Wald, L., 2004. The method Heliosat-2 for deriving shortwave solar radiation from satellite images. *Solar Energy,* Volume 77, pp. 159-169.

Schmetz, J., 1989. Towards a surface radiation climatology: retrieval of downward irradiances from satellites. *Atmos. Res.,* Volume 23, pp. 287 - 321.

Schroedter-Homscheidt, M. et al., 2009. *Nowcasting and forecasting of solar irradiance for energy electricity generation.* s.l., s.n.

Schulz, C. et al., n.d. *Virtual Power Plants with Combined Heat and Power Micro-units*, Germany: Technical University Braunschweig, Institute of High-Voltage and Electric Power Systems.

Seiz, G. et al., 2007. Cloud mapping with ground-based photogrammetrics cameras. *International Journal of Remote Sensing*, 28(9), pp. 2001 - 2032.

Shields, J., Johnson, R., Karr, M. & Wertz, J., 1998. *Automated Day/Night Whole Sky Imagers for Field Assessment of Cloud Cover Distributions and Radiance Distributions.* s.l., s.n., pp. 165 - 170.

Shields, J. et al., 2007. *Continuing Support of Cloud Free Line of Sight Determination including Whole Sky Imaging of Clouds,* San Diego, CA: Final Report for ONR Contract N00014-01-D-0043 DO #13.

Shields, J. et al., 2009. *Research toward Multi-Site Characterization of Sky Obscuration by Clouds,* San Diego, CA: Final Report for Grant N00244-07-1-009.

United States of America Federal Energy Regulatory Commission, 2011. *Standards for Business Practice and Communication Protocols for Public Utilities,* Washington, DC: Submittal of Smart Grid Related Standards.

Urquhart, B. et al., 2012. *Towards intra-hour solar f orecasting using two Sky Imagers at a large solar power plant.* Denver, CO, USA, s.n.

Urquhart, B. et al., 2013. Sky imaging systems for short-term solar forecasting. In: *Solar Energy Forecasting and Resource Assessment.* s.l.:Academic Press.

Von Dollen, D., 2009. *Report to NIST on the Smart Grid Interoperability Standards Roadmap--Post Comment Period Version,* s.l.: Electric Power Research Institute (EPRI).

Whitacker, C. et al., 2008. *Renewable Systems Interconnection Study: Distributed Photovoltaic Systems Design and Technology Requirements,* Albuquerque, NM and Livermore, CA: Sandia National Laboratories.

Zelenka, A., Perez, R., Seals, R. & Renné, D., 1999. Effective accuracy of satellite-derived irradiance. *Theor. Appl. Climatol.,* Volume 62, pp. 199 - 207.

Acknowledgments and Disclaimer

This material is based upon work supported by the Department of Energy under Award Number EE-0004680.